The Dissertation Committee for Penghao Xiao
certifies that this is the approved version of the following dissertation:

Exploring energy landscapes of solid-state materials: from individual atoms to collective motions.

Committee:

Graeme A. Henkelman, Supervisor

Keith J. Stevenson

Peter J. Rossky

David A. Vanden Bout

Gyeong S. Hwang

Exploring energy landscapes of solid-state materials: from individual atoms to collective motions.

by

Penghao Xiao, B.S.

DISSERTATION

Presented to the Faculty of the Graduate School of

The University of Texas at Austin

in Partial Fulfillment

of the Requirements

for the Degree of

DOCTOR OF PHILOSOPHY

THE UNIVERSITY OF TEXAS AT AUSTIN

May 2014

Dedicated to my family.

Acknowledgments

First of all, I would like to thank my advisor, Graeme Henkelman, for his great guidance in my graduate study. His inspiring discussions and sincere encouragements made the research processes enjoyable. I will continue to benefit from his way of thinking, as well as his communication and management skills in my career development. Also I want to thank my parents for their continuous support for my pursuit of science. Special thanks to my wife, Libin Zhang, who has been exploring the true meaning of life with me. My first paper was coauthored with Daniel Sheppard on developing the generalized solid-state NEB (G-SSNEB) method and it was pleasant to work with him. Kyu-Sung Park and Anthony Dylla introduced to me several experimental projects on batteries for theoretical explanations. Qiang Zhu, Jinguang Cheng and Jianshi Zhou provided phase transition examples where the G-SSNEB method applies. Finally, I want to thank Liang Zhang, Samuel Chill, Rye Terrell, Shannon Stauffer and Juliana Duncan for many helpful and delightful discussions.

Exploring energy landscapes of solid-state materials: from individual atoms to collective motions.

Publication No. _____

Penghao Xiao, Ph.D.
The University of Texas at Austin, 2014

Supervisor: Graeme A. Henkelman

Chemical reactions can be understood as transitions from basin to basin on a high dimensional potential energy landscape. Varying temperature only changes the average kinetic energy of the system. While applying voltages or external pressures directly tilts the landscape and drives the reactions in desired directions. In solids at relatively low temperature, where the entropy term is approximately invariant, the reaction spontaneity is determined by the energy difference between the reactant and product basins and the reaction rate can be calculated from the barriers in between. To achieve sufficient accuracy to explain experimental observations we are interested in, density functional theory (DFT) is usually employed to calculate energies. There are two types of reactions I have studied: the first type of reaction only involves a few number of individual atoms, corresponding to traveling in a small volume in the high dimensional configuration space; the other type involves a large amount of atoms moving in a concerted pattern, and the distance traveled in

the configuration space is significantly longer. The scopes of these two in the energy landscapes are in different scales and thus proper metrics for distance measurements are required.

In the first case, I have mainly studied Li/Na behaviors in the cathode materials of secondary batteries. Here resolving the energy landscape step by step with detailed information is possible and useful. By analyzing the energy landscapes with DFT plus the Hubbard U correction, I have explained several phenomena related to the degradation of lithium-rich layered oxides, rate performance of surface modified $LiFePO_4$, and capacity of vanadium-based fluorophosphates. Predictions on both thermodynamic and kinetic properties of materials are also made based on the calculation results and some are confirmed by experiments.

In the second case, my focus is on solid-solid phase transitions. With a tremendous long reaction pathway, examining every possible atomic step is too expensive. By adopting periodic boundary conditions, a small supercell can represent the main feature of the energy landscape in a coarse grained way, where the connection between phases is easier to explore. After the big picture of a phase transition mechanism learned from this simplified model, details along the reaction pathway, like new phase nucleation and growth, could be resolved by using a larger supercell. In the above treatment, two types of variables, the cell vectors and atomic positions, span a generalized configuration space. Special consideration is required to balance these two to keep consistency under different supercells and avoid biases. A solid-state NEB

(SSNEB) and a solid-state dimer (SSD) method are then developed to locate saddle points in the generalized configuration space. With the methodology well justified, we are able to efficiently find possible nucleation mechanisms, for examples the CdSe rock salt to wurtzite and Mo A15 to BCC phase transitions. SSNEB is also applied in studying phases transitions under pressures, including the graphite to diamond, and $CaIrO_3$ perovskite to post-perovskite transitions. Combined with the adaptive kinetic Monte Carlo (AKMC) algorithm, SSD shows the ability to find new polymorphs of CdSe and the connecting barriers between them.

Table of Contents

Acknowledgments **v**

Abstract **vi**

List of Figures **xiii**

List of Tables **xv**

Chapter 1. Introduction **1**

1.1 Lithium/sodium ion batteries 2

1.1.1 Calculations of oxygen stability in lithium rich layered cathodes 4

1.1.2 Enhanced Rate performance by Anion Surface Modification of $LiFePO_4$ 5

1.1.3 Theoretical Study of Vanadium-Based Fluorophosphates Cathodes for Rechargeable Batteries 6

1.2 Solid-solid phase transitions 7

1.2.1 A Generalized Solid-state Nudged Elastic Band Method 8

1.2.2 From Graphite to Diamond: Reaction Pathways of the Phase Transition 9

1.2.3 Mechanism of the $CaIrO_3$ Post-Perovskite Phase Transition Under Pressure 10

1.2.4 Solid-State Dimer Method for Calculating Solid-Solid Phase Transitions 10

Chapter 2. Calculations of oxygen stability in lithium rich layered cathodes **12**

2.1 Abstract 12

2.2 Introduction 12

2.3 Computational Method 14

2.4 Results 15

2.5 Conclusion 21
2.6 Acknowledgements 23

Chapter 3. Enhanced Rate Performance by Anion Surface Modification of $LiFePO_4$ 24
3.1 Abstract 24
3.2 Introduction 25
3.3 Computational Method 27
3.4 Results 27
3.4.1 Explanation of the Rate Increase 28
3.4.2 Prediction of the Voltage Dependence 30
3.4.3 Experimental Confirmation 31
3.4.4 Understanding Li binding at the Surface 32
3.5 Conclusion 37
3.6 Acknowledgments 38

Chapter 4. Theoretical Study of Vanadium-Based Fluorophosphates Cathodes for Rechargeable Batteries 39
4.1 Abstract 39
4.2 Introduction 40
4.3 Computational Method 41
4.4 Results 42
4.5 Conclusion 53
4.6 Acknowledgments 53

Chapter 5. A Generalized Solid-state Nudged Elastic Band Method 55
5.1 Abstract 55
5.2 Introduction 56
5.3 Generalized NEB Algorithm 59
5.3.1 Stress and Strain 62
5.3.2 Coupling Cell and Atomic Variables 65
5.3.3 Method Details 67
5.4 Application 68
5.4.1 CdSe Solid-Solid Transformation 68

5.4.2 Invariance of converged paths to cell geometry 72
5.4.3 Crossover to a localized mechanism 74
5.4.4 CdSe solid-solid transition using DFT 76
5.5 Discussion 77
5.6 Conclusion 79
5.7 Acknowledgments 80

Chapter 6. From Graphite to Diamond: Reaction Pathways of the Phase Transition 81

6.1 Abstract 81
6.2 Introduction 81
6.3 Method 83
6.4 Results 85
6.5 Discussion 90
6.6 Conclusion 92
6.7 Acknowledgments 92

Chapter 7. Mechanism of the $CaIrO_3$ Post-Perovskite Phase Transition Under Pressure 93

7.1 Abstract 93
7.2 Introduction 93
7.3 Method 97
7.4 Results 98
7.5 Discussion 107
7.6 Conclusion 108
7.7 Acknowledgments 109

Chapter 8. Solid-State Dimer Method for Calculating Solid-Solid Phase Transitions 110

8.1 Abstract 110
8.2 Introduction 110
8.3 Methodology 113
8.3.1 Generalized Cell and Atom Configuration Space . . . 113
8.3.2 Solid-state Dimer Method 116

8.4 Results 119
8.4.1 CdSe energy landscape 121
8.4.2 A combined dimer and NEB approach to find complex pathways 123
8.4.3 A15 to BCC solid-solid transformation in Mo 124
8.5 Conclusion 127
8.6 Acknowledgments 128

Bibliography **130**

List of Figures

2.1 Band gaps from DFT+U and HSE 14
2.2 Trends of oxygen loss from experiments 16
2.3 Oxygen binding energies and net charges 16
2.4 DOS without oxygen loss 18
2.5 DOS with oxygen vacancies 20
2.6 DOS with lithium vacancies 21
2.7 Oxygen binding energies and band gaps 22

3.1 Energy landscapes for Li diffusion in $FePO_4$ 28
3.2 Voltage dependences of the rate enhancements by N/S modifications 33
3.3 DOS changes of bare and N-$FePO_4$ after lithiation 34
3.4 DOS changes of bare and S-$FePO_4$ after lithiation 35
3.5 Structures of bare and N-/S-$FePO_4$ as a Li atom intercalating 36

4.1 Na arrangements in $Na_xV_2(PO_4)_2FO_2$ with $x = 1, 2, 3$ 43
4.2 The calculated convex hull and voltage profile 44
4.3 DOS of $Na_3V_2(PO_4)_2FO_2$ and $Na_3V_2(PO_4)_2F_3$ 48
4.4 Voltage profiles of $Na_xV_2(PO_4)_2M$ with different anion (M) substitutions 48
4.5 Structures after Br substitutions 49
4.6 Na arrangements in $Na_xV_2(PO_4)_2FCl_2$ with $x = 1, 2, 3$ 50

5.1 Failure of the drag method 57
5.2 NEB force projections 60
5.3 Uniform strain in different unit cells 62
5.4 Stress comparison as doubling the cell size 64
5.5 Two transition pathways from CdSe rock-salt to wurtzite . . . 69
5.6 Comparison of algorithms along the atom-dominated path . . 70

5.7 Comparison of algorithms along the cell-dominated path . . . 71
5.8 Invariance of the MEP under different cell representations . . 72
5.9 Scaling of the energy barrier with system size 73
5.10 MEP of a nucleation-like mechanism in a 2912 atom cell . . . 75
5.11 MEPs of concerted mechanisms within DFT 77

6.1 Enthalpy landscapes and nucleation structures of RG-CD and HG-HD phase transitions 84
6.2 The smallest nuclei of bct C4, M, and Z-carbon 87
6.3 Brønsted-Evans-Polanyi relationship for nuclei formation . . . 87
6.4 Pressure dependences of the maximum barriers 89

7.1 Properties along the MEP of $CaIrO_3$ Pv to pPv phase transition at zero pressure 99
7.2 Atomic mechanism of Pv to pPv phase transition 100
7.3 MEPs under different compression conditions 103
7.4 MEP at 30 GPa isotropic pressure and computed properties along the path. 105
7.5 MEP of a larger supercell at zero pressure 106
7.6 Structures of the intermediate and final minima in the larger supercell 106

8.1 Several phase transition mechanisms in CdSe found by the SSD 118
8.2 Two pathways from the WZ to RS structure 120
8.3 Disconnectivity graphs of the eight atom CdSe system 120
8.4 Two concerted mechanisms of the A15 to BCC phase transition in Mo 124
8.5 A localized nucleation and growth mechanism for the A15 to BCC phase transition in Mo 125

List of Tables

2.1 U values for transition metals considered 14

4.1 Partial atomic charges from a Bader analysis. 47

Chapter 1

Introduction

A journey of a thousand miles begins with a single step. –Laozi

This dissertation is a collection of the work I have done during my Ph.D. study in physical chemistry at the University of Texas at Austin. It is the milestone of my graduate study, but in the long run, it is also the first step of my scientific career. The same logic applies to the study of chemical reaction pathways, the major topic of this thesis: depending on how closely we need to look into the reaction mechanisms, different ruler scales (miles or steps) should to taken to appropriately measure the meaningful distances in a configuration space. The seven chapters are seven self-contained papers I have published, all of which are related to the exploration of potential energy landscapes. The first three chapters focus on the applications in lithium ion battery systems, where the reactions are investigated step by step. The last four chapters focus on the mechanisms of solid-solid phase transitions, where smaller scale (coarse-grained) maps are needed to efficiently navigate the broader landscapes.

1.1 Lithium/sodium ion batteries

The lithium ion batteries have been widely used for energy storage in portable electronic devices and now even in electric vehicles. By replacing lithium with cheaper sodium, the system can also be made economically efficient for use in large-scale energy storage in electrical grids. The increasing demands for larger capacity and higher charging/discharging rate per unit weight, as well as better cyclability and safety, drive the development of new battery materials. Computational simulations are playing an import role in understanding reaction mechanisms at the atomic scale in the batteries and giving new directions for further experiments.

A lithium ion battery consists of three major components: the cathode, the anode and the electrolyte. During discharging, lithium atoms spontaneously move from the anode to the cathode. The energy difference between lithium in these two electrodes is the work available to the outside circuit. More specifically, the lithium binding energy difference in the two materials determines the battery voltage, and the number of available sites for lithium in lattice determines the battery capacity. The electrolyte is electron insulating with large band gap but lithium ion conducting, which forces electrons to separate from lithium ions and travel through the metal wire of the electrical circuit. The cathode and anode are host materials that barely change their structures upon lithiation or delithiation, and thus the discharging and charging reactions are ideally completely reversible. The cathode is relatively more energetically favorable to host lithium. The cathode and anode are electrically

neutral in the bulk, as well as the electrolyte far from interfaces. On the interfaces, small amounts of net charge can accumulate as the system fluctuates away from equilibrium, which only affects the kinetics and is ignorable under small charging/discharging currents. Therefore, before intercalating into the electrode, Li^+ from the electrolyte has to recombine with an e^- on the interface, which is usually a highly electrically conductive carbon layer coated on the electrode. Without carbon coating, the recombination of Li^+ and e^- could become the rate limiting step. In our simulations, we assume that lithium intercalates as a neutral atom, and then in the host material, the electron from lithium redistributed according to self-consistent electronic structure calculations. The applied voltage that controls the direction (charging or discharging) and rate of lithium intercalations is understood as the amount of work put into the system per electron passing the outside circuit, which effectively changes the energy difference between the initial and final state (lithium being in the cathode or anode) during cycling. Under equilibrium, i.e. the zero current limit, the input and output work exactly cancels and the effective energy difference between lithium in the cathode and anode is zero. Inputting work to the system can be thought of as connecting the system to another exothermic reaction (another battery), and thus an electric field is not necessarily present.

The first three chapters discuss three cathode materials, which are all transition metal compounds. Actually nearly all the cathodes include transition metals. Regular density functional theory (DFT) tends to artificially delocalize electrons due to the self-interaction errors, thereby giving qualita-

tive inaccurate pictures in describing the localized d and f electrons, especially the 3d ones. An U term based on the Hubbard model, which accounts for the on-site Coulomb repulsion, is needed to capture the qualitatively correct electronic structures and then the correct forces between atoms. With the help of modern supercomputers, chemically accurate energy landscapes of these cathodes can be depicted under the GGA+U framework. Consequent modifications of the landscapes can be made towards desired features by changing certain elements of the materials.

1.1.1 Calculations of oxygen stability in lithium rich layered cathodes

Stability or cyclability is a big issue for the cathode materials. In many layered compounds oxygen evolution becomes spontaneous as lithium concentration drops during charging. For example, $LiCoO_2$ can only be safely charged to $Li_{0.5}CoO_2$ to avoid any irreversible structure change, which limits the practical capacity to be half of the theoretical value. This is also the reason that keeping the laptop battery fully charged accelerates its capacity decay. Similar problems exist in $LiNi_{0.5}Mn_{0.5}O_2$. To suppress the structure collapse of these layered compounds during charging, Li_2MnO_3 is introduced as an electrochemically inactive structure component to support the whole framework, because Mn^{4+} is supposed to be in the highest oxidation state and thus its lithium are difficult to extract. However, oxygen loss is still observed in the mixed compound, which shows clearly as a plateau in the voltage profile. It is also found that Ti substitution in the transition metal

layer reduces the plateau while Co increases the plateau. In this chapter, we attribute the plateau length to the strength of oxygen binding in the material and qualitatively explain the trend of oxygen loss upon substitution of Mn with other transition metals.

1.1.2 Enhanced Rate performance by Anion Surface Modification of $LiFePO_4$

$LiFePO_4$ is a cathode material with excellent stability developed in Dr. Goodenough's group in Austin. Compared with the layered materials, $LiFePO_4$ has a three dimensional framework with one dimensional lithium channels along the [010] directions. The rate performance of this material has always been a problem. The first issue is that $LiFePO_4$ is an insulator, which dramatically reduces Li^+ and e^- recombination. As we mentioned above, the cathode can only accept neutral atoms for intercalations. Consequently, the overall discharging rate is limited by electron transfer, or more specifically the combination of Li^+ and e^- on the surfaces of the cathode particles. This issue is solved by coating the cathode with electron conducting carbon which provides easy pathways for e^- to meet with Li^+. After that, slow lithium atom diffusion is the bottleneck of the rate performance. Another success that finally commercialized this cathode is reducing the particle size by nano-engineering to shorten the lithium diffusion length. But mechanisms behind the relatively low lithium diffusion rate still remain unclear, which holds off further improvements. Several factors have been proposed as the possible rate limiting step, including lithium-iron antisite defects that block some lithium

diffusion channels and the separation of lithium-rich and lithium-poor phases. There is a lot of debate on the phase separation topic, for example: whether there are two phases or not; if two phases form, whether it follows the core-shell or the domino cascading mechanism. In this chapter, we study the rate performance from the energy landscape perspective. With a pathway of atomic resolution, we find lithium occupying the surface site is the highest energy state along the diffusion path and can be used to approximate the overall barrier for small particles. Any surface modification that enhances lithium binding on the surface can thus improve the rate performance.

1.1.3 Theoretical Study of Vanadium-Based Fluorophosphates Cathodes for Rechargeable Batteries

Sodium is significantly more abundant in earth's crust than lithium. Therefore sodium ion batteries attract attention for large-sale energy storage. Because of the larger weight compared to lithium, sodium cathodes usually have a slightly smaller gravimetric energy density. Some people argue that the bigger mass of sodium also causes slower diffusion and lower rate performance. However, diffusion is a chemical reaction following statistical laws rather than a physical movement governed by a single dynamical trajectory. For any chemical reaction in solids, which is a rare event, the rate is mainly determined by the energy barrier. Sodium atoms are also about thirty percentage larger in volume than lithium atoms, and therefore require larger space in the host material to be accommodated. The bigger volume does not necessarily mean slower diffusion either. In some layered materials, sodium has a

lower diffusion barrier than lithium. Regarding diffusion, there are two competing effects related to the size: if the diffusing atom is too big compared to the channel, Pauli repulsions contribute most to the barrier; if the atom is too small, weakening of Coulomb attractions at the saddle point raises the barrier. In some materials, sodium could diffuse much faster than lithium because its radius is just right compared to the size of the diffusion channel.

1.2 Solid-solid phase transitions

Solid-solid phase transition is an interesting and challenging topic. It involves understanding material degradation mechanisms and synthesizing new materials under pressures. For example, Li_2MnO_3 undergoes layered-to-spinel phase transition during charging; graphite can be transformed into diamond at high temperature under extraordinary high pressure. The challenge for simulation comes from the enormous number of atoms in solid materials. Periodic boundary conditions, i.e. cell vectors that represent translational symmetry, are usually adopted to efficiently describe bulk, which works perfectly for equilibrium property calculations. While during phase transitions, the solid system may have cell vector changes as well as atom movement. These two types of variables need to be treated in an unbiased way to correctly represent the reaction coordinates of the transitions. Therefore, a generalized configuration space spanned by both cell and atomic degrees of freedom is introduced, along with a metric for proper distance measurements. The nudged elastic band and the dimer method are then adapted into the generalized space.

1.2.1 A Generalized Solid-state Nudged Elastic Band Method

Previous efforts on calculating barriers of solid-state phase transitions have successfully explained some important experimental phenomena, but the methods employed cannot be directly extended to general cases. In these studies, either the cell or atomic degrees of freedom are preselected as the primary reaction coordinates and the unselected ones are fully relaxed as the main coordinates change, which are typical drag methods. It is well known that the drag variables have to be choose carefully, otherwise the atomic motion could be noncontinuous and the reaction path calculated would be unphysical. Without prior knowledge of the system, applying any kind of drag method is risky. Moreover, some phase transitions may involve both cell and atomic motion at the same time, for example a nucleation and growth process, that dragging either of them would not give the proper reaction pathway. In this chapter, a generalized solid-state nudged elastic band (G-SSNEB) method is developed, which treats the cell and atomic degrees of freedom on the same footing. It is revealed by the method whether the transition is cell-dominated, atom-dominated, or neither, rather than predefined. With this advantage, a minimum energy path of the nucleation process in the CdSe rock salt to wurtzite phase transition is calculated for the first time.

1.2.2 From Graphite to Diamond: Reaction Pathways of the Phase Transition

Several puzzles are still unsolved in understanding the kinetics of the phase transition from graphite to diamond. Cubic diamond is the most stable structure among carbon allotropes, while many other structures can exist for a long time due to kinetic barriers. For example, graphite is the most common meta-stable phase. With the help of high pressure techniques, more meta-stable structures are being synthesized in experiment, because the enthalpy landscapes can be modified by the work term (PV) to tilt towards configurations with smaller volumes. Barriers may also increase or decrease by pressure depends on the reaction paths. The so-called cold compressed graphite (CCG) is a new allotrope synthesized at room temperature by compressing graphite to 17 GPa, whose exact structure is unsolved. Since low temperature means a extremely low barrier to overcome, using G-SSNEB to calculate the barriers from graphite to different candidate structures could help to identify the CCG. Another interesting observation is that heating graphite under 15GPa pressure, a hexagonal diamond structure forms at lower temperature than the cubic diamond, which indicates a higher barrier for the latter phase transition. While previous theoretical studies were limited to concerted mechanisms and found the opposite barrier order. With G-SSNEB, we show the phase boundary that was missed in the concerted mechanism is responsible for the discrepancy.

1.2.3 Mechanism of the $CaIrO_3$ Post-Perovskite Phase Transition Under Pressure

In this last application of the G-SSNEB, roles of external stresses in changing reaction barriers are discussed. Applying isotropic pressure always stabilizes the compact phase, but does not necessarily reduce the transition barrier. Whether the pressure decreases or increases the barrier depends on the angle between the reaction pathway and the pressure. When $CaIrO_3$ transforms from the perovskite to the more condensed post-perovskite phase, the volume needs to increase first to allow for IrO_6 octahedron rotations, which raises the barrier under moderate isotropic pressures. Keeping adding pressures finally shifts the transition path from IrO_6 rotations to direct IrO_6 compressions, from where the barrier starts to decrease with the pressure. While shear stress always facilitates the transition towards the post-perovskite phase, which agrees with experimental observations.

1.2.4 Solid-State Dimer Method for Calculating Solid-Solid Phase Transitions

Extended from the G-SSNEB method, a solid-state dimer (SSD) method is developed for single-ended saddle point searching in the generalized configuration space. Different from the NEB method, where both the initial and final states are needed to launch a saddle search, the dimer method only requires information of one state and can locate low lying saddle points to escape the state. Then structures of product states are obtained by minimizing the energy from the saddles found. This procedure makes the exploration of energy

landscapes more automatic and less biased. In studying phase transitions, how atoms in the final phase corresponds to those in the initial phase is burdensome to sort out manually. Moreover, the choice of cell for each phase is not unique, which further increases the complexity of the atomic mapping. To set a plausible initial phase transition path for SSNEB becomes a big hurdle to study a new phase transition. The SSD does not have this issue since it traces the atom and cell movement from a single initial point in the generalized space. Combining the SSD with the adaptive kinetic Monte Carlo method (AKMC) in the EON software, new phase transition mechanisms and crystal structures can be found more easily.

Chapter 2

Calculations of oxygen stability in lithium rich layered cathodes

2.1 Abstract

Oxygen loss can lead to high capacity Li_2MnO_3-based lithium-rich layered cathodes. Substitution of Mn with other transition metals (Ti and Co) significantly affects the amount of oxygen loss and capacity during the first charge/discharge cycle. An explanation of these results is provided with density functional theory (DFT+U) electronic structure calculations. Oxygen is found to bind more strongly to Ti and more weakly to Co. The influence of the substitution is attributed to changes of the band gap. Ti lifts the non-bonding band and increases the band gap of the compound, thus raising the energy required to redistribute the electrons released upon oxygen loss. Co lowers the non-bonding band and facilitates oxygen loss.

2.2 Introduction

Li_2MnO_3-stabilized $LiMO_2$ (M=Mn, Co, Ni) materials are promising cathodes for Li-ion batteries due to their higher capacity and stability as compared to the parent $LiMO_2$ layered oxides [1]. The stabilized compounds have

a similar structure as $LiMO_2$ except that excess Li populates the transition metal layer. This is made clear using the notation, $Li[Li_{1/3}Mn_{2/3}]O_2$, where [...] indicates the composition of the transition metal layer; in this example 1/3 of the Mn atoms are replaced with Li. In the endpoint material, Li_2MnO_3, Mn^{4+} cannot be oxidized further. It has been shown that the oxidation of O^{2-} to O_2 compensates for electrons in charging process [2, 3, 4]. For the stabilized materials, it was expected that the compensating electrons would only come from $LiMO_2$ (M=Mn, Co, Ni) where M can be oxidized to a +4 state. Interestingly, oxygen loss is still observed, and it continues after all the transition metals are fully oxidized [5, 6]. This oxygen loss results in a higher capacity than either of the endpoint materials so it is important to determine the factors that affect it.

In a previous paper, $Li[Li_{0.2}Ni_{0.2}Mn_{0.6}]O_2$ was synthesized and the influence of different transition metal ions on oxygen loss during the first cycle was studied [6]. The results shows that oxygen loss is sensitive to the substitution: introducing Ti into the transition metal layers reduces oxygen loss while Co promotes it. The explanation provided is that a greater overlap between the $Co^{3+/4+}$ t_{2g} and O^{2-} 2p bands leads to more metal-O covalency, more delocalized electrons, and a reduced stability of O^{2-} ions; whereas less overlap between the $Ti^{3+/4+}$ t_{2g} and the O^{2-} 2p bands leads to less metal-O covalency, more localized electrons, and an increased stability of O^{2-} ions. Here we employ density function theory (DFT) calculations to explain the experimental results, and test this model from the perspective of oxygen binding

Table 2.1: The U values for different transition metals (TMs).

TM	U_{eff}	Ref.	TM	U_{eff}	Ref.
Co	5.1	[7]	V	4.0	[8]
Mn	5.0	[9]	Cr	3.5	[10]
Ti	4.2	[11]	Fe	4.3	[7]
Ni	5.96	[9]			

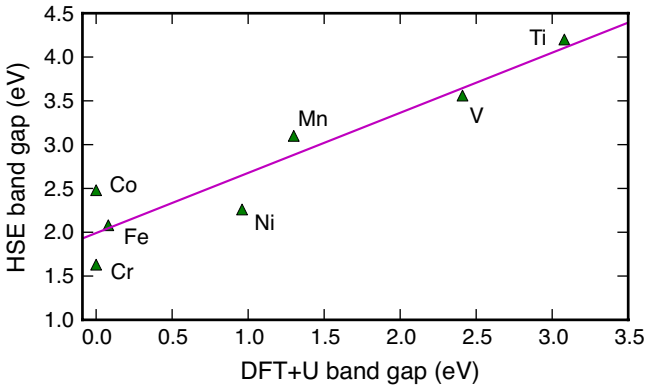

Figure 2.1: Correlation between band gaps of Li_2MO_3 calculated with DFT+U and the HSE functional.

and electronic structure calculations.

2.3 Computational Method

To simplify the calculations, we modeled the endpoint material $Li[Li_{1/3}Mn_{2/3}]O_2$ and then substituted Mn with other transition metals. All transition metals modeled are in their +4 state, which represents the chemical environment where oxygen loss occurs. DFT+U calculations were conducted using Vienna ab-initio simulation package [12]. The generalized gradient approximation with PW91 functional was chosen to describe electron exchange and correlation [13].

All calculations included spin-polarization. Core electrons were incorporated into pseudopotentials with the projector augmented-wave method [14, 15]. Valence electrons were described with a plane wave basis set with an energy cutoff of 400 eV. A 2×1×1 super-cell was chosen to represent the periodic crystal. All atoms were allowed to relax, but no gross structural rearrangements were considered. A Monkhorst-Pack k-point mesh of 2×4×4 was set for oxygen binding energy calculations, and a 6×12×12 mesh for density of states (DOS) calculations. An on-site Hubbard term (U) was used for the transition metals to avoid the delocalization of 3d electrons as a result of self-interaction. The effective U values (U_{eff}=U−J) were taken from the literature; they are summarized in Table 2.1. A comparison of band gaps calculated with DFT+U and the Heyd-Scuseria-Ernzerhof (HSE06) hybrid functional [16] are plotted in Fig. 2.1. The HSE band gaps are expected to be in fairly good agreement with experiment, without relying on any material specific fitting parameters [17]. Although DFT+U underestimates the band gap as compared to HSE, the correlation between the two methods validates the use of DFT+U and the literature values of U_{eff} used for our analysis. Local charges were calculated using a grid based Bader analysis method [18, 19].

2.4 Results

The effects of Ti and Co doping on oxygen loss in the first cycle are summarized in Fig. 2.2 [6]. The width of the plateau at 4.5 V corresponds to the amount of oxygen loss. When Mn is substituted for Ti the plateau

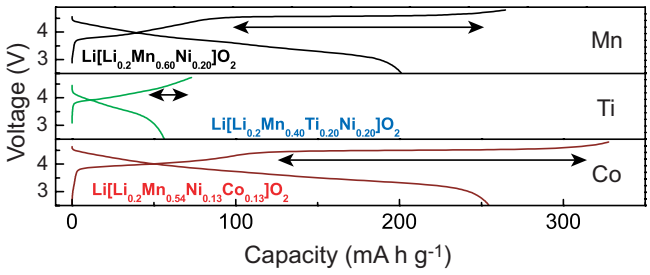

Figure 2.2: Charge/discharge curves of different compounds from Ref. [6], showing how Ti suppresses oxygen loss and Co increases it.

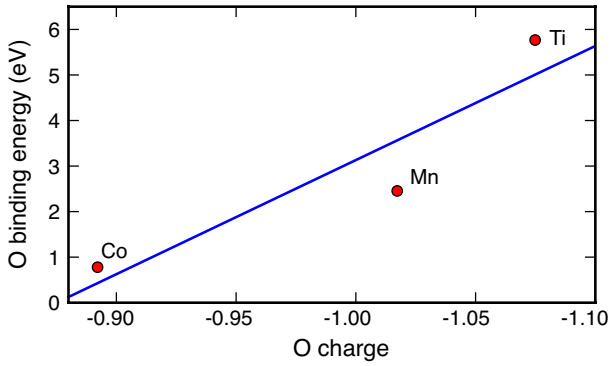

Figure 2.3: Correlation between oxygen binding energy and the oxygen net charge.

increases (indicated by the arrows in the figure); the opposite is observed for Co substitution.

The oxygen binding energy is a direct indicator of oxygen stability in different compounds. A stronger oxygen-metal bond makes it harder for oxygen to leave the material. Using DFT, the oxygen binding energy is calculated as the energy of the following reaction

$$\mathrm{Li_{2x}M_xO_{3x}} \rightarrow \mathrm{Li_{2x}M_xO_{3x-1}} + \frac{1}{2}\mathrm{O_2}. \tag{2.1}$$

Our model uses a value of x=4 and an oxygen vacancy concentration of 8.3%.

The low concentration reduces the interaction of vacancies between periodic images so that the calculations correspond to the onset of oxygen loss, thus simplifying the analysis. The oxygen binding energy of $Li[Li_{1/3}M_{2/3}]O_2$ (M = Co, Mn, and Ti) are shown in Fig. 2.3. Ti substitution is found to increase the oxygen binding energy while Co decreases it, which agrees well with the experimental trends. The average net charge on the oxygen atoms, which is the total electric charge calculated with a Bader analysis minus the number of protons in the nucleus, is also shown to correlate with the oxygen binding energy. This trend has been understood in terms of the degree of covalency between the O and transition metal [6]. Transition metals that are more electropositive result in more ionic oxygen-metal bonds. When the bonding electrons are relatively more localized on oxygen atoms, these oxygen atoms are difficult to remove and the material is harder to oxidize. Transition metals which are less electropositive lead to a greater degree of covalency with oxygen and a greater tendency for oxygen loss.

Trends in oxygen stability can be directly understood from the electronic structure of the oxide materials, and specifically how the density of states changes with the transition metal, as shown in Fig. 2.4(a). One thing worth noting is that the valence bands consist of both oxygen and metal character, with oxygen dominating. There is more metal contribution in the valence band for Co, which suggests more overlap between the Co and O bands and a greater covalency. Both Mn and Ti have a greater ionic character. In all three compounds, the conduction band primarily consists of non-bonding

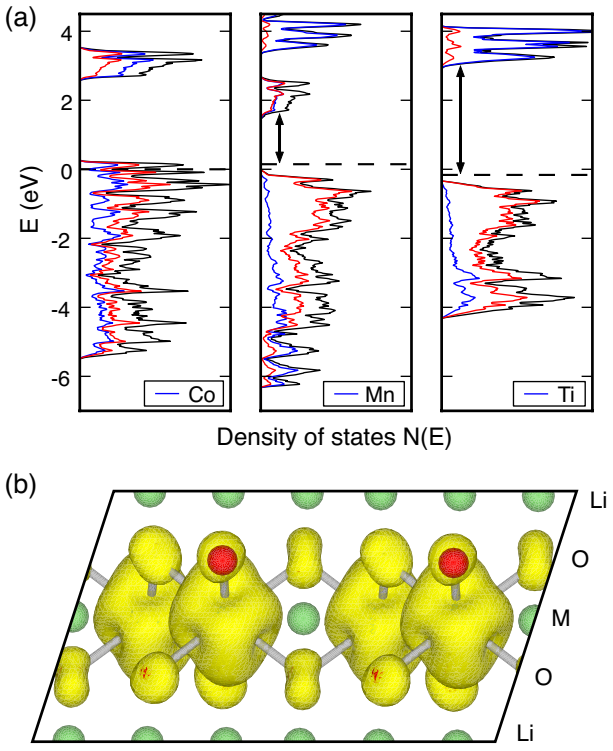

Figure 2.4: (a) Density of states of $Li[Li_{1/3}M_{2/3}]O_2$, where M is Co, Mn or Ti. In each plot, the black curve is the total density; red and blue are the partial density of oxygen and the transition metal; and the dashed black line indicates the Fermi-level. The band gap increases from left to right, which follows the oxygen binding energy trend (note that $Li[Li_{1/3}Co_{2/3}]O_2$ is calculated to be a metal). The energy levels are alined by the low-lying oxygen 2s states. (b) Electron density isosurface (yellow) of the lowest unoccupied molecular orbital (LUMO) in $Li[Li_{1/3}Ti_{2/3}]O_2$. The green spheres are Li and the red are O. The concavity along the bond directions shows the non-bonding character of the LUMO.

or anti-bonding metal states. The nuclear positive charge increases from Ti to Co and the metal states lower in the DOS due to an increased Coulomb attraction. For Co, the non-bonding states overlap with the valence states and the band gap vanishes.

The band gaps of the three compounds are also found to positively correlate with their oxygen binding energy. This is not surprising: when an O atom is removed from the material, the localized electrons on the O, which occupied states below the Fermi level, must be accommodated in unoccupied states. The differences in energy for oxygen removal between the different compounds can then be correlated to the band gap. This model is supported by calculations of the DOS of $Li[Li_{1/3}M_{2/3}]O_{2-x}$ shown in Fig. 2.5(a). Removal of an O atom releases two electrons to the crystal which occupy a new state above the Fermi level. In $Li[Li_{1/3}Ti_{2/3}]O_{2-x}$, this new state is localized in an orbital with d_{z^2} character on the two Ti centers neighboring the O vacancy. The d_{z^2} states on Ti mix with the p_z states of the missing O in the metal-oxide valence band. The other end of the Ti-d_{z^2} orbitals point to occupied O-p_z orbitals. The node between the Ti-d_{z^2} and O-p_z orbitals indicates the anti-bonding character of the state. A small portion of the state is locating on the second nearest neighbor Ti atom, with t_{2g} symmetry, which indicates non-bonding character. To summarize, the electrons left behind upon O loss in $Li[Li_{1/3}Ti_{2/3}]O_{2-x}$ are in a non-bonding/anti-bonding mixed state.

The density of states also shows why oxygen loss is enhanced upon delithiation. In Fig. 2.6, removal of a Li atom in $Li_{1-x}[Li_{1/3}M_{2/3}]O_2$ creates

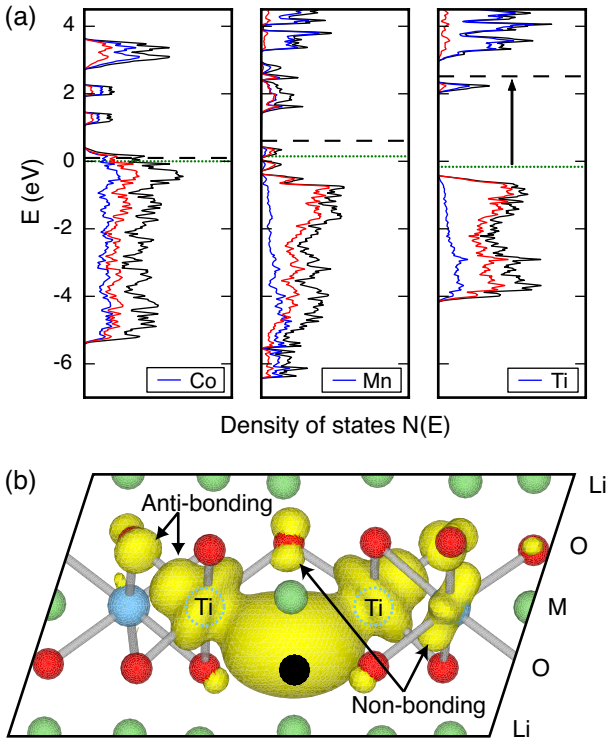

Figure 2.5: (a) DOS of $Li[Li_{1/3}M_{2/3}]O_2$ with an oxygen vacancy in the supercell. The black dashed line shows the increased Fermi level after oxygen removal as compared to before, shown by the green dotted line. (b) The electron distribution of the highest occupied orbital created by oxygen removal in $Li[Li_{1/3}Ti_{2/3}]O_2$. Green spheres are Li, red are O; blue Ti; and black is the O vacancy.

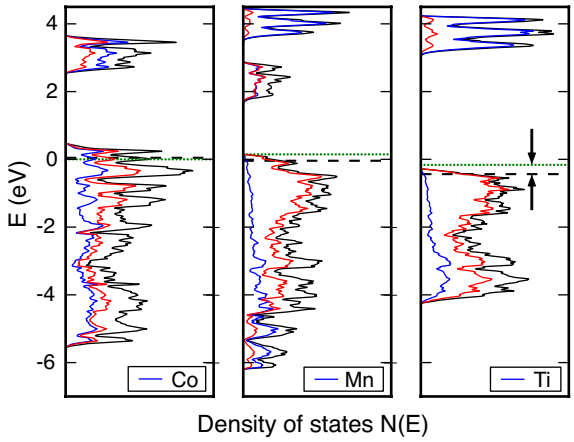

Figure 2.6: DOS of $Li[Li_{1/3}M_{2/3}]O_2$ with a lithium vacancy in the supercell. Fermi levels drop from the green dotted lines to the black dashed lines. All of the three materials are conductors now.

an electronic hole and lowers the Fermi level so that the material becomes a conductor. Since the band gap is zero, oxygen loss is facilitated by the low lying unoccupied states. This explains why $Li[Li_{1/3}M_{2/3}]O_2$ is inactive as a cathode material.

The correlation between the band gap of $Li[Li_{1/3}M_{2/3}]O_2$ and the binding of oxygen extends over the first-row transition metals, as shown in Fig. 2.7. These calculations indicate that Fe and Cr could be potential doping elements for $Li[Li_{1/3}Mn_{2/3}]O_2$, besides Ni and Co. V, on the other hand, should stabilize oxygen as compared to Mn.

2.5 Conclusion

We have explained the effect of transition metal substitutions on oxygen loss in lithium-rich layered oxides from the electronic structure calculated

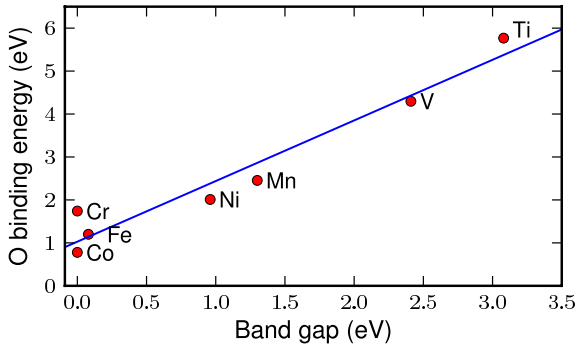

Figure 2.7: Correlation of oxygen binding in $Li[Li_{1/3}M_{2/3}]O_2$ with the band gap. The band gaps are calculated as the energy differences between the bottom of the conduction bands and the top of the oxygen dominating bands since the extra electrons come from the leaving oxygen. These are the conventional band gaps for all the compounds in the figure as their oxygen bands lie on the Fermi levels, except for vanadium whose highest occupied states are non-bonding metallic states.

with DFT+U. The conclusion is that the band gap of the cathode determines the oxygen binding energy, because the unoccupied metal bands provide the empty energy levels for electrons from the removed O. Ti substitution increases the band gap because the non-bonding metal band has higher energy due to the weaker nuclear attraction as compared to Mn. Thus Ti suppresses oxygen loss. Co substitution decreases the band gap because the low-lying non-bonding metallic band overlaps with the valence band and makes the material a conductor. Thus Co facilitates oxygen loss. The correlation between band gap and oxygen binding energy is further confirmed by examining other third period transition metals between Ti and Ni.

2.6 Acknowledgements

This work is supported as part of the program "Understanding Charge Separation and Transfer at Interfaces in Energy Materials (EFRC:CST)" an Energy Frontier Research Center funded by the US Department of Energy, Office of Science, Office of Basic Energy Sciences under Award Number DE-SC0001091. Calculations were done with resources from the National Energy Research Scientific Computing Center and the Texas Advanced Computing Center.

Chapter 3

Enhanced Rate Performance by Anion Surface Modification of $LiFePO_4$

3.1 Abstract

Despite the great achievement in understanding the materials properties and powder engineering of $LiFePO_4$, the chemical bonding at the surface has been almost ignored. Herein, we demonstrate that the under-coordinated Fe^{2+}/Fe^{3+} redox couple at the surface gives a high barrier for charge transfer, but it can be stabilized by nitrogen or sulfur adsorption. The surface modification improves greatly the charge transfer kinetics and the charge/discharge performance of the $LiFePO_4$ cathode. The rate performance enhancement is explained in the energy landscape picture from DFT calculations. Based on this understanding, we predict that during discharging the rate enhancement is a segmented function of applied voltages and it vanishes as the voltage (absolute value) decreases (the anode energy level increases). The predictions are further confirmed by following experiment where the rate constants are measured under different voltages.

3.2 Introduction

To reduce the effects of fossil fuels on global warming and air pollution, alternative energy sources at an affordable price are urgently needed. The intermittency of wind and solar energy makes mandatory large-scale energy storage as a complement to these alternative energy sources, and rechargeable batteries can provide both portable and stationary storage of the electrical energy generated from wind and radiant solar power. Moreover, rechargeable batteries that power electric vehicles offer not only a distributed energy store, which can make the cost of battery storage more acceptable, but also a relief from distributed sources of air pollution. $LiFePO_4$ offers a cathode alternative for a Li-ion battery (LIB) that contains low-cost, environmentally benign materials, is safe, and has a competitive energy density with a proven long cycle life at high rates of charge/discharge. These features make it a worthy target for further reduction of its reversible capacity loss at the highest charge/discharge rates desired for powering an electric vehicle.

A $LiFePO_4$ cathode has a theoretical capacity of 170 mAh g^{-1} and operates at a voltage V = 3.45 V versus Lithium, which is safely above the HOMO of the organic liquid-carbonate electrolyte. Moreover, the strong covalent bonding within the $(PO_4)^{3-}$ anion keeps the top of the O-2p bands well below the active redox energy, which prevents oxygen evolution at full charge even at high temperatures [20, 21, 22, 23]. Although a two-phase reaction between $LiFePO_4$ and $FePO_4$ creates a poor electronic conductivity, which lowers the electrochemical capacity at higher charge/discharge rates, carbon coating

of nanosized $LiFePO_4$ particles has largely solved this problem [24, 25, 26]. Although Li^+ diffusion is confined to 1D channels along the b-axis [27, 28, 29], the nanosized $LiFePO_4$ particles crystallize in the form of platelets with the b-axis perpendicular to the plates, which facilitates Li access to all the particle volume. With proper quality control, high-rate $LiFePO_4$ cathodes have been successfully introduced into practical LIBs of very long life. Nevertheless, there is some reversible capacity loss at high rates owing to the resistance of Li^+ transport across the electrolyte/electrode interface.

A reduction of this charge-transfer resistance by the introduction of nitrogen or sulfur to the surface of the $LiFePO_4$ particles is observed in experiment. The surfaces of bare $LiFePO_4$ and $FePO_4$ particles were modified by NH_3 gas and S vapor, and these surface-modified samples are denoted as N-$LiFePO_4$, N-$FePO_4$, and S-$LiFePO_4$, S-$FePO_4$, respectively. The particle size and the morphology were little changed by the postannealing treatments, regardless of the annealing temperatures; changes in the lattice parameters are also less than 0.05% compared to the reference values. We have undertaken a theoretical study to explain how the barrier of Li transport between the Li metal anode and the $FePO_4$ cathode is modified by the substitution of nitrogen for surface oxygen or the absorption of sulfur on the (010) surface of the $FePO_4$ platelets.

3.3 Computational Method

All the calculations were performed in the Vienna ab-initio simulation package (VASP) at the GGA+U level of theory [30, 31]. The functional for electron exchange and correlation was chosen as PW91, and the effective U value, $U_{\text{eff}} = U - J$, was set to 4.3 eV, according to a self-consistent calculation [32, 33, 34]. Core electrons were described in the projected augmented wave formalism [15]. Valence electrons were described by a plane wave basis set with an energy cutoff at 400 eV [35, 36]. A ferromagnetic spin configuration was set for the Fe ions. The supercell was constructed of 1×2 unit cells on the ac plane, and 8 layers in the b direction, with a 15 Å vacuum layer separating the periodic slabs.

3.4 Results

To correlate the presence of N and S atoms on the specific surface sites and the improved electrochemical properties, density functional theory (DFT) calculations of the surface- modified $FePO_4$ have been performed. The $FePO_4$ (010) surface is chosen for this study because it is the most stable surface and also because it exposes the b-channels that transport Li [37]. TOF-SIMS experiments show that N and S appears only on the surface of the material; nitrogen is found mainly with phosphorous as P-N, while sulfur is found with iron as Fe-S. Using these results as guidance, we replaced an O atom closest to a b-channel with a N atom in a PO_4 group in the N-$FePO_4$ case; in the S-$FePO_4$ case, we put a S atom on top of a surface Fe site, forming a Fe-S

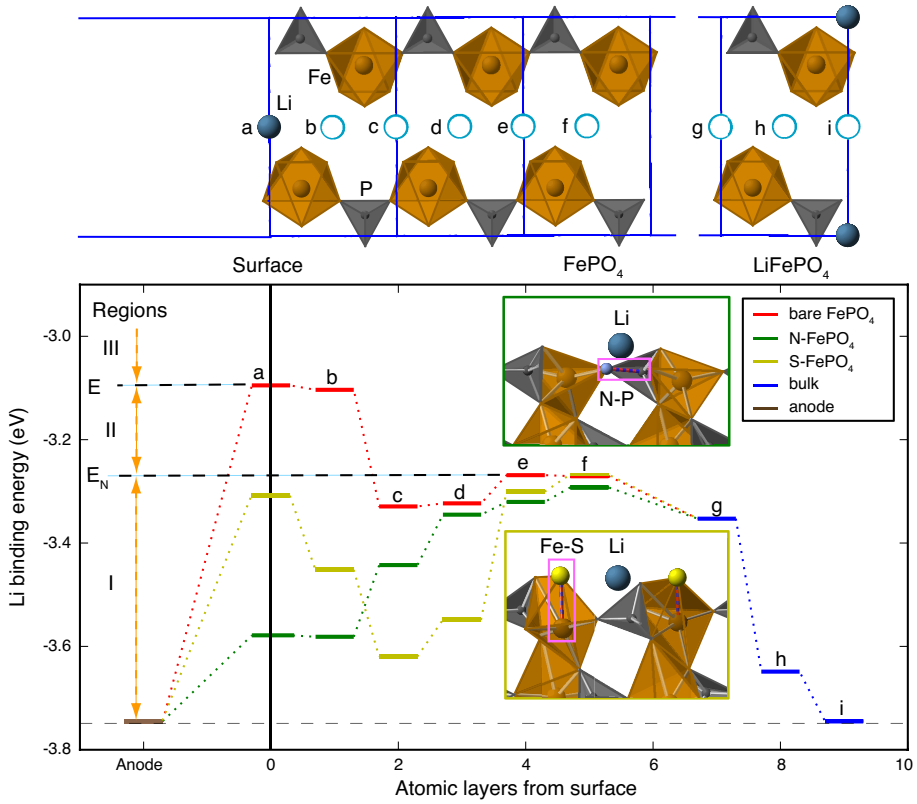

Figure 3.1: Energy landscapes of Li moving from the surface into the *b*-channel of undoped $FePO_4$ and in the presence of N and S surface dopants.

bond. These binding sites were found to be energetically favorable.

3.4.1 Explanation of the Rate Increase

Figure 3.1 shows the calculated binding energy of a single Li atom as it diffuses from the (010) surface of $FePO_4$ along the *b*-channel. In the bare $FePO_4$, Li binds weakly on the surface and subsurface sites (a- and b-sites, respectively) owing to a low coordination of Li and Fe on the surface and a structural distortion of the subsurface site. Where Li reaches an $FePO_4$ bulk

site, the binding is stronger by 0.18 eV. Li binds most strongly in the $LiFePO_4$ phase. In the $FePO_4$ phase, there is a Coulomb attraction between Li^+ and its electron, which is located on a neighboring Fe^{2+} center. In the $LiFePO_4$ phase, several Li can share the same Fe^{2+} center making the Coulomb energy correspondingly lower [38]. The binding energies for the three regions (surface, $FePO_4$, and $LiFePO_4$) are -3.10, -3.28, and -3.75 eV, respectively, consistent with values reported in the literature [37, 39].

Since the barriers for Li hopping between sites are relatively small (0.2-0.3 eV) and do not vary significantly between phases [34, 39], the binding energies along the *b*-channel can serve as the minimum energy path (MEP) for Li diffusion into and out of the material. As shown in Fig. 3.1, the weak binding of Li to the surface site determines the overall barrier for both lithiation and delithiation. Theoretically, if the voltage is below 3.75 V during lithiation, Li should be able to intercalate into the cathode and form the $LiFePO_4$ phase. In practice, however, the rate at this voltage is too low to be measured. There are two reasons for this observation: first, diffusion of Li into the material has to overcome a relatively high barrier ($3.75 - 3.10 = 0.65$ eV), and second, those intercalating Li must agglomerate to nucleate the $LiFePO_4$ phase. Only when the voltage approaches 3.28 eV does the discharge current become measurable, because at this voltage, isolated Li are stable in the $FePO_4$ phase. Both N- and S-modification decrease the total barrier by strengthen the Li binding on surface sites, thus improving the rate performance. After surface modification, the barrier is determined by the Li binding energy in the $FePO_4$ bulk phase.

3.4.2 Prediction of the Voltage Dependence

Focusing on the lithiation (discharge) processes, we can compare the rate of the bare and N-/S-$FePO_4$ to see whether experimental discharging rates match what we expect from the calculated energy landscape (Figure 3.1). If the anode energy level increases (by decreasing the applied voltage between anode and cathode), the overall lithiation barrier will change. If the anode energy level is below that of the weakest binding site, the intercalation barrier is the energy difference between these two sites. When the anode energy level is above the weakest binding site energy, there is no additional barrier above the diffusion barrier between sites, and so the intercalation rate is limited by diffusion (or other mass transport factors in the experimental apparatus).

In this high-energy anode regime, we take the diffusion barrier to be the rate-limiting barrier for Li transport from the anode to the surface site, denoted as ΔE_{N} for the N-$FePO_4$ and ΔE for the bare $FePO_4$. ΔE_{N} and ΔE are independent of the applied voltage. Next, we denote the binding energy of Li in a bulk site of N-$FePO_4$ as E_{N}, and the surface site binding energy of the bare $FePO_4$ as E. E_{N} and E are the binding energies of Li at the highest energy (weakest binding) sites for the N-$FePO_4$ and the bare $FePO_4$, respectively. The relative rate constants for the bare and N-$FePO_4$ case follows Eq. 3.1. Here we assume the same prefactor A for all the lithiation processes and use V' as a converted value of the applied voltage in eV scale ($V' = -V$

in value).

$$\frac{k}{k_{\mathrm{N}}} = \begin{cases} \frac{Ae^{-\beta(E-V')}}{Ae^{-\beta(E_{\mathrm{N}}-V')}} = e^{-\beta(E-E_{\mathrm{N}})} & \text{if } V' < E_{\mathrm{N}} \text{ (region I)} \\ \frac{Ae^{-\beta(E-V')}}{Ae^{-\beta(\Delta E_{\mathrm{N}})}} = e^{-\beta(E-V'-\Delta E_{\mathrm{N}})} & \text{if } E_{\mathrm{N}} < V' < E \text{ (region II)} \\ \frac{Ae^{-\beta(\Delta E)}}{Ae^{-\beta(\Delta E_{\mathrm{N}})}} = e^{-\beta(\Delta E-\Delta E_{\mathrm{N}})} & \text{if } V' > E \text{ (region III)} \end{cases} \tag{3.1}$$

As shown in Eq. 3.1, if $V' < E_{\mathrm{N}}$ or $V' > E$ (regions I and III) the ratio of rate constants is independent of the voltage, while in between, the ratio increases as the voltage decreases (V' increases). In region I, $V' < E_{\mathrm{N}}$, the current is too small to be measured in experiment, as discussed; in region III, the voltage is too high and the system is far from equilibrium, which may complicate the discussion. So we will compare with experiment the rate constant trend in region II, $E_{\mathrm{N}} < V' < E$.

These same arguments hold for the dependence of rate on the applied voltage in the S-$FePO_4$ case.

3.4.3 Experimental Confirmation

To estimate the rate constant k from experimental data, we assume the lithiation process as a simple first-order reaction. Because lithium diffusing into the cathode is equivalent to vacancies moving out, the rate equation is written in terms of vacancy concentration C_V. The backward reaction can be ignored when the discharge time t is small.

$$\frac{dC_V(t)}{dt} = -kC_V(t) \tag{3.2}$$

$$C_V(t) = C_V(0)e^{-kt} \tag{3.3}$$

Converting C_V to the capacity Q gives:

$$Q(\infty) - Q(t) = Q(\infty)e^{-kt} \quad (3.4)$$

$$ln(1 - Q(t)/Q(\infty)) = -kt \quad (3.5)$$

In experiment, $ln(1 - Q(t)/Q(\infty))$ vs time curves of the bare and N-/S-$FePO_4$ are found to be linear in the short-time domain [40]. In this short-time domain, the discharge reaction is interfacial charge-transfer controlled, not diffusion controlled. From the slopes of the curves, the rate constants are calculated. The ratio of the rate constants between the bare and N-/S-$FePO_4$ are plotted in Figure 3.2 to show the voltage-dependence as predicted in Eq. 3.1. The experimental trend clearly confirms the prediction. In both N- and S-$FePO_4$ cells, as the applied voltage decreases, the k/k_{N} and k/k_{S} ratio increases. At around 3.2 and 3.1 V, it reaches a plateau, where the ratio stops increasing as the voltage decreases (a transition between region II and III, where the lithium binding energy E = -3.10 eV). Since sulfur has a higher surface coverage than N, the slope of k/k_{S} may be higher than k/k_{N}.

3.4.4 Understanding Li binding at the Surface

In this section, we discuss changes to the Li binding due to surface doping. The Li binding energy has two primary contributions: the electronic part (e^-) and the ionic part (Li^+). For the bare $FePO_4$, weak binding at the surface is primarily due to the electronic contribution. In bulk, the Fe d_{z^2} orbital extends over two neighboring oxygen atoms; on the surface, Fe is undercoordinated, and its d_{z^2} orbital extends over only one oxygen neighbor. The

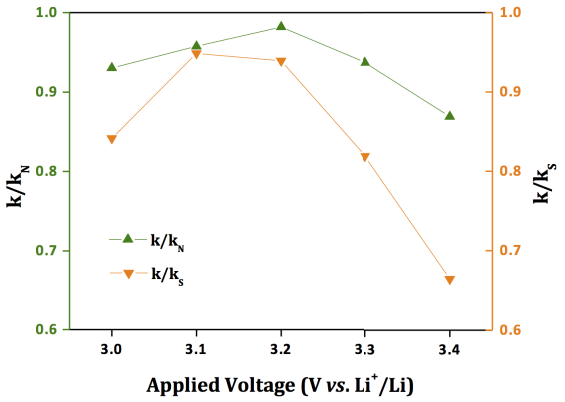

Figure 3.2: Ratio of the rate constants between the bare and N-/S-$FePO_4$. The rate equation is estimated in terms of filling up vacant Li-sites in $FePO_4$ during constant-voltage discharge by Eq. 3.5.

surface Fe-O bond is, therefore, stronger, and the energy of the corresponding anti-bonding state (populated by the extra electron from Li) is higher. In the b-site of Figure 3.1, the ionic part is responsible for weak binding. Li^+ in this is fully coordinated, but the cage space where Li^+ can sit is bigger than a bulk site. The distance between Li^+ and half of the surrounding O^{2-} is increased, raising the Coulombic energy. In the a-site, Li^+ is missing an attractive interaction from an O^{2-} center; it is also missing a repulsion interaction from an Fe^{3+} center. As a result of these two competing effects (which are comparable in magnitude), the ionic contribution of Li binding to an a-site is comparable to a bulk $FePO_4$ site.

N-doping can stabilize Li in both a- and b-sites because it affects the binding energies in both electronic part and ionic part. First, as shown in Fig. 3.3, nitrogen provides an empty 2p state in the band gap, so that the

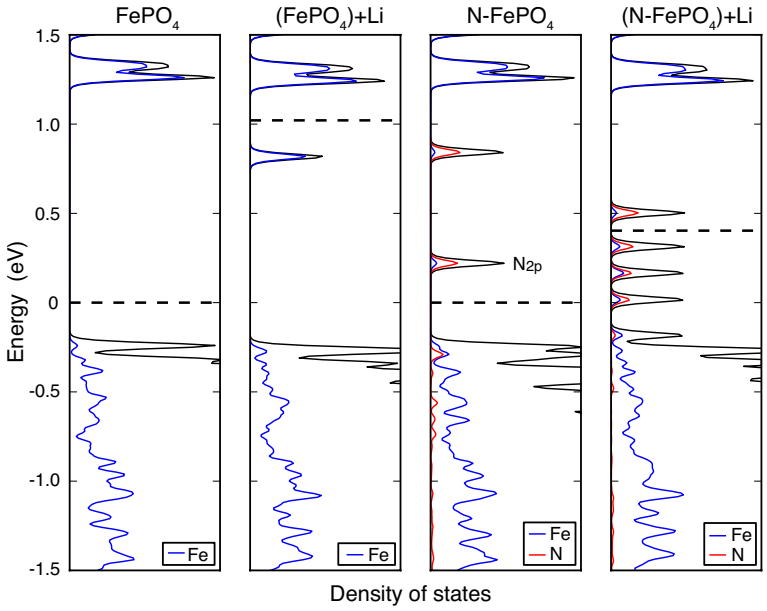

Figure 3.3: Comparison of the density of states (DOS) between the bare and N-$FePO_4$ before and after Li absorption in the a-site. The dashed lines indicate the Fermi levels. In the case of the bare $FePO_4$, the electron from Li^+ occupies an Fe state high in the band gap (compare the $FePO_4$ with ($FePO_4$)+Li DOS). In the presence of N, a lower energy state on the N atom is occupied instead; the other N-electrons feel the repulsion from the new electron and their energy levels increase (compare the N-$FePO_4$ with (N-$FePO_4$+Li) DOS).

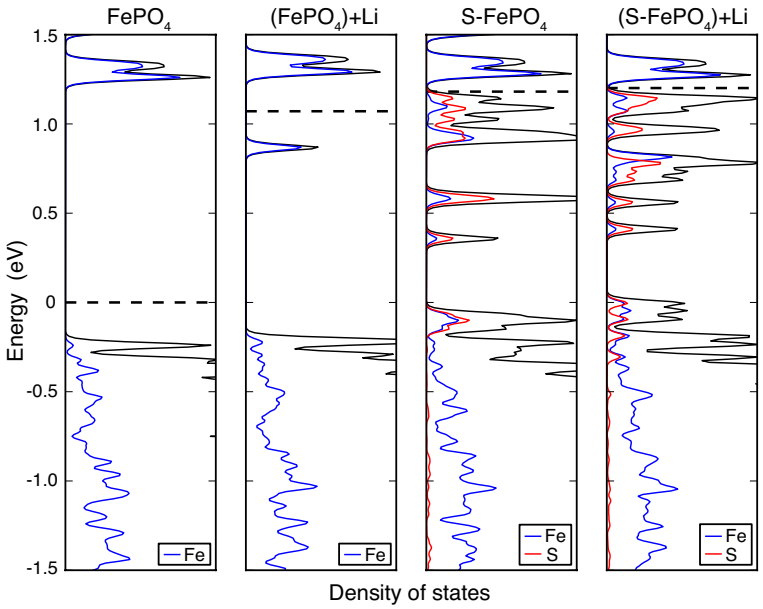

Figure 3.4: Comparison of the density of states between the bare and S-$FePO_4$ before and after Li absorption in the a-site.

extra electron coming with Li^+ does not have to go to the higher energy Fe 3d states. Nitrogen lowers the HOMO energy after Li intercalation. Second, nitrogen is more negatively charged than oxygen and has stronger Coulomb interaction with Li^+. The comparison of the atomic structures of a-, b-, and c-sites are shows in Fig. 3.5. As can be seen, Li^+ in the b-site is displaced towards the nitrogen as compared to the b-site in the bare material, showing the attractive interaction.

An analysis of the S-doped surface shows that the mechanism for increasing Li binding is different from that of nitrogen. Sulfur binds directly to a surface Fe atom, providing full coordination of the Fe center. The electronic environment of Li is similar to bulk and the binding energy is close to that of

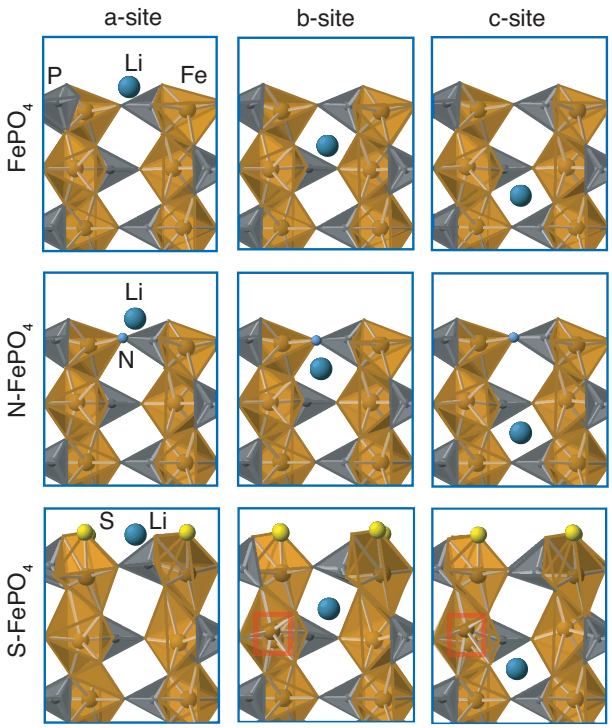

Figure 3.5: Atomic structures of a, b and c-sites for the bare and N-/S-$FePO_4$. The vertex positions are oxygen.

Li in bulk $FePO_4$. The binding of Li in the b- and c-subsurface sites increases with respect to the surface a-site. The reason is not due to the electronic structure. A comparison of the density of states (DOS) is shown in Fig. 3.4. These data show that S raises the HOMO energy level after Li intercalation, indicating that the electron binding energy is weaker. The stronger Li binding is therefore due to ionic interactions. Sulfur induces a dramatic geometric distortion to the surface. The PO_4 surface groups are rotated and the subsurface Fe centers are non-coplanar (see red box). This change in geometry gives rise to the strong Li^+ binding found in the b-, c-, and d-sites.

3.5 Conclusion

In summary, we have shown that the presence of nitrogen or sulfur on the surface of $LiFePO_4$ can greatly improve the surface electrochemistry during charge/discharge. The surface bonding state characterized with TOF-SIMS indicates that nitrogen preferably substitutes for oxygen in the $(PO_4)^{3-}$ anions and sulfur dominantly bonds to the undercoordinated Fe site. DFT calculations show that the total barrier for Li transfer is decreased by strong Li binding on surface sites in the presence of N or S. The theoretical results are backed by comparison of rate constants during potential-step chronocoulometry. For N-$FePO_4$, nitrogen can provide a more stable 2p state than surface Fe 3d state for electron transfer and also has a stronger Coulomb interaction with Li^+ owing to the more negative charge. For S-$FePO_4$, sulfur mainly stabilizes the surface Fe 3d anti-bonding states. Modification of a surface can tune

the surface energy levels and change the total barrier for the charge transfer kinetics.

3.6 Acknowledgments

This material is primarily based upon work supported as part of the program "Understanding Charge Separation and Transfer at Interfaces in Energy Materials (EFRC:CST)", an Energy Frontier Research Center funded by the U.S. Department of Energy, Office of Science, Office of Basic Energy Sciences under Award No. DE-SC0001091. TOF-SIMS data were acquired on a TOF-SIMS 5 instrument (ION-TOF GmbH, Germany, 2010) purchased through the National Science Foundation Major Research Instrumentation program (DMR-0923096).

Chapter 4

Theoretical Study of Vanadium-Based Fluorophosphates Cathodes for Rechargeable Batteries

4.1 Abstract

A single-phase crystalline $Na_3V_2O_2(PO_4)_2F$ material has been prepared by the solvothermal method. Ion exchange between Na and Li was then used to form $Na_{3-x}Li_xV_2O_2(PO_4)_2F$. The two materials were studied as positive cathodes by physical characterization, electrochemical measurements, and simulation. With density functional theory calculations, four stable phases of $Na_xV_2O_2(PO_4)_2F$ were identified at the Na concentrations of $x = 0, 1, 2, 3$. The transitions between these phases give rise to three values of the Na chemical potential and three voltage plateaus for Na intercalation. The lower two voltages, corresponding to removal of the first two Na per formula unit, agree well with the corresponding experimental electrochemical measurements. Removal of the third Na, however, is not observed experimentally because it is outside of the (4.8 V) stability window of the electrolyte. This observation is consistent with our calculations that show the last Na will only be removed at 5.3 V owing to the stability of the V-O bonding state and a strong Coulomb attraction between the Na and the anions. Computational modifications of

the material were considered to activate the third Na with an oxidation energy in the electrolyte stability window including swapping the anions from O and F to less-electronegative Cl and Br. The most promising material, $Na_3V_2Cl_2(PO_4)_2F$, is found to be stable and a good candidate as a Na cathode because all three Na ions can be reversibly removed without significant reduction in the cell potential or energy density of the material. Finally, we show that Li can replace two Na (per formula unit) and that these Li intercalate into the material with a higher rate owing to a lower diffusion barrier as compared to Na.

4.2 Introduction

Energy demand is expected to increase considerably in the coming years as a result of population growth and economic development. However, the dependence of modern society on fossil fuels is not sustainable. One driver for the development of the rechargeable Li-ion battery is the need to store electrical energy generated by wind and solar energy [41, 42, 43]. An assessment of lithium reserves reveals that most of them are located in politically sensitive areas [44], which has prompted interest in the sodium-ion battery owing to the wide availability of low-cost Na [45]. Extensive research has been reported recently on polyanion-based cathodes for a sodium-ion battery with an open framework for fast diffusion of mobile ions. Examples include sodium fluorophosphates, $NaVPO_4F$, Na_2MPO_4F (M = Fe, Mn, Co) [46], $Na_3V_2O_2(PO_4)_2F$ [47], $Na_3V_2(PO_4)_2F_3$ [48, 49], and $Li_{1.1}Na_{0.4}VPO_{4.8}F_{0.7}$ [50].

However, despite their fast ionic conduction, their low energy density makes them less attractive as electrode materials. $Na_3V_2O_2(PO_4)_2F$ as a sodium-ion battery cathode has a theoretical specific capacity of 130 mAh g^{-1} with two Na per formula unit that can be cycled reversibly. The ability to cycle all the Na would increase the capacity to 195 mAh g^{-1} [51]. While there is a lot of experimental data on vanadium-based fluorophosphate cathodes, little is known about structural variations of vanadium-based fluorophosphate cathodes during the Na/Li insertion process.

In this work, a single-phase, crystalline $Na_3V_2O_2(PO_4)_2F$ material was prepared by the solvothermal method. The $Na_{3-x}Li_xV_2O_2(PO_4)_2F$ material was subsequently obtained from $Na_3V_2O_2(PO_4)_2F$ by Na/Li ion exchange. Computer simulations were combined with electrochemical analysis in order to understand the electrochemical properties of the as-prepared materials as cathodes for rechargeable batteries and how to make these vanadium-based fluorophosphates cathodes offer a higher energy density. We suggest new polyanion frameworks in which Cl is substituted for O as a promising way to enhance the capacity of $Na_3V_2O_2(PO_4)_2F$ at the electrode without sacrificing voltage.

4.3 Computational Method

Global minima of $Na_xV_2O_2(PO_4)_2F$ for $x = 0.125, 1.0, 1.5, 2.0, 2.53.0$ were found with the basin-hopping algorithm [52]. Each move consisted of randomly swapping the position of a Na atom to the position of a vacancy site. The geometry of the trial configuration was optimized by DFT calcu-

lations and, with the resultant energy, the trial configuration was either accepted or rejected. For each possible value of x (given the small unit cell) in $Na_xV_2O_2(PO_4)_2F$, hundreds of local minima of Na arrangements were sampled.

Geometric relaxation was completed by DFT calculations with corrections for on-site Coulomb interactions of transition metals (DFT+U) using the Vienna *ab initio* simulation package [31]. The generalized gradient approximation with PW91 functional was chosen to describe electron exchange and correlation [13]. All calculations included spin polarization. Core electrons were incorporated into pseudopotentials with the projector augmented wave method, and valence electrons were described with a plane-wave basis set [14, 15]. Relaxations during basin-hopping searches were calculated with an energy cutoff of 256 eV; a higher cutoff of 333 eV was used for relaxation of the global minima for the convex hull construct. A Monkhorst-Pack k-point mesh of 1×1×1 was used during search relaxations and 3×3×2 for final relaxations. An on-site Hubbard term (U) was used for the transition metal, V, to avoid artificial delocalization of 3d electrons as a result of self-interaction [53]. The effective U value (U_{eff} = U-J) was taken from the literature, U_{eff}= 4.0 [54].

4.4 Results

Our theoretical study addresses the origin and magnitude of the voltage stop after the first two Na is removed, at what voltage the third Na would be removed if further oxidation of the framework is possible, and whether an al-

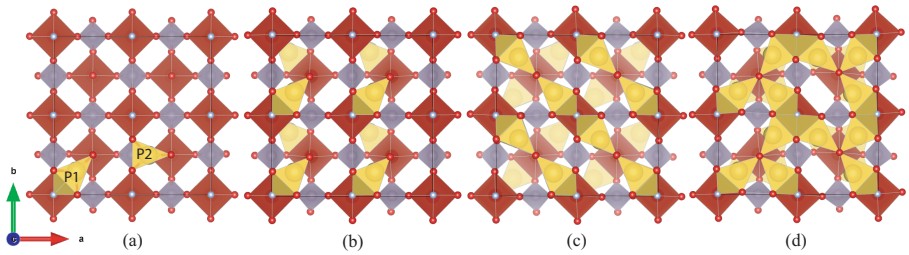

Figure 4.1: The most stable arrangement of Na in $Na_xV_2(PO_4)_2FO_2$ for different compositions, x: (a) two Na positions in the $V_2(PO_4)_2FO_2$ framework; (b) $NaV_2(PO_4)_2FO_2$; (c) $Na_2V_2(PO_4)_2FO_2$; and (d) $Na_3V_2(PO_4)_2FO_2$. The red atoms are O; blue are F; yellow are Na; the red polyhedra enclose the V atoms; and the gray enclose P.

ternative chemistry with the same framework structure can allow the third Na to be removed at a voltage in the electrolyte window without a large sacrifice in the overall average voltage. Finally, we compare the theoretical differences between Li and Na intercalation in terms of voltage profiles and the rate capabilities. For convenience of notation, we put the O bonded to V at the end of the compound formula and rewrite $Na_3V_2O_2(PO_4)_2F$ as $Na_xV_2(PO_4)_2FO_2$ to make a more direct connection to the $Na_3V_2(PO_4)_2F_3$ and $Na_3V_2(PO_4)_2FX_2$, X = -Cl or -Br, that are considered subsequently.

There are two types of sites for Na to occupy in $V_2(PO_4)_2FO_2$, as is shown in Fig. 4.1 (a): the P1 site is coordinated by six O and one F with a binding energy of 4.70 eV in the dilute limit; the P2 site is coordinated by only six O and the binding energy is 4.62 eV. The extra Na-F bond stabilizes the former site by 0.08 eV.

To calculate the voltage profile, formation energies of the material were

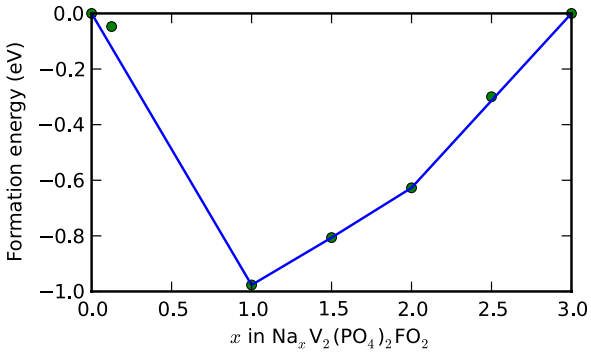

(a)

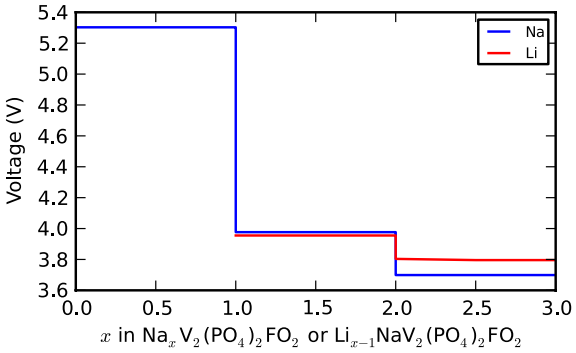

(b)

Figure 4.2: (a) Calculated convex hull plot for $Na_xV_2(PO_4)_2FO_2$ and (b) the calculated voltage for Na/Li intercalation in $Na_xV_2(PO_4)_2FO_2$/Na and $Li_{x-1}NaV_2(PO_4)_2FO_2$/Li.

calculated as a function of Na concentration. The lowest energy structures form the convex hull, of Fig. 4.2 (a). At each composition, hundreds of configurations with different Na arrangements are examined with the basin-hopping algorithm; only the lowest energy structures are plotted [55]. The convex hull clearly shows four Na-ordered phases at $x = 0, 1, 2$ and 3, each of which are illustrated in Fig. 4.1. Any other composition has a higher energy than the linear combination of these phases will, therefore, tend to decompose spontaneously into the two bracketing ordered phases on the convex hull. The voltage profile is obtained from the slopes of the convex hull [55]. The lower two voltage plateaus at 4.0 and 3.7 V match the experimental values. With less than one Na per formula unit (x<1), the intercalation voltage is 5.3 V, which is significantly above the electrochemical stability window of the electrolyte. Moreover, removal of the last Na would require oxidation of the PO_4. In order to extract the last Na, the binding of Na must be weakened in the phase where $x < 1$ and it must be possible to oxidize a redox couple without decomposition of the framework. It is also advantageous to maintain a consistently high voltage for phases allowing $x > 1$ so as not to reduce the energy density of the material.

In the traditional view, the reason that the last Na ($x < 1$) is inaccessible is that the V ion cannot be oxidized to a V^{VI} state. If the O atoms separate from the PO_4 units are replaced by halogen atoms X, the strong covalent V-O bond is replaced by a more ionic V-X bond and the formal vanadium valence becomes V^{III}. The weaker covalence of the V-X bond and the strong inductive

effect of the PO_4 complexes can be expected to lower the formal V^{IV}/V^{III} redox couple to near that of the formal V^{V}/V^{IV} couple; the replacement would also provide an oxidizable redox couple for the third Na atom per formula unit. Young-Uk Park et al. thus proposed to add more F in the formula unit as $Na_3V_2(PO_4)_2F_{1+y}O_{2-y}$ with the idea that a decrease in the V oxidation state should improve the capacity. With $y = 2$, our calculations show that the first plateau is marginally reduced from 5.3 to 4.9 V, which is still at the top of the stability voltage window of the electrolyte. As expected, recent experimental papers on $Na_3V_2(PO_4)_2F_3$ reported that only two Na per formula are active at the two plateaus, 4.1 and 3.6 V, matching our calculated values [56, 57]. These two plateaus are close to those of $Na_3V_2(PO_4)_2FO_2$, which confirms that the energy of the formal V^{IV}/V^{III} couple is indeed lowered by changing the strongly covalent V-O bond to a V-F bond in the traditional picture.

The same phenomena can also be understood from a perspective in which the V oxidation states in the two materials are the same. Adding support to this picture, the results of a charge density analysis (see Table 4.1) shows that the partial charge on V is similar for $Na_3V_2(PO_4)_2FO_2$ and $Na_3V_2(PO_4)_2F_3$ and becomes even closer when two Na are extracted. The reason that the oxidation state of V can be the same despite the different formal charges on O and F is that in $Na_3V_2(PO_4)_2FO_2$ and $NaV_2(PO_4)_2FO_2$ the negative charge on the dangling O is significantly less than on the O in PO_4 and similar to that on F. The actual charge state of the dangling O is closer to O^- than O^{2-}. Additional evidence for having the same redox couple in the two materials is

Table 4.1: Partial atomic charges from a Bader analysis.

	Dangling O/F	O in PO_4	F	V
$Na_3V_2(PO_4)_2FO_2$	-0.89	-1.37	-0.71	1.95
$Na_3V_2(PO_4)_2F_3$	-0.70	-1.39	-0.77	1.87
$NaV_2(PO_4)_2FO_2$	-0.60	-1.26	-0.68	2.03
$NaV_2(PO_4)_2F_3$	-0.62	-1.27	-0.61	2.02

provided by the calculated densities of states in Fig. 4.3. States near the Fermi level are of V character mixed with O from the PO_4 groups. The energy level and the shape of this band, which make up the V redox couple at the Fermi level, are very similar for the two materials. The states from the dangling O/F are about 2 eV lower than those of the O in PO_4, and are largely isolated from the redox couple. One can also see a hole localized on the dangling O in the DOS of $Na_3V_2(PO_4)_2FO_2$, which is not present on the dangling F in $Na_3V_2(PO_4)_2F_3$, which supports the O^- assignment from our charge density analysis.

Since the calculations are able to reproduce the measured voltages, we can then use computational experiments to try to reduce the Na binding in the $x < 1$ phase. One strategy is to replace the bridging F in $Na_xV_2(PO_4)_2FO_2$ with a less-electronegative ion such as Cl or Br. As shown in Fig. 4.4, the first plateau drops to 4.8 V and the other two plateaus drop by 0.3 V with Cl substitution. It would be just possible to extract the final Na ion and realize the extra capacity at 4.8 V for ClO_2, since it is marginally inside the electrolyte stability window. With Br substitution, the first plateau drops to 4.4 V, which is safe for common electrolytes. However, the other two (lower

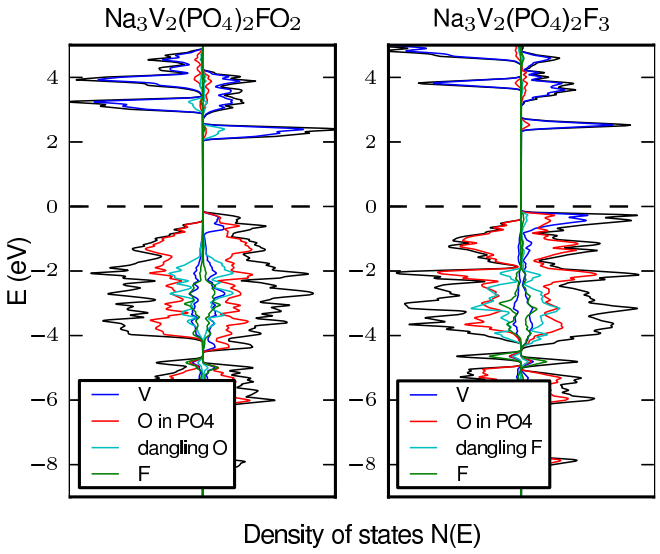

Figure 4.3: Comparison of the density of states between $Na_3V_2(PO_4)_2FO_2$ and $Na_3V_2(PO_4)_2F_3$.

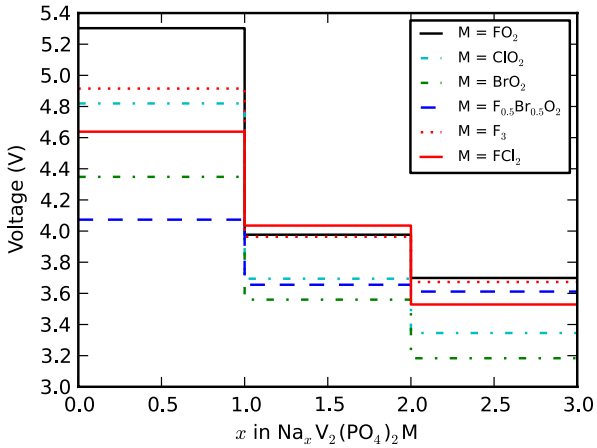

Figure 4.4: Comparison of the voltage profiles of $Na_xV_2(PO_4)_2M$ with different anion (M) substitutions.

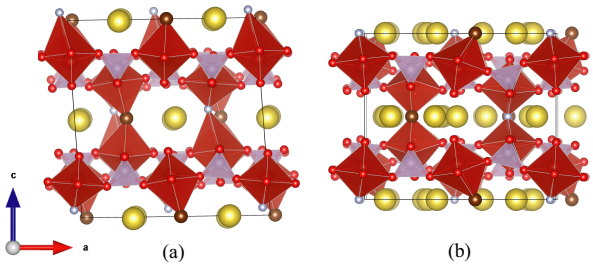

Figure 4.5: Structures of (a) $NaV_2(PO_4)_2F_{0.5}Br_{0.5}O_2$ and (b) $Na_3V_2(PO_4)_2F_{0.5}Br_{0.5}O_2$.

voltage) plateaus are also reduced by about 0.5 V, which would significantly decrease the energy density. Alternatively, $F_{0.5}Br_{0.5}O_2$ gives the most desirable voltage profile (Fig. 4.4, dashed blue line). Unlike -$F_{0.5}Cl_{0.5}O_2$, where the plateau at $0 < x < 1$ is between -ClO_2 and -FO_2, -$F_{0.5}Br_{0.5}O_2$ results in a remarkably low first plateau at 4.1 V, one that is even lower than with -BrO_2. The other two plateaus ($1 < x < 2$ and $2 < x < 3$) are higher than -BrO_2, as expected, and both are close to 3.6 V.

Side views of the structures at $x = 1$ and $x = 3$ with -$F_{0.5}Br_{0.5}O_2$ are shown in Fig. 4.5. The distortion of the structure at $x = 1$ reflects the difference of anion radii. At $x = 3$, the distortion is reduced as well as the voltage drop. While these predictions are encouraging, the difficulties associated with the synthesis of such a Br substituted material may be prohibitive. Br escaping the half-substituted material is slightly energetically favorable as calculated by Eq. 4.3. The half-substituted structure, however, is metastable

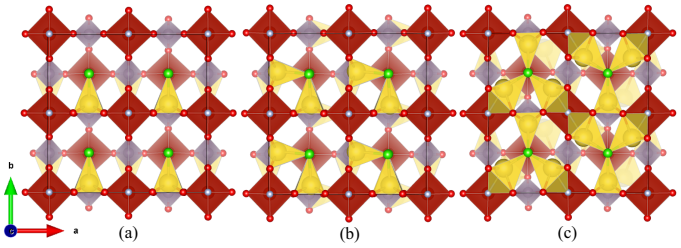

Figure 4.6: Structures of (a) $NaV_2(PO_4)_2FCl_2$ (b) $Na_2V_2(PO_4)_2FCl_2$ (c) $Na_3V_2(PO_4)_2FCl_2$. The green atoms are Cl.

and could, potentially, be synthesized.

$$(Na_3V_2(PO_4)_2ClO_2) \times 8 = (Na_3V_2(PO_4)_2Cl_{0.875}O_2) \times 8 + \frac{1}{2}Cl_2$$
$$\Delta E = 1.58 \text{ eV} \tag{4.1}$$
$$(Na_3V_2(PO_4)_2BrO_2) \times 8 = (Na_3V_2(PO_4)_2Br_{0.875}O_2) \times 8 + \frac{1}{2}Br_2$$
$$\Delta E = 0.90 \text{ eV} \tag{4.2}$$
$$(Na_3V_2(PO_4)_2F_{0.5}Br_{0.5}O_2) \times 8 = (Na_3V_2(PO_4)_2F_{0.5}Br_{0.375}O_2) \times 8 + \frac{1}{2}Br_2$$
$$\Delta E = -0.2 \text{ eV} \tag{4.3}$$

In the transition from $Na_3V_2(PO_4)_2FO_2$ to $Na_3V_2(PO_4)_2F_3$, the two O are replaced by F. Inspired by this strategy, we try occupying the oxygen sites with Cl instead of F to form $Na_3V_2(PO_4)_2FCl_2$. Compared to F, Cl is less electronegative and thus attracts less negative charge and reduces the binding to the positive Na ions. The relative binding energies at the P1 and P2 sites reverse in response to this substitution. The P2 site is more stable by 0.08 eV than the P1 site and, as a result, Na atoms order in different patterns as shown in Fig. 4.6. The voltage profile of $Na_3V_2(PO_4)_2FCl_2$ (solid red line in Fig. 4.4)

looks even better than that of -$F_{0.5}Br_{0.5}O_2$; the average voltage of the three plateaus is higher and the highest one is well within the stable electrolyte voltage window. Another advantage to substitution at the O site is that it has little influence on the framework so that the structure is more likely to be synthesized. The stability of $Na_3V_2(PO_4)_2FCl_2$ is tested computationally by considering three decomposition scenarios. Eq. 4.4 describes Cl escaping as Cl_2 leaving vacancies behind; Eq. 4.5 describes Cl being substituted by O from water. Both of these are energetically unfavorable. The last test, considering anion disorder, involves the swap of one F with Cl in 8 formula units, leaving the stoichiometry fixed, which results in a 0.54 eV energy rise. This observation means that F-Cl disorder is not expected when the Cl/F ratio is set to two. The reverse reaction of Eq. 4.5 is a possible approach to synthesize $Na_3V_2(PO_4)_2FCl_2$.

$$(Na_3V_2(PO_4)_2FCl_2) \times 8 = (Na_3V_2(PO_4)_2FCl_{1.875}) \times 8 + \frac{1}{2}Cl_2 \ \Delta E = 2.23 \text{ eV} \tag{4.4}$$

$$Na_3V_2(PO_4)_2FCl_2 + 2H_2O = Na_3V_2(PO_4)_2FO_2 + 2HCl + H_2 \ \Delta E = 2.30 \text{ eV} \tag{4.5}$$

Next, we checked computationally the stabilities of these compounds during cycling. Fully charged $Na_3V_2(PO_4)_2FCl_2$ turns out to be stable:

$$(V_2(PO_4)_2FCl_2) \times 8 = (V_2(PO_4)_2FCl_{1.875}) \times 8 + \frac{1}{2}Cl_2 \ \Delta E = 0.20 \text{ eV} \tag{4.6}$$

$$(V_2(PO_4)_2FCl_2) \times 8 = (V_2P_2O_{7.875}FCl_2) \times 8 + \frac{1}{2}O_2 \ \Delta E = 3.35 \text{ eV} \tag{4.7}$$

while O_2 formation is spontaneous when $Na_3V_2(PO_4)_2FO_2$ is fully charged:

$$(V_2(PO_4)_2FO_2) \times 8 = (V_2(PO_4)_2FO_{1.875}) \times 8 + \frac{1}{2}O_2 \ \Delta E = -0.30 \text{ eV} \tag{4.8}$$

Finally, we consider the replacement of Na with Li so that the material can be used in a Li cell. Due to the strong binding of the last Na, only two Na per formula can be substituted by Li. This result is understood both from calculations and observed in our experiment, as well as in Parks report [50]. The energy difference to replace two Na with Li (as in Eq. 4.9) is -0.079 eV; this result indicates that the reaction occurs spontaneously. The energy difference to substitute the last Na with Li (as in Eq. 4.10) is 0.073 eV, so that it will not happen spontaneously.

$$Na_3V_2(PO_4)_2FO_2 + 2Li = NaLi_2V_2(PO_4)_2FO_2 + 2Na \ \Delta E = -0.079 \text{ eV} \tag{4.9}$$

$$NaLi_2V_2(PO_4)_2FO_2 + Li = Li_3V_2(PO_4)_2FO_2 + Na \ \Delta E = 0.073 \text{ eV} \tag{4.10}$$

In order to determine the lowest energy structures containing Li, we used the basin-hopping algorithm with one Na in the formula unit as $NaLi_{x-1}V_2(PO_4)_2FO_2$ ($1 < x < 3$). The voltage profile of Li is plotted in Fig. 4.2 (b). The first plateau ($2 < x < 3$) matches the experimental value, while the second one ($1 <$x< 2) is lower by 0.2 V. The deviation might be due to subtle structural changes caused by the ion exchange.

Na/Li diffusion is studied by calculating the minimum energy paths for ion hopping with the nudged elastic band method [58, 59]. Since one Na is always trapped inside the material, one extra Na/Li atom is added to the structure (Fig. 4.1 (b)) to form $Na_{1.125}V_2(PO_4)_2FO_2$ or $NaLi_{0.125}V_2(PO_4)_2FO_2$. The motion of this extra atom is investigated to calculate the diffusion barrier. Our results agree with the literature; the barrier of Na diffusion is 0.37 eV and

the barrier to Li diffusion is lower by 0.1 eV, but the two proposed diffusion pathways from previous studies have comparable barriers because of different Na arrangements [50]. The difference in diffusion barrier between the two cations explains the better rate performance of the Li battery as observed in our experiment.

4.5 Conclusion

In summary, simple and environmentally friendly solvothermal methods provide easy routes to the synthesis of $Na_3V_2O_2(PO_4)_2F$ and then $Na_{3-x}Li_xV_2O_2(PO_4)_2F$ by ion exchange. Through first principle calculations, we have successfully explained the two plateaus in the voltage profiles of $Na_3V_2O_2(PO_4)_2F$/Na and why the third Na is difficult to be extracted either electrochemically or by chemical ion exchange. Moreover, we find a possible approach to access the third Na per formula unit is to substitute O with Cl to form $Na_3V_2Cl_2(PO_4)_2F$. This compound is calculated to be stable on removal of all the Na and possible to synthesize. Finally, we show that $Na_{3-x}Li_xV_2O_2(PO_4)_2F$ can also be used as a cathode in a Li-ion cell with an even higher rate capability.

4.6 Acknowledgments

This work is supported by the Department of Energy Office of Basic Energy Science grant (No. DE-SC0005397) and the Energy Frontier Research Center "Understanding Charge Separation and Transfer at Interfaces in Energy Materials (EFRC:CST)" (No. DE-SC0001091), The Robert A Welch

Foundation, Houston, Texas Grant number F-1066, and the National Natural Science Foundation of China (No. 21063014). Calculations were done with resources from the National Energy Research Scientific Computing Center and the Texas Advanced Computing Center.

Chapter 5

A Generalized Solid-state Nudged Elastic Band Method

5.1 Abstract

A generalized solid-state nudged elastic band (G-SSNEB) method is presented for determining reaction pathways of solid-solid transformations involving both atomic and unit-cell degrees of freedom. We combine atomic and cell degrees of freedom into a unified description of the crystal structure so that calculated reaction paths are insensitive to the choice of periodic cell. For the *rock-salt*–to–*Wurtzite* transition in CdSe, we demonstrate the method is robust for mechanisms dominated either by atomic motion or by unit-cell deformation; notably, the lowest-energy transition mechanism found by our G-SSNEB changes with cell size from a concerted transformation of the cell coordinates in small cells to a nucleation event in large cells. The method is efficient and can be applied to systems in which the force and stress tensor are calculated using density functional theory.

5.2 Introduction

The nudged elastic band (NEB) method is widely used for calculating reaction pathways of atomic-scale processes in chemical and materials systems [60]. When the initial and final states of a reaction are known, the NEB relaxes an initial pathway to a minimum-energy path (MEP) between reactants and products. With the climbing image NEB, the highest-energy image converges to a transition state (saddle point) along the path. [59] While the end points of the band need to be specified, the reaction coordinate does not. The MEP determined from the NEB can be complex and involve degrees of freedom (DOF) that are not anticipated. [61]

The NEB can be contrasted to a class of drag methods in which a subset of the DOF are preselected as important for the progress of the reaction. Popular progress coordinates include atomic positions, bond lengths, root-mean-squared deviations from a reference structure, or energy coordinates. The system is constrained along the progress variables and allowed to relax in the other DOF, which are considered to be unimportant for describing the reaction mechanism. The system is then dragged along the variables assumed to be important with the hope that the system will be constrained to a good transition state at some position along the path.

The distinction between the NEB and a drag method is illustrated in Fig. 5.1. For a London-Eyring-Polanyi-Sato potential coupled to a harmonic oscillator [62], an assumed reaction coordinate fails to constrain the system to the transition state. The x coordinate clearly separates the initial and final

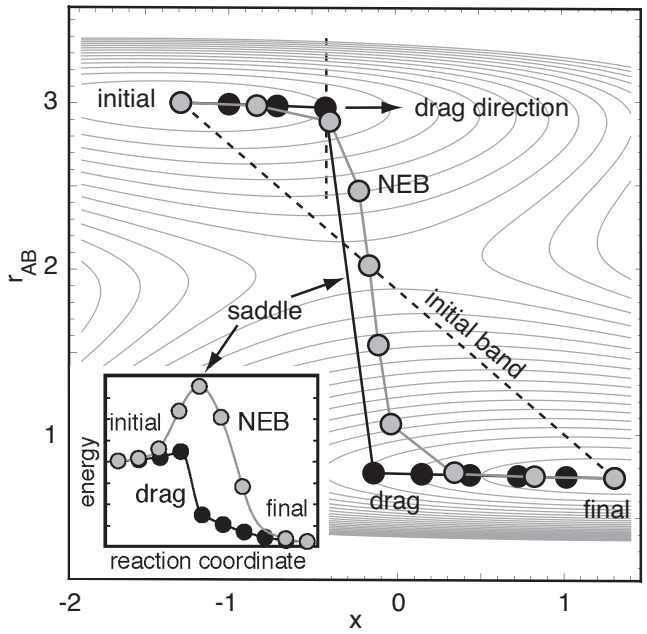

Figure 5.1: In a drag calculation (black) x is chosen as the drag direction so that images along the path are constrained in x and minimized in y. The drag calculation misses the saddle point because the reaction coordinate near the saddle is along the r_{AB} direction and orthogonal to the drag direction. A converged NEB (grey) finds the minimum energy pathway because the reaction coordinate is defined by the images and not by a preconceived notion about which DOF are important.

states, but is not parallel to the negative curvature mode at the saddle point. Using the drag method with x as the progress variable leads to a reaction path which avoids the transition state; that is, the drag path misses the saddle point. The energy profile calculated along the path (Fig. 5.1, inset) underestimates the true barrier. In general, such drag paths can either over- or under-estimate the barrier. The NEB, on the other hand, converges to the MEP, which follows x near the minima and r_{AB} at the saddle.

Here, we address the challenge of finding reaction pathways for solid-solid transformations. The primary computational issue is that there are two types of variables, i.e., those describing atomic motion and those describing the geometry of the periodic cell. It is tempting to focus on either the atoms or the lattice as important and minimize the other, as in the drag method. Trinkle *et al.* showed how a NEB calculation in the atomic DOF can be coupled to a relaxation of the lattice in order to find solid-solid transitions in titanium [63, 64]. In the other extreme, Caspersen and Carter utilized the NEB exclusively for lattice DOF while maintaining the atoms in relaxed geometries – the rapid-nuclear-motion (RNM) approximation [65]. While these approaches can be appropriate for mechanisms primarily involving atomic or primarily lattice changes, they are drag methods. Furthermore, Lui and Johnson showed for pressure-induced *bcc*-to-*hcp* transitions in iron, such drag methods (as applied, e.g., in Ref. [66]) yield an incorrect (and unphysical) MEP as atomic and cell DOF are not properly coupled [67].

In this manuscript, we describe a formulation of the NEB in which

the atomic and lattice variables are treated on equal footing so that reactions involving changes in all DOF are properly described, permitting one to address transformations that transcend current capabilities. Critically, the relative weight assigned to the two sets of variables is chosen so that the resulting MEPs are independent of the unit cell (shape and size) used to describe the transition. This new NEB formulation is largely an integration of the standard NEB in atomic DOF with a similar approach for determining solid-solid transitions (e.g., from Caspersen and Carter [65]), but the formulation ensures that DOF are properly coupled and MEPs are independent of simulation cell. While there are differences in the details of how the lattice variables are described, we keep a similar name for the unified method, i.e., a generalized solid-state nudged elastic band (G-SSNEB).

5.3 Generalized NEB Algorithm

The reaction path is represented in the NEB by a set of images. The NEB force (see Fig. 5.2) on image i is

$$\mathbf{F}_i^{\mathrm{NEB}} = \mathbf{F}_i^{s\parallel} + \mathbf{F}_i^{\nabla\perp}, \tag{5.1}$$

where $\mathbf{F}_i^{\nabla\perp}$ is the force due to the gradient of the potential perpendicular to the path, and $\mathbf{F}_i^{s\parallel}$ is the spring force parallel to the path. $\mathbf{F}_i^{\nabla\perp}$ is calculated from the potential force, $\mathbf{F}_i^{\nabla}$, as

$$\mathbf{F}_i^{\nabla\perp} = \mathbf{F}_i^{\nabla} - (\mathbf{F}_i^{\nabla} \cdot \hat{\boldsymbol{\tau}}_i)\hat{\boldsymbol{\tau}}_i, \tag{5.2}$$

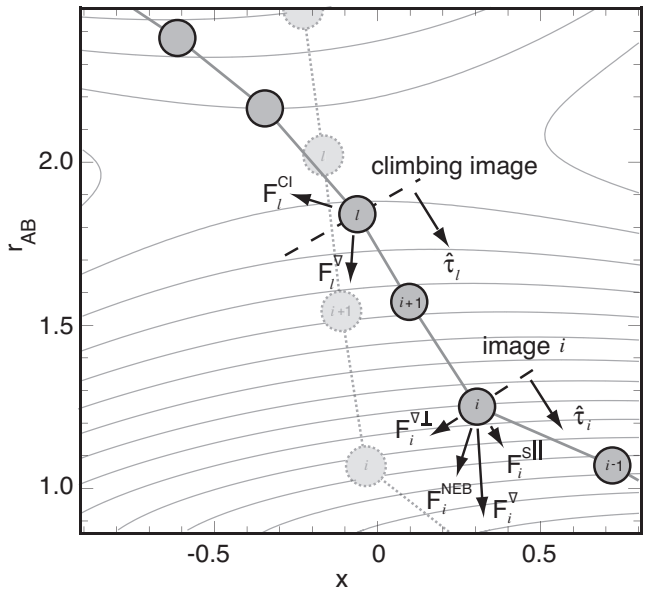

Figure 5.2: The NEB force projections are shown for a typical image i and for the climbing image l. The force components are defined in (5.1)-(5.5). The translucent images are along the converged path where the NEB forces vanish.

where $\hat{\boldsymbol{\tau}}_i$ is an up-winding tangent defined by the adjacent image with the higher potential energy [58].

Spring forces are added to ensure the images are evenly spaced along the transition path,

$$\mathbf{F}_i^{s\parallel} = k(|\Delta\mathbf{R}_+| - |\Delta\mathbf{R}_-|)\hat{\boldsymbol{\tau}}_i, \tag{5.3}$$

where k is the spring constant, the distance to the next and previous images are

$$\begin{aligned} \Delta\mathbf{R}_+ &= \mathbf{R}_{i+1} - \mathbf{R}_i \\ \Delta\mathbf{R}_- &= \mathbf{R}_i - \mathbf{R}_{i-1}, \end{aligned} \tag{5.4}$$

and the vector $\mathbf{R}_i$ has the Cartesian positions of the atoms for image i. The converged path is insensitive to the choice of k, but it should be chosen on the same order as the interatomic force constants for efficient optimization.

The climbing-image NEB method (CI-NEB) is used to find saddle points along a reaction path. The climbing image converges to the saddle point so that no interpolation is required to approximate its energy. The image along the path with the highest potential energy is designated the climbing image l. The force on the climbing image

$$\mathbf{F}_l^{\mathrm{CI}} = \mathbf{F}_l^{\nabla} - 2(\mathbf{F}_l^{\nabla} \cdot \hat{\boldsymbol{\tau}}_l)\hat{\boldsymbol{\tau}}_l, \tag{5.5}$$

is free from spring forces and points up the potential along $\hat{\boldsymbol{\tau}}_l$ and down in all other DOF.

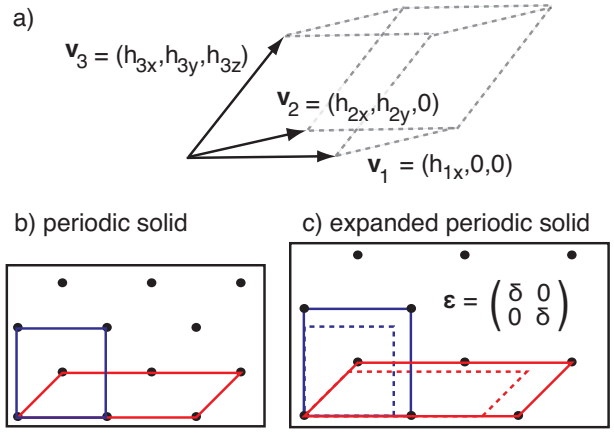

Figure 5.3: (a) Any 3-dimensional unit cell is defined by 3 vectors and 6 DOF. (b) A periodic solid can be represented by different unit cells. (c) The strain in a material is independent of the choice of unit cell. For example, isotropically expanded by an amount δ gives the same strain tensor $\boldsymbol{\varepsilon}$, defined in (5.7), for both the red and blue unit cells.

5.3.1 Stress and Strain

Infinite solids are efficiently modeled with a finite set of atoms in a unit cell replicated by periodic boundary conditions (PBC). Figure 5.3 shows a periodic simulation cell defined by three vectors: $\mathbf{v}_1$, $\mathbf{v}_2$, and $\mathbf{v}_3$. Rotational DOF of the cell are eliminated by constraining $\mathbf{v}_1$ to the x-direction and $\mathbf{v}_2$ to the xy plane. Any cell, $\mathbf{h}$, is then defined by 6 DOF arranged in a lower triangular matrix,

$$\mathbf{h} = \begin{pmatrix} \mathbf{v}_1 \\ \mathbf{v}_2 \\ \mathbf{v}_3 \end{pmatrix} = \begin{pmatrix} \mathrm{h}_{1x} & 0 & 0 \\ \mathrm{h}_{2x} & \mathrm{h}_{2y} & 0 \\ \mathrm{h}_{3x} & \mathrm{h}_{3y} & \mathrm{h}_{3z} \end{pmatrix}, \tag{5.6}$$

where h_{1x} is the component of $\mathbf{v}_1$ in the x-direction and so on. The choice of periodic cell for a given solid is not unique; there are many representations of the same extended solid. It is critical that any description of changes to the

solid lattice – compression, expansion, and shear – be independent of unit cell. A natural choice is the engineering strain, i.e.,

$$\boldsymbol{\varepsilon} = \mathbf{h}^{-1} \cdot (\mathbf{h}^{\text{def}} - \mathbf{h}) \tag{5.7}$$

where $\mathbf{h}^{\text{def}}$ is the cell for the deformed solid. Figure 5.3b shows two periodic representations for a solid and how they deform given a strain (Fig. 5.3c). The strain, $\boldsymbol{\varepsilon}$, for the deformation is the same for both cells.

In the NEB method atomic configurations are moved according to the forces on the atoms. The analogy in solid mechanics is that cell vectors are changed according to the stress in the material. Thus, we need a relation between the stress, the strain, and the corresponding change in cell vectors. A simple system for determining this relationship is an isotropic elastic medium with a Poisson ratio of zero. If the material is strained out of mechanical equilibrium, Hooke's law gives the induced stress

$$\boldsymbol{\varepsilon} = Y^{-1}\boldsymbol{\sigma} \tag{5.8}$$

where Y is Young's modulus and the stress tensor $\boldsymbol{\sigma}$ is the sum of the internal (Cauchy) stress and the external pressure,

$$\boldsymbol{\sigma} = \boldsymbol{\sigma}_{\text{cauchy}} + P\,\mathbf{I}. \tag{5.9}$$

Here, we have assumed a hydrostatic (isotropic) pressure, P, applied uniformly via an identity matrix $\mathbf{I}$. From the stress in a material, we would like to calculate the strain and the change in the unit cell vectors, $\mathbf{h}^{\text{def}}$, which will

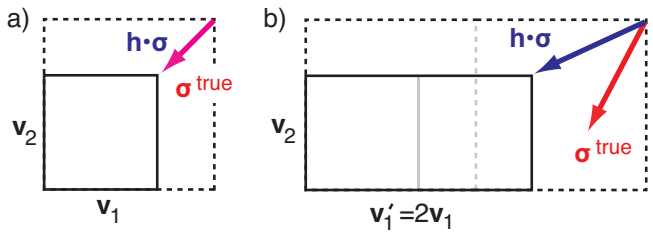

Figure 5.4: (a) A square cell in mechanical equilibrium (black) is uniformly expanded (dashed). The steepest-descent directions calculated from (5.11) and (5.10) give the same direction required to restore equilibrium. (b) When the cell is doubled along $\mathbf{v}_1$, the direction from (5.11) does not restore the solid to equilibrium. The direction from (5.10) does, and results in the same macroscopic change to the cell as in (a).

bring the solid back into mechanical equilibrium. This deformation can be calculated from (5.7) and (5.8)

$$(\mathbf{h}^{\text{def}} - \mathbf{h}) = Y^{-1}(\mathbf{h} \cdot \boldsymbol{\sigma}), \tag{5.10}$$

and the steepest-descent direction to bring the solid into equilibrium is along $\mathbf{h} \cdot \boldsymbol{\sigma}$.

Caspersen and Carter have a different approach to calculating the steepest-descent direction. They determine the change in energy with respect to the components of $\mathbf{h}_{m,n}$, which they call the true stress [65],

$$\boldsymbol{\sigma}^{\text{true}}_{m,n} = -\frac{\partial E}{\partial \mathrm{h}_{m,n}} = -\Omega(\boldsymbol{\sigma} \cdot \mathbf{h}^{-1})^{\mathrm{T}}_{m,n}, \tag{5.11}$$

where E is the potential energy of the cell and m, n are the components of the stress tensor. The problem with this definition is that the strain along the steepest-descent direction is not invariant to the choice of cell. This is illustrated graphically in Fig. 5.4. For a uniformly strained cubic cell, $\boldsymbol{\sigma}^{\text{true}}$ and

$\mathbf{h}\cdot\boldsymbol{\sigma}$ point in the same direction towards the unstrained geometry. If, however, the representative cell is doubled along only one direction, $\boldsymbol{\sigma}^{\text{true}}$ no longer points towards the unstrained geometry, so the approach does not maintain invariance with respect to cell choice, as it should.

5.3.2 Coupling Cell and Atomic Variables

In our G-SSNEB method, the atomic and cell variables are combined into a single vector containing forces and another containing distances. With this unified description we can use the NEB force projections as described in Sec. 5.3. The challenge is that the cell and atomic variables have different units and have different scaling relations with system size. Changes in the cell are described by strain, which is unitless, and changes to atomic position have units of length. Similarly, the corresponding cell variable to the forces on the atoms is the stress on the cell vectors, which has units of pressure. To combine these quantities, a Jacobian J is needed to transform stress and strain into the units of the atomic forces and distances. The Jacobian should also make the cell and atomic variables scale in the same way with system size so that converged minimum energy paths will be invariant to the choice of unit cell.

The vector describing changes in configuration is formed by concatenating the (scaled) strain and changes in atomic coordinates,

$$\Delta\mathbb{R} = \{J\boldsymbol{\varepsilon}, \Delta\mathbf{R}\}. \tag{5.12}$$

The strain is multiplied by J to make the units and system size scaling consistent with the atomic motions. Because $\boldsymbol{\varepsilon}$ is unitless, J must have units of

length. Our choice is the average distance between atoms in the cell

$$L = \left(\frac{\Omega}{N}\right)^{1/3}, \tag{5.13}$$

where $\Omega = \det \mathbf{h}$, i.e., the volume of the unit cell, and N is the number of atoms in the cell.

We also require that the magnitude of $J\boldsymbol{\varepsilon}$ scale in the same way as the magnitude of $\Delta\mathbf{R}$ for different unit cell sizes. Consider a unit cell with a single atom that moves by an amount $\Delta\mathbf{R}_0$. If we take a larger cell with N atoms, the magnitude of atomic motion becomes

$$\Delta\mathbf{R}_N = \left(\sum_{i=1}^{N} \Delta\mathbf{R}_i^2\right)^{1/2} = \sqrt{N}\Delta\mathbf{R}_0. \tag{5.14}$$

The strain, however, is invariant to the system size. Thus, we need a factor of $\sqrt{N}$ in our Jacobian, i.e.,

$$J = L\sqrt{N} = \left(\frac{\Omega}{N}\right)^{1/3} N^{1/2} = \Omega^{1/3} N^{1/6}\ . \tag{5.15}$$

The stress is scaled to the atomic forces using similar arguments. A given stress, $\boldsymbol{\sigma}$, describes the force per unit area on the cell. With the average distance between atoms defined as L, the average force per atom is $\boldsymbol{\sigma}L^2$. As with the distance, the stress needs to be multiplied by a factor $\sqrt{N}$ to scale in the same way as the forces with system size. The resulting G-SSNEB force,

$$\mathbb{F} = (-\Omega\boldsymbol{\sigma}/\mathrm{J}, \mathbf{F}). \tag{5.16}$$

is formed by concatenating the (scaled) stress and the atomic forces.

5.3.3 Method Details

In the G-SSNEB method it is important to decouple motion of atomic DOF from motion of the cell when calculating $\Delta\mathbb{R}_+$, $\Delta\mathbb{R}_-$ and the tangent direction from (5.3) and (5.12). When $\Delta\mathbf{R}$ is calculated in Cartesian coordinates, as in the NEB, a change in the cell coordinates will contribute to atomic motion since the atoms are represented within the periodic cell. To decouple the variables, $\Delta\mathbf{R}$ should be calculated in direct coordinates, where atomic positions are given as fractional distances along $\mathbf{v}_1$, $\mathbf{v}_2$, and $\mathbf{v}_3$. The difference vectors are then converted back to Cartesian coordinates to apply the force projections.

The vector $\Delta\mathbf{R}$ is calculated between two configurations that may have different cell geometries. To convert between direct and Cartesian coordinates, we use the average cell geometry. More specifically, $\mathbf{R}_i$ and $\mathbf{R}_{i+1}$ are first put into direct coordinates using their respective cells, $\mathbf{h}_i$ and $\mathbf{h}_{i+1}$. $\Delta\mathbf{R}_+^{\text{direct}}$ is then calculated by subtraction, and the resultant vector is converted back to Cartesian using the average cell

$$\bar{\mathbf{h}}_+ = \frac{1}{2}(\mathbf{h}_i + \mathbf{h}_{i+1}). \tag{5.17}$$

This method for calculating distances is consistent with the regular NEB when there is no change in the cell DOF.

The strain between two images, which is the fractional change in the cell parameters, is also sensitive to which image is used for reference. In the G-SSNEB, the vector between image i and $i+1$ should be the negative of that

from $i+1$ to i. Directly using (5.7) we find

$$\mathbf{h}_i^{-1} \cdot (\mathbf{h}_{i+1} - \mathbf{h}_i) \neq -\mathbf{h}_{i+1}^{-1} \cdot (\mathbf{h}_i - \mathbf{h}_{i+1}). \tag{5.18}$$

To ensure a consistent strain between images we use the average,

$$\bar{\boldsymbol{\varepsilon}}_+ = \frac{1}{2}(\mathbf{h}_{i+1}^{-1} + \mathbf{h}_i^{-1}) \cdot (\mathbf{h}_{i+1} - \mathbf{h}_i). \tag{5.19}$$

Using a similar philosophy, we want the Jacobian J to remain constant during the simulation. Thus, in (5.13) and (5.15), we use the average cell volume

$$\bar{\Omega} = \frac{1}{2}(\Omega_{\text{inital}} + \Omega_{\text{final}}) \tag{5.20}$$

between the initial and final states.

5.4 Application

5.4.1 CdSe Solid-Solid Transformation

The G-SSNEB is numerically demonstrated for a solid-solid phase transition in CdSe. To illustrate the importance of including both cell and atomic DOF in the reaction coordinate, we show two paths by which CdSe can transition from rock-salt to Wurtzite (Fig. 5.5). Transition path (a) is dominated by atomic DOF; each row of atoms slides with respect to the adjacent row. Path (b) is dominated by cell DOF; the atoms do not move significantly with respect to the cell vectors.

Initially, interatomic forces are evaluated with an empirical potential defined by Rabani [68]. In a later section, these calculations are repeated using

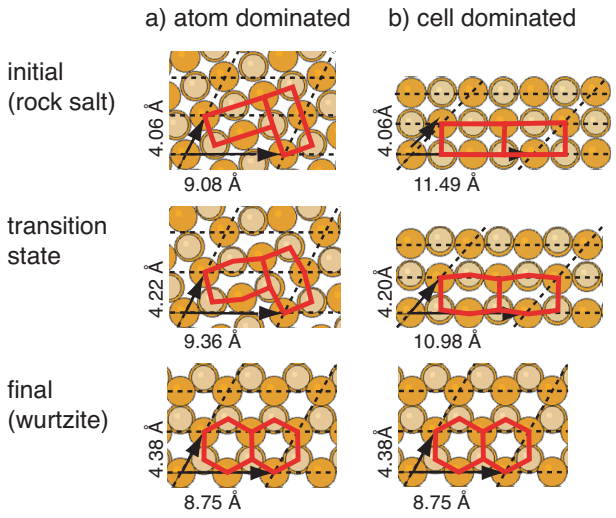

Figure 5.5: *Rock-salt*–to–*Wurtzite* transformation in CdSe can occur via an atom-dominated (a) and cell-dominated (b) mechanism. Cd atoms are lighter and Se darker.

density functional theory (DFT). The empirical potential has two terms; a Lennard-Jones term with a cutoff of 10 Å and a Coulomb term which is evaluated by Ewald summation using a real-space radius of 10 Å. Forces and stresses are evaluated using the LAMMPS program [69].

Figure 5.6 shows the energy along three paths connecting the initial and final states for the atom-dominated mechanism. The reaction coordinate primarily involves atomic DOF so the regular NEB is able to find the saddle point. The MEP along this path is not smooth, however, and a discontinuity is seen in the path between images 7 and 8 as the cell DOF suddenly relax to give a state which is similar to the final state. In the other extreme, the RNM approximation has only cell DOF in the reaction coordinate. Because the process is atom-dominated, the saddle point is not found using this approxi-

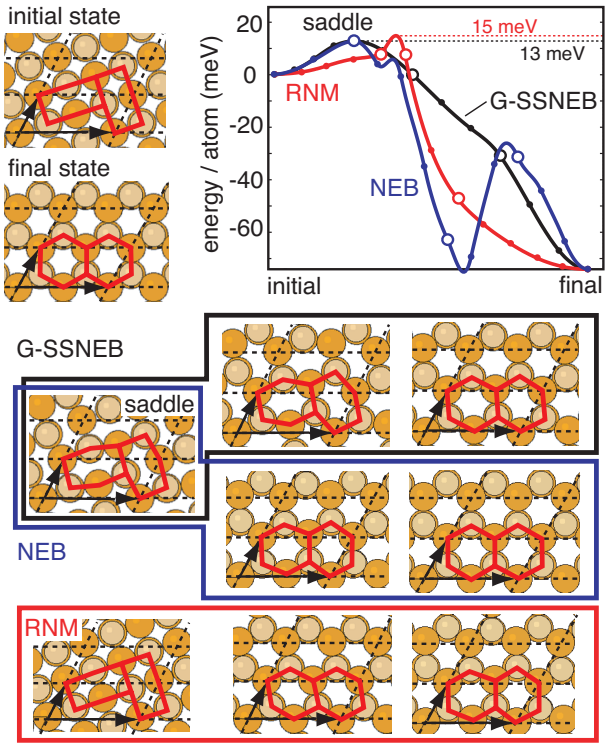

Figure 5.6: Comparison of the three algorithms used to determine the CdSe *Rock-salt*–to–*Wurtzite* transformation along the atom-dominated path (Fig. 5.5a). The G-SSNEB finds the saddle point. The NEB, for which the cell DOF are always relaxed, is also able to find the saddle but the path is not smooth because the cell DOF do not change continuously. The RNM path, for which the atoms are always relaxed, fails to determine the saddle. Selected configurations along each path (marked with larger open circles) are shown.

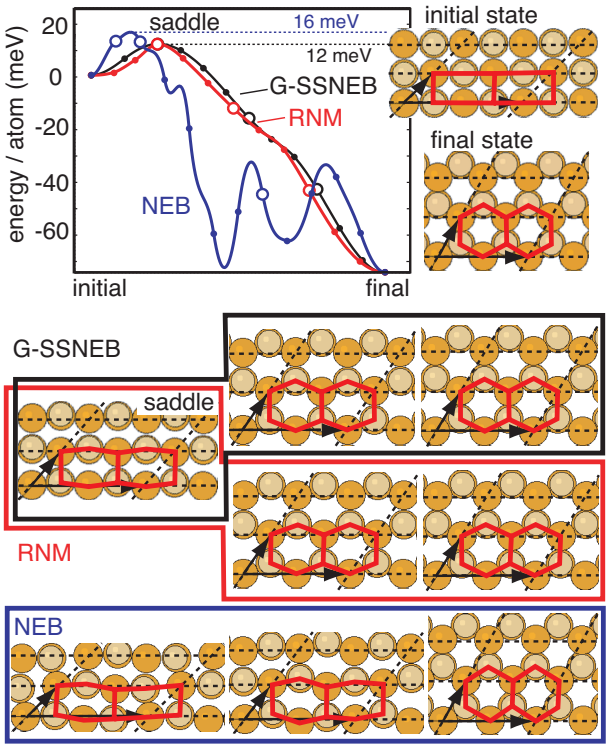

Figure 5.7: Similar calculations as in Fig. 5.6 for the cell-dominated path (Fig. 5.5b). In this case the RNM approximation finds the saddle but the regular NEB, for which the cell coordinates are minimized, does not.

mation. There is also a discontinuity in the RNM path between the highlighted images 4 and 5, at which point the atoms suddenly relax from the rock-salt to Wurtzite structure. The G-SSNEB treats the atomic and cell DOF on equal footing and finds a true reaction coordinate.

Figure 5.7 shows the energy along three paths for the cell-dominated mechanism (Fig. 5.5b). Here, the RNM approximation successfully finds the same saddle point as the G-SSNEB. The regular NEB results in a wandering path which does not pass through the saddle. Images 1 and 2, which bracket

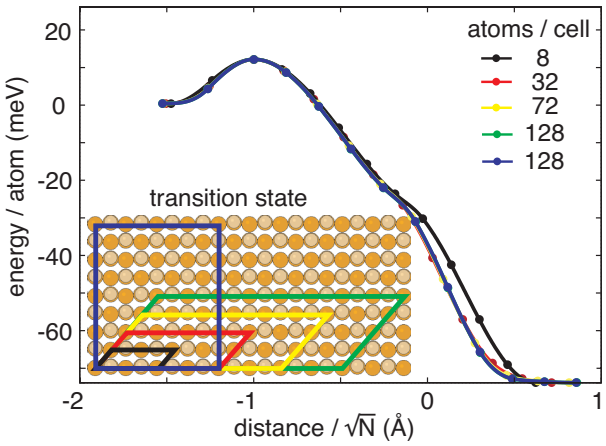

Figure 5.8: When the unit cell is large enough to accommodate the transition mechanism, G-SSNEB paths are invariant to cell size and shape.

the saddle, have a discontinuous change in cell geometry.

5.4.2 Invariance of converged paths to cell geometry

Strain was chosen to represent cell changes in Sec. 5.3.1 because it is a material property that is independent of the unit cell chosen to represent the solid. In Sec. 5.3.2 a $\sqrt{N}$ scaling factor was included in the Jacobian to ensure that the magnitude of cell DOF changes would scale with the same power of N as the atomic motion within the cell. Figure 5.8 shows the invariance of converged G-SSNEB paths (Fig. 5.5b) to the cell size and shape. The eight-atom cell is a little too small to accommodate the periodicity of the fully relaxed MEP. The MEP for larger cells are indistinguishable.

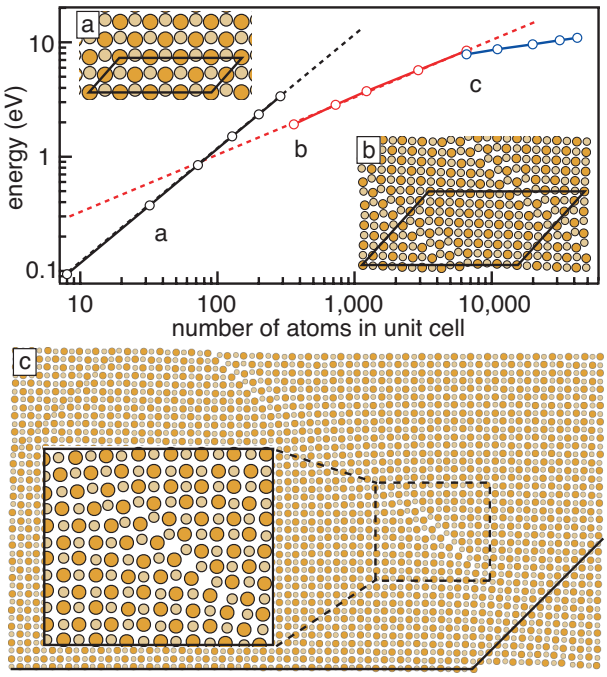

Figure 5.9: Scaling of the energy barrier with system size for different reaction mechanisms. For small systems, a concerted bulk mechanism is preferred (a). For larger system, there is a crossover to a mechanism in which the crystal slips along a line (b) and finally to a local nucleation mechanism (c).

5.4.3 Crossover to a localized mechanism

Small cells with few atoms provide a computationally efficient representation for calculating solid-solid phase transformations. Changes in the cell DOF correspond to a collective motion of the atoms in the solid. The energy barrier calculated for a transformation involving cell motion will increase as more atoms are included in the unit cell (the energy barrier per atom becomes constant). There will therefore always be some cell size for which it will be energetically favorable to have a local nucleation event of one phase in the other and a subsequent propagation of the interface across the cell.

The energy barrier for the cell-dominated transformations in CdSe is shown as a function of cell size in Fig. 5.9. The line through the origin corresponds to the scaling of the barrier for the concerted process (Fig. 5.5b). The energy barrier scales linearly with the number of atoms, giving a unit slope on the log plot. With increasing unit cell size, a lower saddle is found where the concerted motion is only in one dimension. The energy barrier scales with the length of the line defect so that increasing the cell size in two dimensions results in a slope of 1/2. For a local transition state, the energy barrier will not increase with the number of atoms in the cell in the limit of a large cell. In the largest cells considered (Fig. 5.9c) a local mechanism (in two-dimensions) is becoming apparent. As the cell is expanded in the xy-plane, the energy for this local mechanism is expected to plateau. Increasing the cell size in the z direction as well should lead to a local nucleation event in all three dimensions. It should be noted, however, that the barrier for such an event will be large,

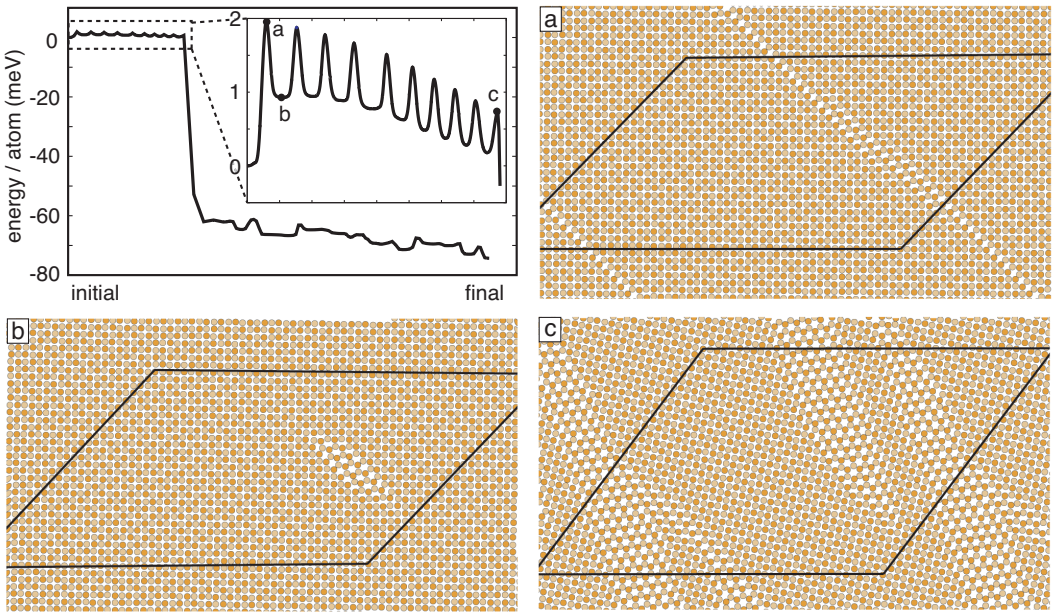

Figure 5.10: Energy landscape of a *rock-salt*–to–*Wurtzite* transformation in a 2912 atom unit-cell. The highest transition state (a) is a line defect followed which forms (b) a local Wurtzite domain in a rock-salt structure. The nucleation volume continues to grow until transition state (c) where Wurtzite domains dominate the cell structure.

and it is likely that defects would play a role in such a transition in a real CdSe crystal.

In general, there can be many pathways connecting a given initial and final state for a solid-solid phase transformation. An example of this complexity is shown in Fig. 5.10. The transformation is initiated with a line defect which slips into a local minimum where a Wurtzite domain is nucleated (Fig. 5.10b). This process repeats ten times as the Wurtzite domain grows. Finally, there is a significant change in the cell DOF and the crystal switches to the Wurtzite structure. The G-SSNEB must then follow a minimum energy path to bring

each atom to its specified location in the product structure. Clearly this can happen in many ways. Because of this degeneracy, a barrier found by the G-SSNEB should be considered an upper bound in large systems.

5.4.4 CdSe solid-solid transition using DFT

The cost of the G-SSNEB method is similar to the regular NEB so that it can be used for systems described by DFT. The method has been implemented both for the atomic simulation environment (ASE) [70] in the TSASE code [71] and for the Vienna *ab initio* simulation package (VASP) in the VTST code [72]. Here we consider the same transition in CdSe from the previous sections using forces and stresses evaluated with the VASP code. The DFT calculations were done using a plane-wave basis set up to an energy cutoff of 455 eV. Core electrons were treated within the projector augmented wave framework [15]. Electron exchange and correlation were modeled within the generalized gradient approximation using the PW91 functional [32]. The simulation cell was chosen to contain 8 atoms using a Monkhorst-Pack mesh of $10\times10\times10$ to sample the Brillouin zone [73]. Tests with 32 atoms per unit cell showed that the results were converged with respect to cell size.

Figure 5.11 shows G-SSNEB calculations of both the atom- and cell-dominated mechanisms (see Fig. 5.5). The atom-dominated path (black) follows a similar path to what is found using the empirical potential, although the barrier is reduced by a factor of 5. Perhaps even more significantly, no concerted cell-dominated mechanism is found. In this regard, DFT provides

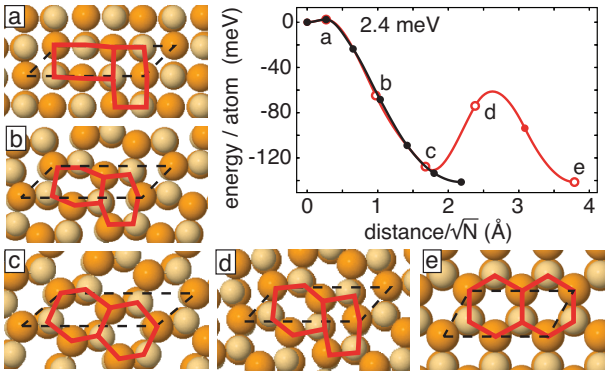

Figure 5.11: Energy landscape of the *rock-salt*-to-*Wurtzite* transformation within DFT. The atom-dominated mechanism (black) is similar to that found previously. The cell-dominated path (red) is different; it first follows the atom-dominated mechanism (a-c) and then has second transformation involving rotation of the atoms (c-e) to reach the specified cell in the final state.

a qualitatively different energy landscape for the transformation. Instead of finding a concerted mechanism, the path to the cell-dominated final state (red) follows the atom-dominated mechanism and then an atomic rotation to reach the specified final state.

5.5 Discussion

The Jacobian in (5.15) is used to combine atomic and cell DOF so that the MEP found by the G-SSNEB is insensitive to the choice of unit cell size and geometry. The choice, however, is not unique. Multiplying the Jacobian by a constant factor, for example, will change the relative weighting between atomic and cell motion along the MEP. In some cases, the user may have to adjust this parameter to equalize atomic and cell motion for their particular

reaction path. While the choice of Jacobian influences the MEP (much in the same way that mass-weighted coordinates do), the stationary points are not affected. This is particularly relevant when using a climbing-image; if the climbing image converges to a saddle, the barrier height is independent of the Jacobian. For example, in our calculations, the regular climbing image NEB is able to converge to the saddle for the atom-dominated CdSe phase transition (Fig. 5.6) because 90% of the G-SSNEB tangent at the saddle can be projected onto the atomic DOF. Similarly the RNM approximation is able to converge to the cell-dominated process (Fig. 5.7) because 68% of the G-SSNEB tangent is along cell DOF. While the reaction coordinates are not entirely along atom and cell coordinates, respectively, the climbing image is robust enough to find the saddle points using these approximate methods.

There is an unusual consequence of introducing cell DOF into the NEB. The cell is used to describe the periodicity of an infinite solid, but the configuration of any real, finite system is fully described (at least classically) by the coordinates of the constituent atoms. In this sense, the cell DOF are artificial constructs for an infinite solid. In the RNM approximation, changes in the cell are viewed as slower than atomic motion so that the atoms can always be relaxed. This could be, in some limited cases, an appropriate view for an experiment in which macroscopic variables, such as the external pressure or the stress on the solid, are used to induce a solid-solid phase transition. For a thermally-activated process, however, atomic motion should initiate the transition. The barrier for any concerted mechanism will increase with the

number of atoms so that in the limit of a continuum solid, no such transition is thermally accessible. Instead, there must be a lower energy local process that is dominated by atomic motion. For these transitions, the standard NEB should be sufficient to describe it.

However, for any finite-cell description, the atomic and cell DOF are coupled and must be handled such that no one set of the DOF dominate so as to find the correct transition state and the results are independent of the choice of simulation cell, as we have now made possible.

5.6 Conclusion

We have developed a generalization to the solid-state NEB methods (i.e., G-SSNEB method) in which atomic and cell DOF are considered equally for the reaction coordinate, and results do not inherently depend on the simulation cell. We demonstrated that the method is robust for transitions dominated by atomic motion and for processes where deformation of the simulation cell dominants. We illustrate that the mechanism found by the G-SSNEB can change with cell size from a concerted transformation of the cell coordinates to nucleation involving atomic coordinates. In addition, the method was exemplified both by empirical and DFT methods for system that exhibits both atom-dominated and cell-dominated transitions.

5.7 Acknowledgments

The work in Austin was supported by the National Science Foundation (CHE-0645497) and the Robert A. Welch Foundation (F-1601). GH was supported by the W. A. "Tex" Moncrief, Jr. Endowment in Simulation-Based Engineering Sciences through Grand Challenge Faculty Fellowships from the Institute of Computational and Engineering Sciences at The University of Texas at Austin. DDJ is supported by the Department of Energy, Basic Energy Sciences, Division of Materials Science and Engineering (DEFG02-03ER46026) and the Ames Laboratory (DE-AC02-07CH11358), which is operated by Iowa State University. WC was supported for his senior project with DDJ at the University of Illinois by the National Science Foundation (DMR-07-05089) for the initial stages of this work. Computing was provided by the Texas Advanced Computing Center. We also thank Kyle Caspersen and Emily Carter for insightful comments. Computing time was provided by the Texas Advanced Computing Center. We would also like to thank Kyle Caspersen and Emily Carter for insightful comments.

Chapter 6

From Graphite to Diamond: Reaction Pathways of the Phase Transition

6.1 Abstract

Phase transitions between carbon allotropes are calculated using the generalized solid-state nudged elastic band method. We find new reaction mechanisms between graphite and diamond that have nucleation characteristics and lower activation energies than concerted mechanisms. The barrier from graphite to hexagonal diamond is lower than to cubic diamond, resolving a conflict between theory and experiment. Transitions are calculated to three structures of cold compressed graphite: M-carbon, Z-carbon and bct C4, which are accessible at the experimentally relevant pressures near 17 GPa.

6.2 Introduction

Carbon has many crystalline phases, including graphite, cubic diamond (CD), hexagonal diamond (HD) and cold compressed graphite (CCG). The transition mechanisms between these phases are not thoroughly understood. There is no consensus, for example, of the structure of CCG [74, 75, 76]. The transitions from graphite to CD and to HD have been well documented

in experiments. It has been found that both transitions can occur at 15 GPa static pressure and the temperature required to form HD is lower than CD [77, 78], indicating that the barrier to form HD is lower at this pressure.

Challenges still exist in the theoretical explanation of these two-phase transitions. Molecular dynamics studies are limited by the vibrational time scale of atoms, and so are often done at pressures several times higher than in experiments in order to observe a transition. The transition mechanism, however, can change with increasing pressure [79]. Another approach is to use transition state theory to calculate the barrier and mechanism for the activated process. Previous saddle point calculations have focused on the concerted mechanism, where the barrier to HD is higher than to CD, in disagreement with experiments [80, 81]. The concerted mechanism can be active at pressures higher than 15 GPa or under shock wave compression [82, 83], but at 15 GPa static pressure there must be a lower energy pathway. Employing a neural network potential and including 145,000 atoms, Khaliullin et al. found the structure of a stable nucleus, but not a reaction pathway of its formation [84]. In this simulation, the lowest pressure required to stabilize a diamond nucleus in graphite was 30 GPa, twice the experimental pressure. CCG can also be synthesized at low pressure (17 GPa) and at lower temperatures than is required to form diamond, indicating that a different mechanism with a lower barrier is present [76]. To resolve these issues, we use a computational method that can reveal the mechanism of solid-solid phase transitions between carbon phases in the low-pressure regime.

In this communication, we present a new transition mechanism at low pressure that was found using the generalized solid-state nudged elastic band (G-SSNEB) method. Forces and energies were calculated with density functional theory (DFT) using a simulation cell containing only 40 atoms. The rate-limiting step in this mechanism corresponds to the nucleation of several diamond layers in the graphite structure. The diamond phase then grows, layer by layer, overcoming a series of smaller barriers. Our result shows that the highest barrier to HD is lower than to CD at 15 GPa. The barriers to form previously proposed structures of CCG are compared, and found to be lower than to CD though still higher than to HD, pointing to a selection criterion for identifying the structure of CCG.

6.3 Method

Minimum energy paths (MEPs) were calculated using the climbing-image G-SSNEB method [85]. This nascent method is appropriate for solid-solid phase transitions that are described by changes in both atomic coordinates and lattice vectors. Neglecting to include either of these degrees of freedom in the reaction coordinate (e.g. by minimizing them along a reaction path) leads to a bias in the calculation and a risk of missing the correct MEP [85]. An adaptive nudged elastic band approach was used to increase the resolution near saddle points [86].

Hexagonal graphite (HG) was chosen as the initial state in the formation of HD, and rhombohedral graphite (RG) for CD, based upon symmetry

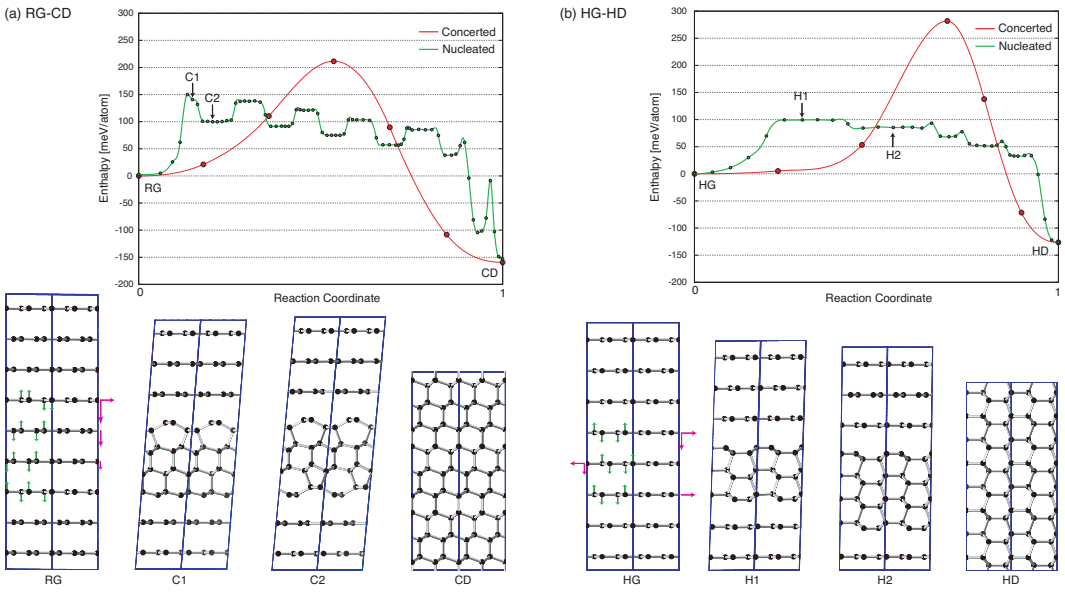

Figure 6.1: Enthalpy landscapes and nucleation structures of (a) RG-CD and (b) HG-HD phase transitions at 15 GPa. Arrows on the initial structures indicate the relative movement of atoms. Two unit cells are shown for each structure. The undulations in the minimum energy paths for the nucleation mechanisms correspond to layer-by-layer growth of the diamond phase.

considerations [84]. Supercells of 1×1×4 unit cells were used for the HG-HD transition and 2×1×3 for RG-CD, so that both transitions were represented by four carbon atoms per layer and a similar number of layers (8 for HG and 9 for RG).

Energies and forces between the carbon atoms were calculated with DFT using a plane wave basis set for valence electrons and the projector augmented wave method for core electrons, as implemented in the Vienna ab-initio simulation package [15]. The electron exchange-correlation energy was calculated in the generalized gradient approximation (GGA) with the Perdew-

Wang (PW91) functional [32]. Two levels of convergence were used, a lower level with the standard carbon pseudopotential and a plane wave energy cutoff of 520 eV, and then a higher level to converge the enthalpy barriers using hard pseudopotentials and a cutoff energy of 910 eV. A semi-empirical dispersion term was added to describe van der Waals interactions [87].

6.4 Results

Figure 6.1 shows the enthalpy landscapes of transitions from RG to CD and from HG to HD at 15 GPa. The nucleation mechanisms (green lines) have lower barriers than the concerted mechanisms (red lines). Furthermore, in the nucleation mechanism, the overall barrier to form CD is higher than HD. The common feature of the nucleation mechanisms in Fig. 6.1 is that there are a series of barriers and minima along the path, and the initial barrier is higher than the following ones. This landscape is characteristic of a nucleation process followed by growth of the nucleus. Unlike the concerted mechanism, where all the atoms in the supercell transform to the new phase simultaneously, the nucleation mechanism involves the transformation of several layers into a two-dimensional diamond nucleus that subsequently grows layer-by-layer into the graphite. We note, however, that the nucleation and growth occurs along one dimension; the transition is still concerted within each layer. The lateral interface, which must also contribute to the energy of a truly local nucleus, are not considered in our small simulation cells. The nucleation mechanism found here may be observable in the case of a small graphite particle where

the nucleus is able to extend across the particle so that the lateral interfaces are eliminated. Despite not providing true nucleation barriers, our calculations can be used to compare barriers to different phases when the lateral sizes of the nuclei are comparable. We note that the barriers of the nucleation mechanisms are largely determined by the enthalpy to form the nuclei, C1 and H1.

For the RG to CD transition, the nucleus is a mixed CD and M-carbon phase (or W-carbon, as one cannot distinguish from one layer). In each basin along the minimum enthalpy landscape, both ends of the nucleus are capped with M-carbon; on the plateaus, one side is M-carbon and the other is a CD/RG interface. The difference in termination means that the M/RG interface has lower energy than the CD/RG interface, although the CD/RG interface is unavoidable as the CD phase grows. There is no such mixed interface for the HG to HD transition so the HD/HG interface is more stable. While the enthalpy of HD is slightly higher than CD, the energy of the HD/HG interface is much lower than that of CD/RG and the overall nucleation barrier is also lower.

Due to our limited supercell size, the nuclei have periodic structure in the graphite planes and the interface between phases is only present between layers. As the nucleus grows, the interface size and structure does not change. The enthalpy change along the reaction path is only due to differences in enthalpy of the graphite and diamond phases. When the pressure is sufficiently high so that the diamond phase is more stable than graphite, the enthalpy profile is exothermic after the nucleus forms.

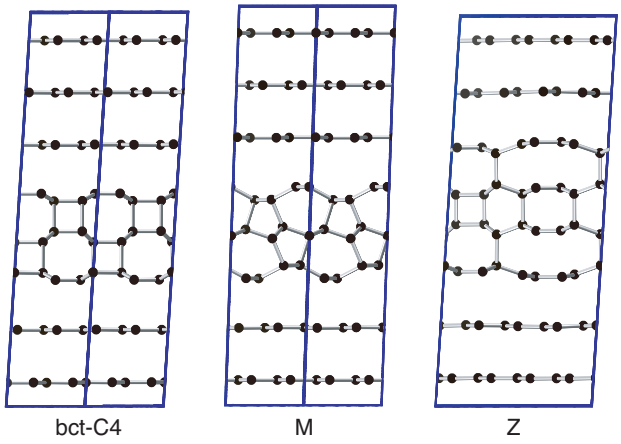

Figure 6.2: The smallest nuclei of bct C4, M, and Z-carbon. Two unit cells are shown for bct C4 and M-carbon; one unit cell is shown for Z-carbon.

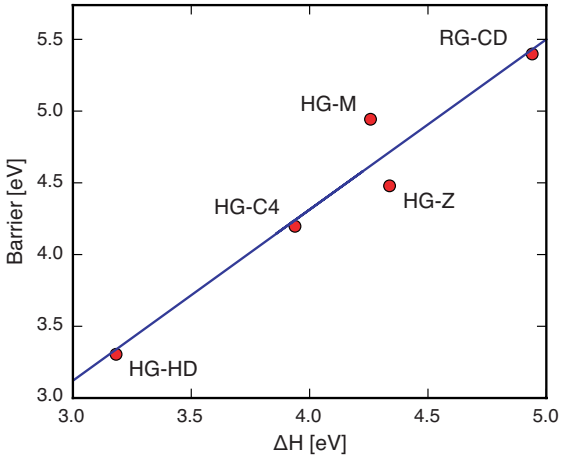

Figure 6.3: Brønsted-Evans-Polanyi relationship for nuclei formation at 15 GPa.

Since the highest barrier along each MEP is due to the formation of the smallest nucleus, only this barrier is calculated when considering transformations from graphite to CCG. Initial structures of the CCG nuclei were generated based upon those found for CD and HD. Each was taken as a final state of a G-SSNEB calculation. If an intermediate state was found by the G-SSNEB, it was set as the final state and the calculation was restarted. This procedure was repeated until no intermediate state was found, so that the stable nucleus was directly connected to the initial state by a single barrier.

Bct C4, M, and Z-carbon are calculated as candidates of the kinetically accessible CCG phase [88, 89, 90, 91]. The configurations of the CCG nuclei at 15 GPa are shown in Fig. 6.2. The structure of the Z-carbon nucleus is only slightly distorted from bulk. Two C atoms above and below the octagon in the center are displaced away from the 4-carbon ring positions, so the 6+4+6 rings merge into large 12-carbon rings. Interestingly, the distortion does not occur in bct C4, where no 6-carbon rings exist. A Brønsted-Evans-Polanyi (BEP) relationship, showing a linear trend between the barrier and enthalpy of forming the smallest nucleus, is given in Fig. 6.3. To further save computational effort, we use the enthalpies of the critical nuclei and the BEP relationship to determine the overall phase transition barriers.

The phase transition barriers are shown as a function of pressure in Fig. 6.4. The barriers are only plotted at pressures where the new phases are more stable than graphite. The three forms of CCG become stable above 15-25 GPa, consistent with experiment and recent calculations also using GGA

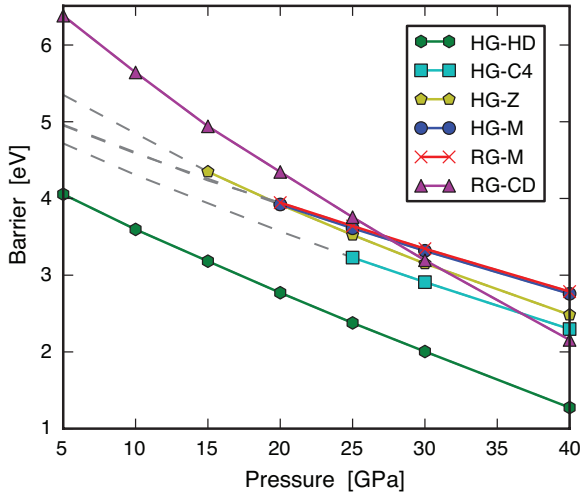

Figure 6.4: Pressure dependence of the maximum barrier for each phase transition. Dashed lines indicate regions where the new phases are less stable than graphite.

functionals with long range dispersion [92]. Earlier LDA calculations underestimate the enthalpy differences between graphite and CCG [81, 91].

The barriers from RG and HG to the M-phase of CCG are the same because RG and HG differ only in their long-range stacking of layers, which does not effect the formation energy of the critical nucleus. The barrier to Z and M-carbon are similar, although Z-carbon has a somewhat more negative activation volume (the slope in Fig. 6.4), so the transition to Z becomes favorable as compared to M above 20 GPa. An interesting and important result is that enthalpy changes to the final phases are not proportional to the barriers to reach them. It is the formation energy of the critical nucleus that determines the activation energy. For example, bct C4 has higher enthalpy than M-carbon [92], but the barrier is lower due to a lower energy interface with

graphite. In the formation of metastable forms of carbon, the kinetics can be more important than the thermodynamics.

Figure 6.4 shows that the formation of CCG is favorable as compared to CD below pressures of 27 GPa. This is only true for the nucleation mechanism found here; CD is favored via the concerted mechanism [81, 93]. Our ordering of barrier heights is consistent with the experimental observation that CCG can be synthesized at a lower temperature than CD near 17 GPa. On the other hand, our calculations also show that HD should form more readily than CCG at this pressure, which is not observed. One possible resolution is that the kinetically accessible phase of CCG has not been found yet; new forms are still being discovered [94]. Our model also has some limitations: the lateral interfaces of the critical nuclei are not included, nor defects, which may play a role in the nucleation process.

6.5 Discussion

While not all issues are resolved, our calculations show that the kinetics of the nucleation mechanisms are qualitatively different from the concerted mechanisms. The nucleation mechanisms are understood in terms of the structure and energy of the critical nuclei. The nucleation barriers are described by two components; one from the interface energy between the phases, and the other from the enthalpy of the new phase. The enthalpy of the new phase cannot alone determine the magnitude of the barrier. Its contribution is proportional to the volume of the critical nucleus, which can vary significantly, as

shown in Fig. 6.1. For small nuclei, the barrier is dominated by the interface energy, which is positive with respect to graphite. As the nucleus grows, the barrier is dominated by the enthalpy of the new phase, which is negative with respect to graphite. In our model, any comparison of enthalpies away from the critical nucleus is ambiguous; it is at the critical radius where the enthalpies should be compared. This size of the critical nucleus is a function of pressure. In Ref. [84], for example, the energy of nuclei of new phases in graphite are calculated, but the size of the nuclei are chosen arbitrarily and there is no guarantee that these will be close to the critical size.

Under increasingly high pressure conditions, the concerted mechanism will be faster than nucleation. To compare these two mechanisms, we can write the enthalpy barriers as $\Delta E + P\Delta V$, where ΔE is the energy barrier, ΔV is the activation volume, and P is the pressure. For any phase transition from graphite, ΔV is negative in both mechanisms, as can be seen from the slopes in Fig. 6.4. In a system with a large number of atoms, the volume at the saddle point for the concerted mechanism is smaller than a nucleation mechanism. At increasing pressure, the $P\Delta V$ term will dominate the enthalpy barrier and the concerted mechanism, with a more negative ΔV, will eventually be spontaneous.

It will be interesting to investigate the size at which the reactions favor a truly local nucleation mechanism, as was done with the G-SSNEB method for CdSe [85]. In a large graphite simulation at pressures between 15 and 27 GPa, the critical nucleus must be limited in lateral extent, and it may

involve more graphite layers. Our current calculations correspond to the limit of layer-by-layer propagation of the new phase in graphite.

6.6 Conclusion

In conclusion, we are able to calculate new nucleation mechanisms with a modest number of atoms over a wide pressure range using the G-SSNEB method. The barrier from graphite to three candidate CCG structures, bct C4, M, and Z-carbon, are calculated to be lower than to CD in the pressure range at which they are synthesized in experiment. The barriers to HD and to CD are in the same order as seen in experiments, demonstrating the usefulness of the G-SSNEB method in exploring solid-state potential energy surfaces.

6.7 Acknowledgments

This work was supported by the National Science Foundation under CHE-1152342. We acknowledge the Texas Advanced Computing Center for computational resources, Qiang Zhu and Maximilian Amsler for insightful discussions, and Carol King for help with the manuscript.

Chapter 7

Mechanism of the $CaIrO_3$ Post-Perovskite Phase Transition Under Pressure

7.1 Abstract

Recent experiments have shown that the perovskite to post-perovskite phase transformation in $CaIrO_3$ occurs more readily at room temperature when a shear stress is applied as compared to isotropic pressure. To understand this mechanistically, we have calculated the minimum energy pathway of the phase transition with density functional theory under different pressure conditions with the generalized solid-state nudged elastic band method. Our results reveal that shear stress significantly lowers the barrier and stabilizes the product state, while isotropic pressure initially raises the barrier and only reduces the barrier at pressures above 90 GPa. The non-monotonic change in barrier with isotropic pressure is explained in terms of an increase in the activation volume under low pressure and a decrease under high pressure.

7.2 Introduction

Aided by laser-heating in a diamond anvil cell, the principal constituent of the Earth's lower mantle, $MgSiO_3$ perovskite (Pv), was recently found to

transform into a post-perovskite (pPv) structure above 125 GPa and 2500 K, which corresponds to the pressure and temperature conditions at the Earth's lowermost mantle, or D″ layer [95, 96, 97]. Following the discovery of pPv $MgSiO_3$, a number of other ABO_3 perovskites, e.g. $CaBO_3$ (B=Ru, Rh, Sn, Ir) have been transformed into the pPv structure under high-pressure and/or high-temperature conditions [98, 99, 100, 101, 102]. Unlike $MgSiO_3$, the Ca-based pPv are stable at ambient conditions, which makes them excellent analog materials of $MgSiO_3$.

Recently, high-pressure experiments on Pv $CaIrO_3$ demonstrate that the Pv to pPv transition can indeed be induced at room temperature at relatively low pressures in the presence of a significant shear stress [103, 104], whereas the Pv phase remains unchanged up to 31 GPa at room temperature under isotropic pressure conditions [105].

In order to understand the mechanism of the Pv–to–pPv transition under pressure, and especially in the presence of shear stress, it is important to determine the transition process at the atomic scale. In previous theoretical studies of $MgSiO_3$, the Pv–to–pPv transition has been determined under extremely high pressure conditions ($\geq$120 GPa) [97, 106]. It was found that the transition occurs through a shear or slide mechanism, which implies that shear stress should facilitate the Pv–to–pPv transition. However, the pressures and temperatures considered in the simulations were so high that the conclusions may not be extendable to room temperature and lower pressure conditions. All applied stresses in these previous studies were taken to be isotropic and

the role of pressure was primarily understood as stabilizing the pPv phase; how pressure affects the transition temperature and activation energy has not been investigated. Another concern about these previous studies is that the transition mechanisms were found only in the degrees of freedom used to define the periodic cell. This so-called rapid-nuclear-motion approximation [107] can give incorrect barriers, or fail to find a true minimum energy path if the reaction mechanism also involves motions of the atoms within the cell [85]. The focus of this work is thus to investigate the dynamics of Pv–to–pPv transition in $CaIrO_3$ under different pressure and shear conditions using the generalized solid-state nudged elastic band (G-SSNEB) method [85], which treats both cell and atomic degrees of freedom on equal footing.

A common approximation, within the context of transition state theory, is that the most probable reaction pathway is the minimum energy path (MEP) and the maximum energy along the path with respect to the initial state (the barrier) largely determines the rate of the reaction at a specified temperature. When the reaction pathway is determined, the influence of an external pressure on the barrier can also be calculated [108]. Under constant pressure, the energy landscape $E(\mathbf{R})$ can be generalized to an enthalpy landscape $H(\mathbf{R})$,

$$H(\mathbf{R}) = E(\mathbf{R}) + PV(\mathbf{R}), \tag{7.1}$$

where $\mathbf{R}$ represents the geometry configuration, P is the external pressure, and V is the volume of the system. The difference between the energy and enthalpy barrier is the $P\Delta V$ work done by the external pressure. For solid

state systems, the pressure can be anisotropic and should be expressed as a stress tensor. The work W done by the external pressure is then written in the general form

$$W = V \sum_{ij} \sigma_{ij}^{\text{ext}} \epsilon_{ij}, \tag{7.2}$$

where σ_{ij}^{ext} is the stress tensor and ϵ_{ij} is the strain tensor. In the low pressure regime, the barrier change is primarily from the work term. When the pressure is high enough, the barrier geometry can also change, and this contribution to the activation enthalpy cannot be ignored.[109]

The main results in this paper are as follows. First, we investigate the atomic mechanism of the Pv–to–pPv phase transition by locating the MEP in the enthalpy landscapes with the G-SSNEB method [85]. Our results directly show that shear stress decreases the barrier, while the isotropic pressure increases the barrier at low pressure and only decreases the barrier when the pressure is over 90 GPa. This surprising behavior is a result of the reaction pathway being along the shear deformation direction under all pressure conditions, while the volume can either expand or shrink from the reactant to the saddle point depending on the isotropic pressure applied. We also find an interesting intermediate minimum between the two phases, in which every other layer of iridium atoms are coordinated by four oxygen in a square-planar geometry. A nucleation-like layer by layer growth of the pPv phase is observed in a sufficiently large supercell.

7.3 Method

For solid state systems described by periodic boundary conditions, the geometric configuration vector $\mathbf{R}$ includes two types of variables: atomic positions $\mathbf{r}$, and cell vectors $\mathbf{h}$. To define distances in this generalized configuration space, a Jacobian (metric) is required to balance the two vectors. Our choice of Jacobian is made so that the ratio between distances is invariant to the supercell representation of the material. To satisfy this requirement, the distance between two points in configuration space is defined as

$$\|\Delta\mathbf{R}\| = \sqrt{NL^2\|\bar{\boldsymbol{\varepsilon}}\|^2 + \|\Delta\mathbf{r}\|^2}, \tag{7.3}$$

which is the norm of the generalized configuration vector

$$\begin{aligned} \Delta\mathbf{R} &= \left\{\sqrt{N}L\bar{\boldsymbol{\varepsilon}}, \Delta\mathbf{r}\right\} && (7.4)\\ &= \left\{J\bar{\boldsymbol{\varepsilon}}, \Delta\mathbf{r}\right\}, && (7.5) \end{aligned}$$

where $\bar{\boldsymbol{\varepsilon}}$ is the average strain, $\Delta\mathbf{r}$ is the pure atomic motion in Cartesian coordinates, N is the number of atoms in the supercell, L is the average distance between atoms, and $J = \sqrt{N}L$ is the Jacobian, which has the unit of this length. Based on the general distance defined above, the corresponding general force is

$$\mathbf{F} = \left\{\frac{\Omega}{J}(\boldsymbol{\sigma}^{\text{cauchy}} + \boldsymbol{\sigma}^{\text{ext}}), \mathbf{f}\right\}, \tag{7.6}$$

where Ω is the volume of the supercell; $\boldsymbol{\sigma}^{\text{cauchy}}$ and $\boldsymbol{\sigma}^{\text{ext}}$ are the Cauchy and the external stress, respectively; $\mathbf{f}$ is the regular atomic force. It is then clear that

$$\mathbf{F}\cdot\Delta\mathbf{R} = \Delta E + \Omega\boldsymbol{\sigma}^{\text{ext}}\cdot\bar{\boldsymbol{\varepsilon}} = \Delta H. \tag{7.7}$$

In this generalized coordination system, a structure optimization following the steepest decent direction is simply $\Delta\mathbf{R} = \alpha\mathbf{F}$. The nudged elastic band method implemented in the generalized coordination system is the G-SSNEB method [85].

In our calculations, the forces and stresses are evaluated with density functional theory (DFT) [31] using the general gradient approximation as implemented in the Vienna ab-initio simulation package [35, 36]. The Perdew-Wang functional is adopted for the exchange-correlation energy [32]. Core electrons are described by pseudo-potentials generated from the projector augmented wave method [14, 15], and valence electrons are expanded in a plane-wave basis set with an energy cutoff of 400 eV. A Hubbard model correction is applied to avoid over-delocalization of iridium $5d$ electrons due to self-repulsion. An effective U value of 2.8 eV is chosen to fit to the band gap of the pPv structure [110]. Unlike the electronic structure, the reaction pathway is not sensitive to small changes of the U value. For the same reason, spin-orbit coupling (SOC) is not considered in our calculations either.

7.4 Results

In contrast with the Pv structure, which has a three-dimensional network of corner-linked IrO_6 octahedra, the pPv structure consists of IrO_6 octahedral layers formed by both corner and edge sharing. The phase transition thus involves octahedral rotations and rearrangement. We started with the atom mapping reported in Ref. [97, 106, 104] as an initial path, and then

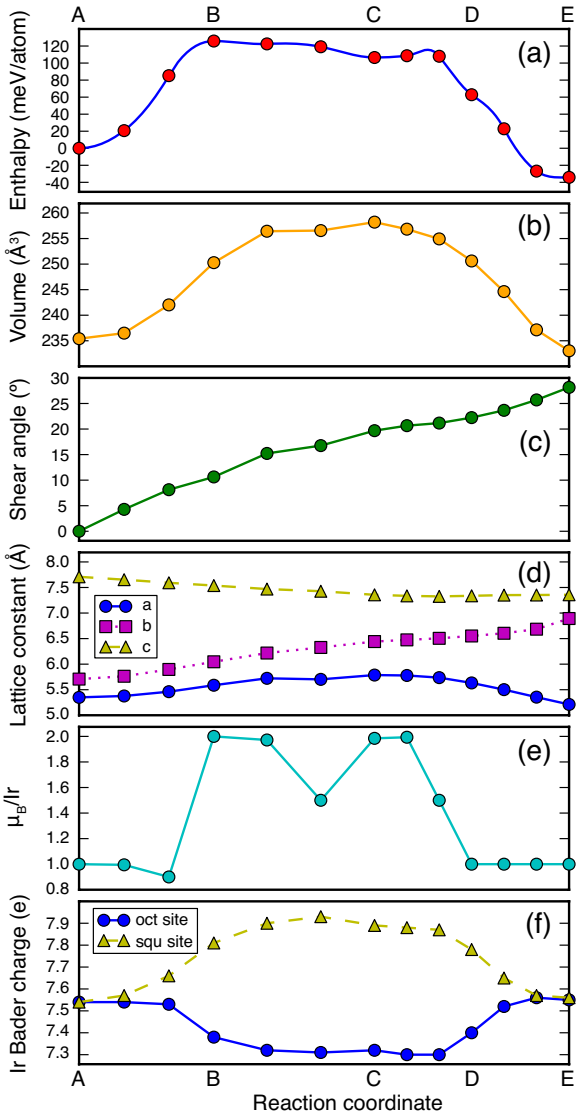

Figure 7.1: Properties of the minimum energy phase transformation path at zero pressure.

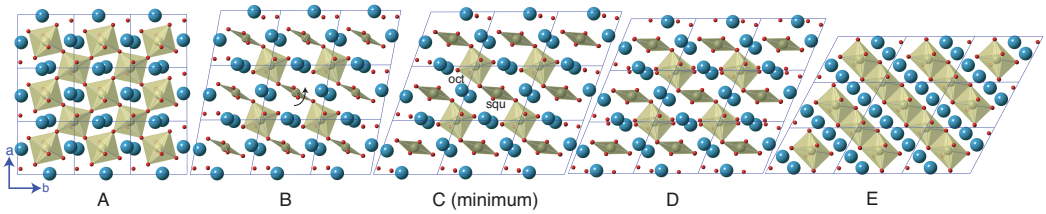

Figure 7.2: Structures along the minimum energy phase transformation path at zero pressure. The polyhedra are IrO_6; the big blue circles are Ca; the small red circles are O.

calculated the MEP with zero external pressure using the G-SSNEB. The converged MEP, shown in Fig. 7.1(a), is a concerted mechanism with a barrier of 125 meV/atom. Structures along the MEP are shown in Fig. 7.2. Along the transition path, the iridium atom in the center of the cell breaks two Ir-O bonds and forms a square planer coordination, while its four neighboring IrO_6 groups remain intact. Meanwhile the center IrO_4 plane rotates slightly to align the Ir-O bond parallel to the neighbors as the arrow indicates in structure B. As the cell continues shearing, two neighboring IrO_6 groups move closer to the center iridium atom and rotate around the shared oxygen to form two newIr-O bonds. Movies of the structural evolution can be found in the supporting information.

The intermediate minimum along the path, labeled C in Fig. 7.2, is characterized with alternating connected square-planar and octahedral units. The intermediate minimum is so shallow that this structure might be difficult to stabilize in an experiment. A Bader analysis [18, 19] for the images in Fig. 7.1(f) shows that a charge transfer occurs between two types of iridium

atoms; the iridium in octahedral sites lose electrons to the iridium in square-planar sites during the transition. This can be understood from crystal field theory. Each iridium atom in the Pv phase originally has five d-electrons in a low-spin configuration. As some sites become less coordinated, the elongation of the two oxygen bonds in the z-direction lowers the energy of d_{yz}, d_{xz}, and d_{z^2} orbitals. When the d_{z^2} level of the square-planar site is close to or lower than the t_{2g} level of the octahedral site, one paired electron from the latter level transfers to the former one to maximize the multiplicity. The Bader charges are not integers, but translated to the conventional picture of discrete charge transfer, they indicate that the octahedral iridium now has four d-electrons and the square-planar has six. This charge transfer picture is consistent with the increase of the average spin magnetic moment of iridium in Fig. 7.1(e). Although the value of the spin moment is not precise in the absence of SOC, there is no doubt that the charge transfer results in a spin moment change, which should be observable in experiment.

The volume change and shear deformation angle are plotted as a function of the reaction coordinate in Fig. 7.1(b, c). The volume increases first and then decreases, while the shear angle increases monotonously. Bell's theory says that the enthalpy barrier height is a linear function of external force [111, 109]. In a first order approximation, the positions of the saddle point and minima are not changed by the external force so that enthalpy barrier change due to the external force is only determined by the work term. Extended to solid state systems, Bell's theory says that in the low pressure

regime the barrier is a linear function of the stress tensor,

$$H^{\ddagger}(\boldsymbol{\sigma}^{ext}) - H^{0}(\boldsymbol{\sigma}^{ext}) = E^{\ddagger}(0) - E^{0}(0) \\ -\Omega^{0} \sum_{ij} \sigma_{ij}^{ext} \epsilon_{ij}^{\ddagger}(0), \tag{7.8}$$

where H^0 and $H^{\ddagger}$ are the enthalpies of the reactant and transition state, respectively. $E^0(0)$ and $E^{\ddagger}(0)$ are the energies of the reactant and transition state under zero pressure. The last term is the work done by the external stress from the reactant to the transition state. The isotropic compression is against the reaction direction (volume expansion), thus increasing the barrier; the shear stress is along the reaction direction (shear deformation), thus decreasing the barrier. In the high pressure regime, shifts of the critical points are significant so that new G-SSNEB calculations with the external stresses applied are required.

A set of MEPs and barriers from G-SSNEB calculations at different external compression conditions are plotted in Fig. 7.3. As expected from Eq. 7.8, the shear stress lowers the barrier whereas the isotropic pressure raises the barrier in the low pressure regime below 20 GPa. The barrier change, however, is clearly non-linear as the pressure increases and even drops after 30 GPa. After 90 GPa the isotropic pressure begins to lower the barrier compared to the zero pressure case. As shown in Fig. 7.3(a), the stabilization of the pPv product state due to isotropic pressure is significantly smaller than due to shear stress. At 120 GPa the energies of the two phases are even closer than at 40 GP, because the Pv phase is more compressible and has a slightly smaller equilib-

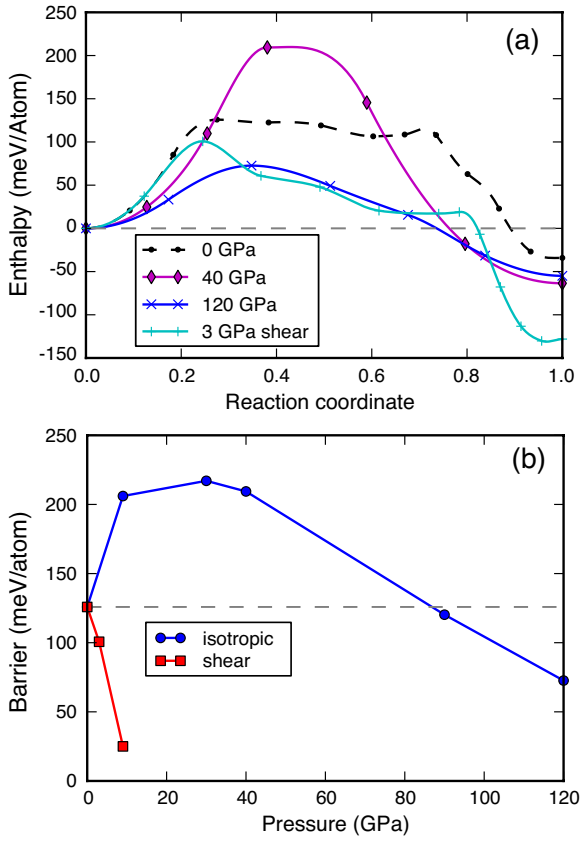

Figure 7.3: Comparison of different compression conditions: (a) MEPs under different pressures, with the energies of the Pv phases aligned to zero; (b) the enthalpy barriers as a function of pressure.

rium volume at the high pressure. It is worth noticing that the intermediate minimum no longer exists in the isotropic pressure calculations.

A detailed analysis at 30 GPa is plotted in Fig. 7.4. The volume shrinks slightly at the saddle point, while the shear deformation follows the same trend as under zero pressure. Taking the first order approximation from this point, it is expected that increasing the isotropic or shear pressure will both lower the barrier. The Bader analysis shows that under 30 GPa the charge transfer between the octahedral and square-planar sites are inhibited, resulting in a different spin moment transition along the path. As the pressure increases, the octahedral and square-planar sites tend to have similar local environment: both becoming stretched octahedra but with different orientations.

So far we have considered only the concerted mechanism which is described by a small unit cell. To investigate the possibility of a more localized phase transition mechanism, we enlarge the supercell size along the a and b directions. The zero pressure MEP calculations for this large cell are shown in Fig. 7.5. Instead of every other IrO_6 group rotating at the same time, now one layer transforms first and another layer follows, which agrees with the observation in Ref. [106]. A laminate structure (G) is observed as a new intermediate minimum along the path, which is recognized as a mixture of the Pv and pPv phases rather than a new phase. The ratio of the two phases in the laminate is limited by the supercell size selected for the calculation; it does not reflect the actual situation expected in experiment. The critical nucleus size of the new phase would be interesting, but it is hard to estimate with DFT because of the

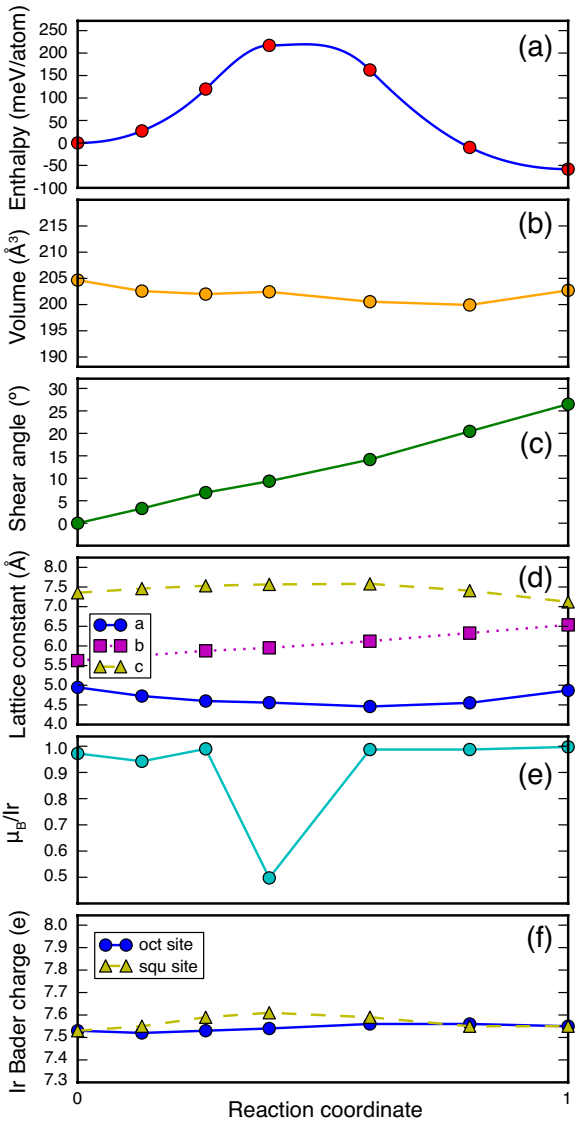

Figure 7.4: MEP at 30 GPa isotropic pressure and computed properties along the path.

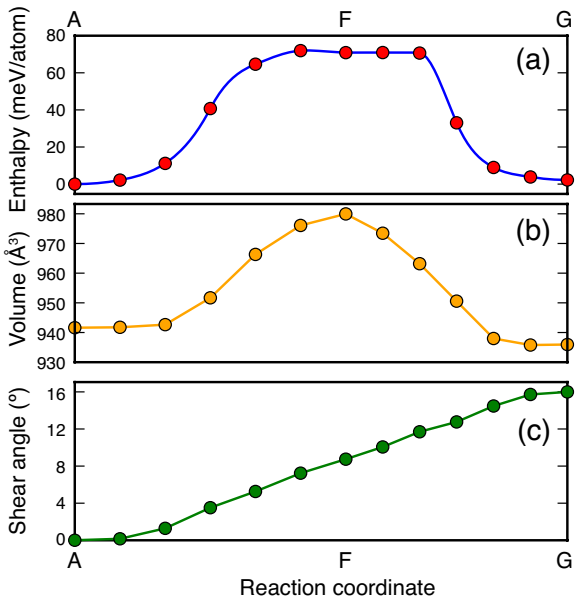

Figure 7.5: MEP of a larger supercell at zero pressure. The initial point (A) is the pure Pv phase; the intermediate (F) and final (G) states are shown in the following figure.

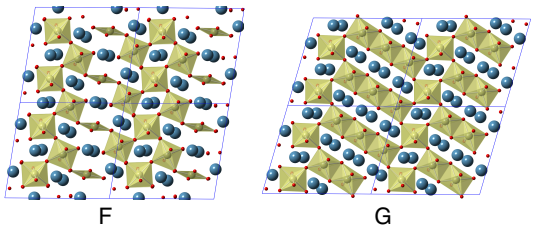

Figure 7.6: Structures of the intermediate (F) and final (G) minima of the larger supercell.

large cell sizes necessary. Switching from the concerted to the non-concerted mechanism, however, does not change the calculated trends of barrier as a function of pressure and sheer stress. The non-concerted mechanism introduces a phase boundary into the transition process, but the boundary does not change the volume or shear deformation direction along the path, as shown in Fig. 7.5(b, c).

7.5 Discussion

The role of temperature in the phase transition is to provide the system with fluctuations to overcome the reaction barrier. A higher barrier requires a higher temperature for the transition to occur. An applied stress can change the enthalpy landscape and thus the barrier height, either an increase or a decrease. At a given external pressure, the barrier height between the two phases can be related to the onset temperature of the transition. For the Pv–to–pPv phase transition in $CaIrO_3$, the barrier height increases with the external isotropic pressure, therefore we predict the onset temperature of the transition will also increase. A suitable experiment for testing our calculated mechanism is as follows: under a given pressure (helium mediated), gradually increase the temperature of the Pv phase to find the temperature when the pPv phase is first observed. Repeat the process at different pressures and get a series of onset temperatures. One possible obstacle is that without any shear stress, the temperature required to activate the transition might be too high, at pressures below 30 GPa. A possible solution is to maintain a constant

9 GPa shear stress and vary the helium gas pressure, which can bring down the barrier to an observable region and allow the study of the unusual isotropic stress effect. Measuring the spin magnetic moment change during the phase transition is another possible way to verify the predicted mechanism.

The Pv–to–pPv phase transition is similar to the iron *bcc*–to–*hcp* transition. The shear effect and the microstructures we find here both agree qualitatively with the multi-scale model results in Ref. [112]. In that work, the authors adopted the microstructure from experimental observations, while we find the laminate directly from atomic simulations.

7.6 Conclusion

In conclusion, we have provided a detailed mechanism of the Pv–to–pPv phase transition as a continuous path in the space of both atoms and lattice parameters. Based upon this path, we have shown how pressure and shear effects the reaction barrier. The shear stress lowers the barrier, while the isotropic pressure first raises the barrier and then lowers it with a crossover point of 90 GPa. These calculations explain the recent experimentally observed phase transformations under different compression conditions. Charge transfer between different iridium sites during the transition is predicted under low isotropic pressure or pure shear stress, which should be accompanied by a change in the spin magnetic moment. Bell's theory provides a straightforward understanding of the pressure effect from the transition path within small pressure deviation, but it may lead to completely opposite conclusion if the

applied stress is far from the perturbation limit.

7.7 Acknowledgments

This work is supported as part of the program "Understanding Charge Separation and Transfer at Interfaces in Energy Materials (EFRC:CST)" an Energy Frontier Research Center funded by the US Department of Energy, Office of Science, Office of Basic Energy Sciences under Award Number DE-SC0001091. Calculations were done with resources from the National Energy Research Scientific Computing Center and the Texas Advanced Computing Center. We thank Libin Zhang for helpful discussions.

Chapter 8

Solid-State Dimer Method for Calculating Solid-Solid Phase Transitions

8.1 Abstract

The dimer method is a minimum mode following algorithm for finding saddle points on a potential energy surface of atomic systems. Here, the dimer method is extended to include the cell degrees of freedom for period solid-state systems. Using this method, reaction pathways of solid-solid phase transitions can be determined without having to specify the final state structure or reaction mechanism. Example calculations include concerted phase transitions between CdSe polymorphs and a nucleation and growth mechanism for the A15 to BCC transition in Mo.

8.2 Introduction

The harmonic approximation to transition state theory [113, 114] is widely used to calculate reaction rates because it depends simply upon the energy difference between a local minimum and a saddle point connected to it by a steepest descent path. The dimer method is an efficient way to locate these first order saddle points on a given potential energy surface. [115, 116] Different

from the nudged elastic band method (NEB), [59, 58] where both the reactant and product configurations are needed to find a connecting saddle point, the dimer method requires only initial configurations in the reactant state and can (in principle) find all connected saddles defining the possible escape pathways from the state. The corresponding product states are identified by minimizing configurations displaced along the negative mode of each saddle point found. Using dimer searches in each new state visited, the adaptive kinetic Monte Carlo (AKMC) algorithm has been developed to explore the connectivity and thermally accessible parts of the potential energy surface. [117] Possible reaction processes and rates are calculated on the fly based on the saddles found by the dimer method and the system is advanced from state-to-state by the kinetic Monte Carlo (KMC) algorithm. [118, 119]

Within the dimer method the *dimer* consists of two configurations of the system separated by a small distance. The vector between the two images, $\boldsymbol{\tau}$, is an estimate of the lowest curvature mode, which is used to bring the center of the dimer to a saddle point. There are two parts to the dimer method. First, the dimer is rotated about its center to minimize the total dimer energy and with this to find the lowest curvature mode. The rotation direction $\boldsymbol{\Theta}$, is along the force difference between the two images, with the component parallel to $\boldsymbol{\tau}$ projected out. The dimer energy is a sinusoidal function of the rotation angle on the plane spanned by $\boldsymbol{\Theta}$ and $\boldsymbol{\tau}$, so the rotation angle which minimizes the dimer energy in this plane can be determined with a single additional force call. [120, 121] Second, the center of the dimer is translated by climbing up

the potential energy surface along the lowest curvature mode direction and relaxing in all perpendicular directions. The dimer converges towards first order saddle points and is oriented along the negative curvature mode defining the reaction coordinate.

For solid-state systems, periodic boundary conditions are adopted to model infinite systems. Many solid-state reactions, and especially phase transitions, involve changes of both atomic positions and cell vectors. To correctly locate saddle point configurations in these systems, it is essential to treat all degrees of freedom on the same footing. Dragging along a chosen direction in solid-state systems, such as moving the cell first and then relaxing the atoms in a fixed cell, or vice versa, is not a reliable way to find saddle points. [122, 65] Here, we show how the dimer algorithm can be extended to include the cell degrees of freedom becoming the solid-state dimer (SSD) method. In the SSD, both the cell and atomic degrees of freedom evolve in concert. The key to the method is the definition of an appropriate metric to define the distance between two structures so that the geometry of the configuration space is independent of the supercell used.

Our approach follows that of the solid-state nudged elastic band (SS-NEB), which was developed using the same expanded degrees of freedom to locate saddle points of solid-solid phase transitions. [122] The limitation of any band type method is that both the initial and final configurations must be known to initiate the calculation, as well as a suitable initial interpolation between the two states. This is not a problem when studying simple diffusion

mechanisms, however the complexity of phase transitions makes this constraint a major challenge. In the NEB, the identity of each atom in the initial state must correspond uniquely to a specific atom in the final state. This atomic mapping creates a combinatorial explosion of possible final states with system size, differing only by atom identity. Moreover, the choice of unit cell for each state is not unique, which further increases the complexity of the mapping. The SSD method circumvents the atom permutation and cell variation issues by automatically following the atoms along the path they naturally take to saddle points and adjacent minima. Then, combined with the AKMC method, the SSD is able to automatically discover new crystal structures and new phase transformation mechanisms.

8.3 Methodology

8.3.1 Generalized Cell and Atom Configuration Space

The energy of a solid-state system represented with periodic boundary conditions is defined by the atomic positions $\mathbf{r}$ and the cell matrix $\mathbf{h}$ (with the cell vectors as rows). In the SSD, we aim to treat both types of variables in a single generalized space of atomic and cell coordinates. Changes in the cell vectors are naturally described in terms of strains which have different units from the atomic positions. A Jacobian, or metric, is required to combine them into a generalized displacement vector,

$$\Delta\mathbf{R} = \{J\boldsymbol{\varepsilon}, \Delta\mathbf{r}\}\,. \tag{8.1}$$

Here, J is the Jacobian, $\boldsymbol{\varepsilon} = \mathbf{h}^{-1}\Delta\mathbf{h}$ is the strain, and $\Delta\mathbf{r}$ is the change in the atomic positions in Cartesian coordinates. $\boldsymbol{\varepsilon}$ is still a 3×3 matrix. $\Delta\mathbf{R}$ is formally a $(N + 3) \times 3$ matrix, where N is the number of atoms in the supercell, but the dot product and norm used in the following are just calculated as flattened vectors. [122] The strain is calculated with respect to the initial cell geometry. It could also be calculated with respect to deformed cell, $\boldsymbol{\varepsilon} = (\mathbf{h} + \Delta\mathbf{h})^{-1}\Delta\mathbf{h}$, but this is not important for the metric because the two expressions for $\boldsymbol{\varepsilon}$ converge in the limit of $\Delta\mathbf{h} \to 0$, where the differential properties of the space are defined.

To separate atomic and cell changes, it is important to define the atomic motion in relative coordinates with respect to the cell vectors. In this way, a pure strain $\boldsymbol{\varepsilon}$ in the generalized space does not contribute to a change in the atomic coordinates $\Delta\mathbf{r}$. The separation of cell and atomic variables is accomplished by calculating $\Delta\mathbf{r}$ as fractional changes along the cell coordinates, converted into Cartesian displacements. As with the calculation of $\boldsymbol{\varepsilon}$, $\mathbf{h}$ is chosen as the reference cell for this transformation.

The most import issue for defining the space of cell vectors and atomic positions is the choice of Jacobian. The Jacobian provides the appropriate metric to combine strain and atom motion into a single vector. Our principle for choosing J is that overall size and shape of the supercell should not affect

the calculation of distances in our generalized space. Our choice of J is

$$J = \sqrt{N}L \tag{8.2}$$

$$L = \left(\frac{\Omega}{N}\right)^{1/3}, \tag{8.3}$$

where N is the number of atoms in the supercell, L is the average distance between atoms calculated from the average volume, and Ω is the volume of the supercell. J has units of length, which compensates for the fact that $\boldsymbol{\varepsilon}$ is unitless. J is only calculated once in the initialization of the calculation and kept constant thereafter. A constant J is sufficient because the precise value is not as important as how J scales with system size. Furthermore, the saddle points are stationary and invariant to the Jacobian.

The distance in the generalized configuration space is

$$\|\Delta\mathbf{R}\| = \sqrt{NL^2\|\boldsymbol{\varepsilon}\|^2 + \|\Delta\mathbf{r}\|^2}. \tag{8.4}$$

One can see from this expression how J balances the relative weight between strain $\boldsymbol{\varepsilon}$ and atomic displacements $\Delta\mathbf{r}$. Consider, for example, a cell that is expanded into a supercell while maintaining the same atomic motion within each cell. The first term under the square root, corresponding to strain, increases linearly with the number of atoms in the cell, due to the $\sqrt{N}$ term in J (Eq. 8.2). The second term, corresponding to the atomic motion, also increases linearly with the number of atoms in the supercell. The Jacobian ensures that the ratio of the two terms remains the same, independent of the choice of supercell, resulting in a proportional change of the atomic and cell

axes in the generalized space. It is trivial to prove that the dot product and angle between any two vectors also remains unchanged under different supercell representations, which confirms that the configuration space is undistorted.

Taking the first derivative of the energy with respect to $\mathbf{R}$ gives the generalized force

$$\mathbf{F} = \left\{ \frac{\Omega}{J} \boldsymbol{\sigma}^{\text{cauchy}}, \mathbf{f} \right\}, \tag{8.5}$$

where $\mathbf{f}$ are the atomic forces and $\boldsymbol{\sigma}^{\text{cauchy}}$ is the Cauchy stress. One can verify that $\mathbf{F} \cdot \Delta\mathbf{R}$ is the energy difference due to the displacement $\Delta\mathbf{R}$. The SSD can be extended by include external stress in an enthalpy landscape by modifying Eq. 8.5 to

$$\mathbf{F} = \left\{ \frac{\Omega}{J} (\boldsymbol{\sigma}^{\text{cauchy}} + \boldsymbol{\sigma}^{\text{external}}), \mathbf{f} \right\}. \tag{8.6}$$

8.3.2 Solid-state Dimer Method

The dimer is defined by a point $\mathbf{R}$ and a direction $\boldsymbol{\tau}$. In the generalized space of cell and atomic degrees of freedom $\mathbf{R}$ has two components, $\mathbf{h}$ and $\mathbf{r}$. As in Eq. 8.1, the direction is defined as $\boldsymbol{\tau} = \{\boldsymbol{\tau}_\varepsilon, \boldsymbol{\tau}_\mathbf{r}\}$, where $\boldsymbol{\tau}_\epsilon$ and $\boldsymbol{\tau}_\mathbf{r}$ are the components from strain and atomic motions, respectively. The dimer can also be defined by its two end points, i.e. the two images of the system at $\mathbf{R}_1$ and $\mathbf{R}_2$, which are centered about $\mathbf{R}$ and separated along $\boldsymbol{\tau}$ by a small distance $\|\Delta\mathbf{R}\|$. $\mathbf{R}_1$ is calculated from $\mathbf{R}$ and $\boldsymbol{\tau}$ in the following way. First, the cell at

the endpoint, $\mathbf{h}_1$ is calculated as

$$\boldsymbol{\varepsilon} = \frac{\|\Delta\mathbf{R}\|}{J}\boldsymbol{\tau}_\epsilon \tag{8.7}$$

$$\mathbf{h}_1 = \mathbf{h}\boldsymbol{\varepsilon} + \mathbf{h}. \tag{8.8}$$

Under the strain $\boldsymbol{\varepsilon}$, the Cartesian atomic positions are scaled from $\mathbf{r}$ to a new position vector that we will call $\mathbf{r}'$. Note that the relative atomic coordinates in these cells are constant, when expressed as fractions of the cell vectors. After transforming to the new cell, the atomic positions are updated according to $\boldsymbol{\tau}_\mathbf{r}$,

$$\mathbf{r}_1 = \mathbf{r}' + \|\Delta\mathbf{R}\|\boldsymbol{\tau}_\mathbf{r}. \tag{8.9}$$

With these definitions of generalized vectors, forces, and displacements, the rest of the SSD method is the same as the regular dimer method. [115, 120, 121] The dimer direction $\boldsymbol{\tau}$ is rotated according to the force differences between the two images; at the new orientation the end point is updated and the new forces are calculated; after $\boldsymbol{\tau}$ converges to the lowest curvature mode direction, the center of dimer is translated up the potential along $\boldsymbol{\tau}$ and down the potential in all other directions, using any force-based optimizer, until a saddle point is found. We note that the dimer rotation is equivalent to the Raleigh-Ritz optimization [123] that is used in the hybrid eigenvector following method [124], and the more recent and closely related gentlest ascent dynamics method [125].

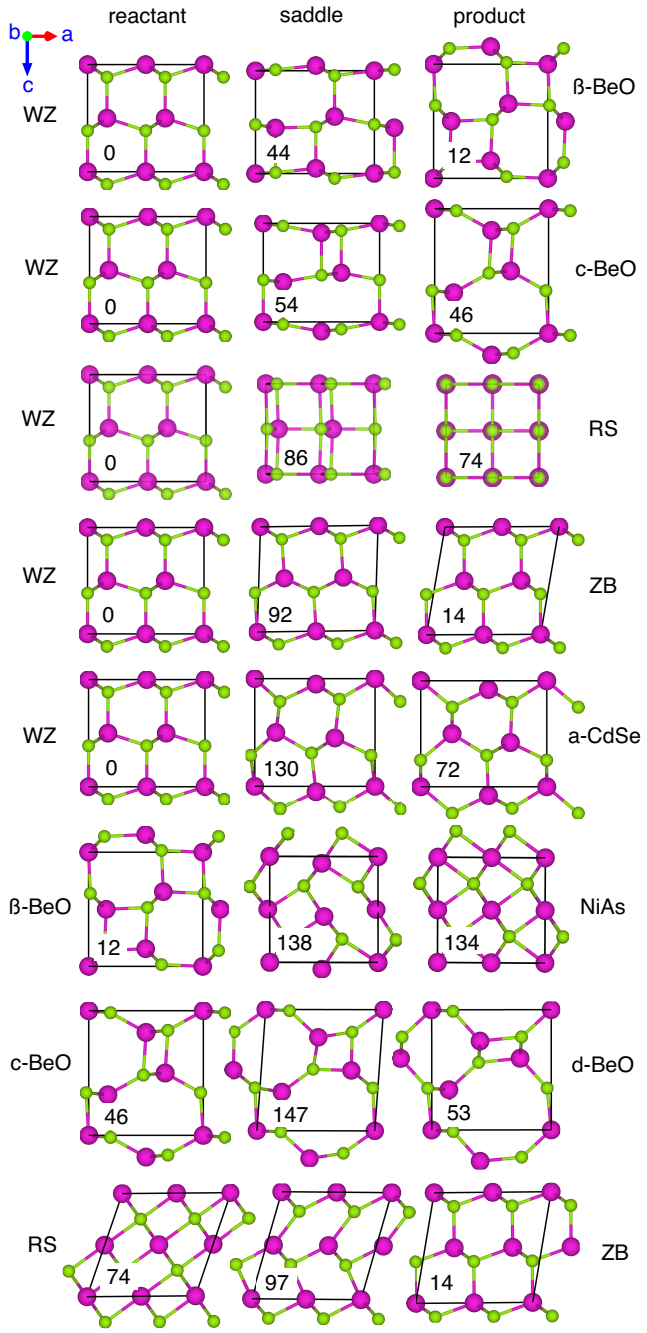

Figure 8.1: Several phase transition mechanisms found by the SSD. Energy values are in meV/atom with respect to the WZ structure. Abbreviations of the structures are defined in the main text. The purple circles are Cd, and the green ones are Se.

8.4 Results

The SSD method is implemented as an extension of the atomic simulation environment (ASE) in the companion transition state (TSASE) code. [70, 71] Exploration of the potential energy surface is done using the AKMC method [126, 117] as implemented in the EON simulation package. [127] We use high temperature state-to-state AKMC dynamics to facilitate crossing of high barriers and sampling of both low and high energy crystal structures.

Two examples are used to demonstrate the capabilities of the SSD method. In the first example, we revisit the CdSe system previously explored with the SSNEB. [122] In addition to the transition pathways found with the SSNEB, the SSD finds many new structures which are illustrated in a disconnectivity graph. [128] In the second example, we calculate a phase transition between the A15 and BCC structures in Mo. With the SSD, two concerted mechanisms of the phase transition are found, without an assumed path or input from molecular dynamics. Finally, we combine the SSD and the SSNEB methods into an efficient strategy for discovering and refining reaction mechanisms. A small supercell representation serves as a coarse-grained model of the system which can be quickly explored by the SSD; the finer details along the pathway of interest, for example at the interfaces between phases, are then refined with the SSNEB.

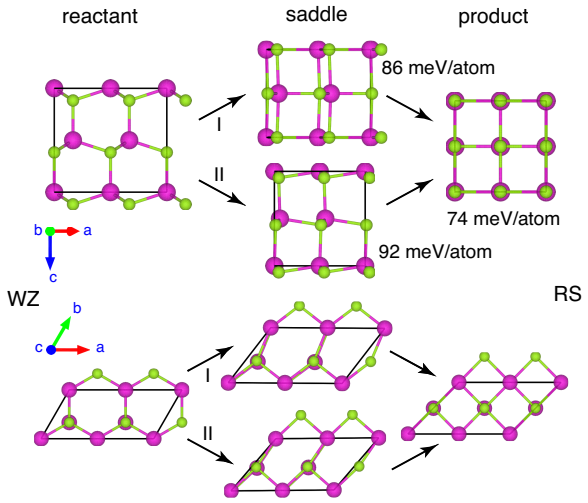

Figure 8.2: Top and side views of two pathways from the wurtzite (WZ) to rock salt (RS) structure. Remarkably, there is the same atomic mapping between the reactant and product states for both mechanisms.

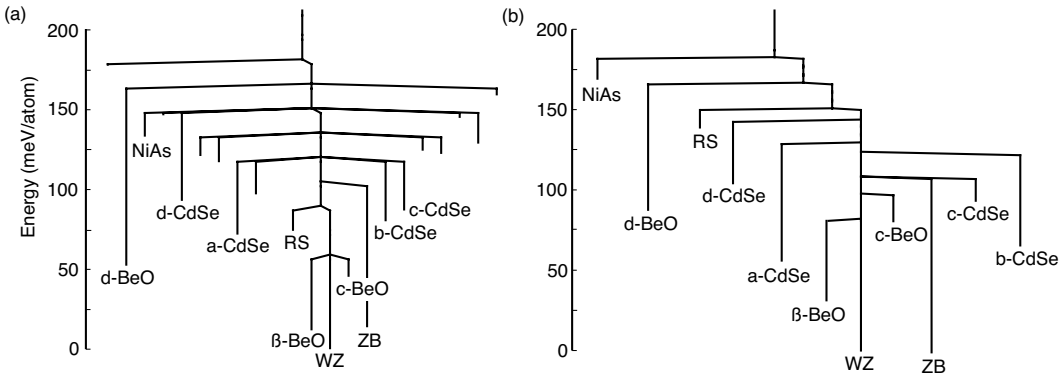

Figure 8.3: A disconnectivity graph of the eight atom CdSe system calculated with (a) an empirical potential and (b) density functional theory. Several of the ordered low energy structures are labelled.

8.4.1 CdSe energy landscape

Our first example is the CdSe system with eight atoms in the supercell, which we have studied using the SSNEB method in a previous paper. [122] The same empirical potential, consisting of long range Coulomb and short range Lennard-Jones terms, describes the atomic interactions. [68] The initial structures for SSD searches are generated by the EON server with random displacements in the generalized space around the wurtzite (WZ) minimum. After the saddles around the minimum are found, the EON server builds a table of reaction rates based upon harmonic transition state theory, and advances the system to a new state with the KMC algorithm. A temperature of 5000 K is used to explore the network of stable crystal structures.

A selected set of saddle points and final state crystal phases found by the SSD are shown in Fig. 8.1. Interestingly, two concerted mechanisms were found for the WZ to rock salt (RS) transition. Fig. 8.2 illustrates both the lower energy path (I), shown in Fig. 8.1, and a slightly higher energy path (II). In path I, the cell contracts first along the c-axis and then along the a-axis; in path II, the cell has contracted both along the a- and c-axes at the saddle point. This example illustrates a strength of single-ended saddle search methods which are not biased to a particular path between an initial and final state. In contrast, the SSNEB using an initial linear interpolation between the two states would only find one of these pathways.

The resulting energy landscape is shown in the disconnectivity graph in Fig. 8.3 (a). The most interesting high symmetry and low energy structures

were relaxed with density functional theory (DFT) calculations, [31] yielding the energy landscape shown in Fig. 8.3 (b). The DFT calculations were performed with the Vienna *ab-initio* simulation package (VASP) using the PW91 exchange-correlation functional and a basis set of plane waves with an energy cutoff of 350 eV. [35, 36, 32] The projector augmented wave method modeled the core electrons. [14, 15] All of the stable structures found with the empirical potential were also found to be distinct minima when fully relaxed in DFT. Transition states between the minima were calculated using the SSNEB within the VASP code, using the minimum energy paths from the empirical potential to initialize the DFT calculations.

The palm-tree shape of the energy landscape calculated with the empirical potential remains intact with DFT, but the lowest barrier to escape the WZ phase increases significantly and the RS and NiAs branches become less stable within the tree. Overall, however, the empirical potential gives reliable structures over the range of local minima as well as reasonable relative energy differences between them. The phase transition barriers, however, deviate significantly from the DFT results. A good compromise can be made by finding structures and pathways with the empirical potential and then refining the energetics with DFT.

Finding new crystal structures in this way can be useful for screening of materials with interesting properties. The energy landscape also provides information about which materials can be synthesized. [129] The WZ and zinc blende (ZB) are the two structures that are observed in experiments at

low temperature and pressure. The funneled "palm-tree" energy landscape explains why the two lowest energy states, WZ and ZB, are relatively easy to synthesize by annealing. The NiAs structure has also been observed in a constant pressure molecular dynamics simulation, but it may be difficult to stabilize under experimental conditions due to the shallowness of its basin of attraction. [130] The d-BeO and a-CdSe structures have not been reported before. Their basins of attraction are deep, but the entrances are relatively high in the energy funnel. If these entrances are bypassed at high temperature, the chances to visit the d-BeO and a-CdSe structures by annealing will be low.

8.4.2 A combined dimer and NEB approach to find complex pathways

Typically, we are interested in phase transitions between stable crystal structures in which the end points can be fully represented by a small supercell. The SSD efficiently finds concerted mechanisms of phase transitions in small cells, but these may not be sufficient to describe the details of a real transition processes, such as one involving nucleation and growth. [131] As the cell size is increased, complex and local mechanisms can be resolved, but it becomes increasingly difficult for the SSD to find complete phase transition pathways in the high dimensional configuration space.

A natural compromise between the mechanistic limitations of a small cell and the computational cost of a large cell can be achieved by combining the SSD and SSNEB methods. We start with a small cell and use the SSD to

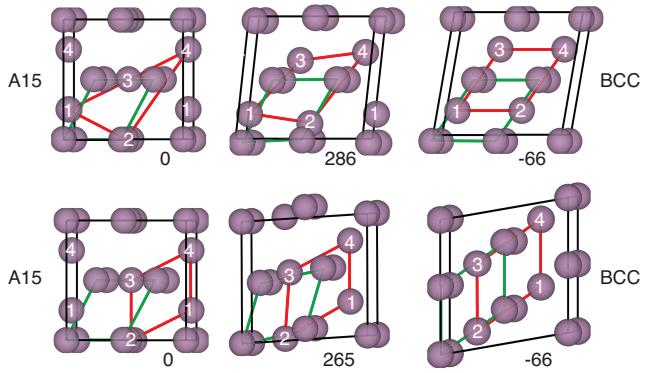

Figure 8.4: Two concerted mechanisms of the A15 to BCC phase transition in Mo. The moving atoms are labeled, and the two sub-lattices outlined for visualization purposes. Energies, listed below each structure, are in meV/atom.

find interesting concerted transitions. Then the SSNEB is used with a larger supercell to allow for local relaxation along the path found by the SSD. Small random displacements are made to the atoms in the SSNEB calculations in order to break the symmetry of the concerted processes found by the SSD. In this way, the coarse grained mechanisms are found by the SSD and the fine grained mechanistic details, including local nucleation and growth, are resolved by the SSNEB.

8.4.3 A15 to BCC solid-solid transformation in Mo

In our second example we show how the SSD can be combined with the SSNEB to efficiently discover and refine details of a complex transformation process in bulk Mo. Complex crystal structures, such as the A15 phase, can form in metal alloys with high concentrations of refractory elements (e.g.

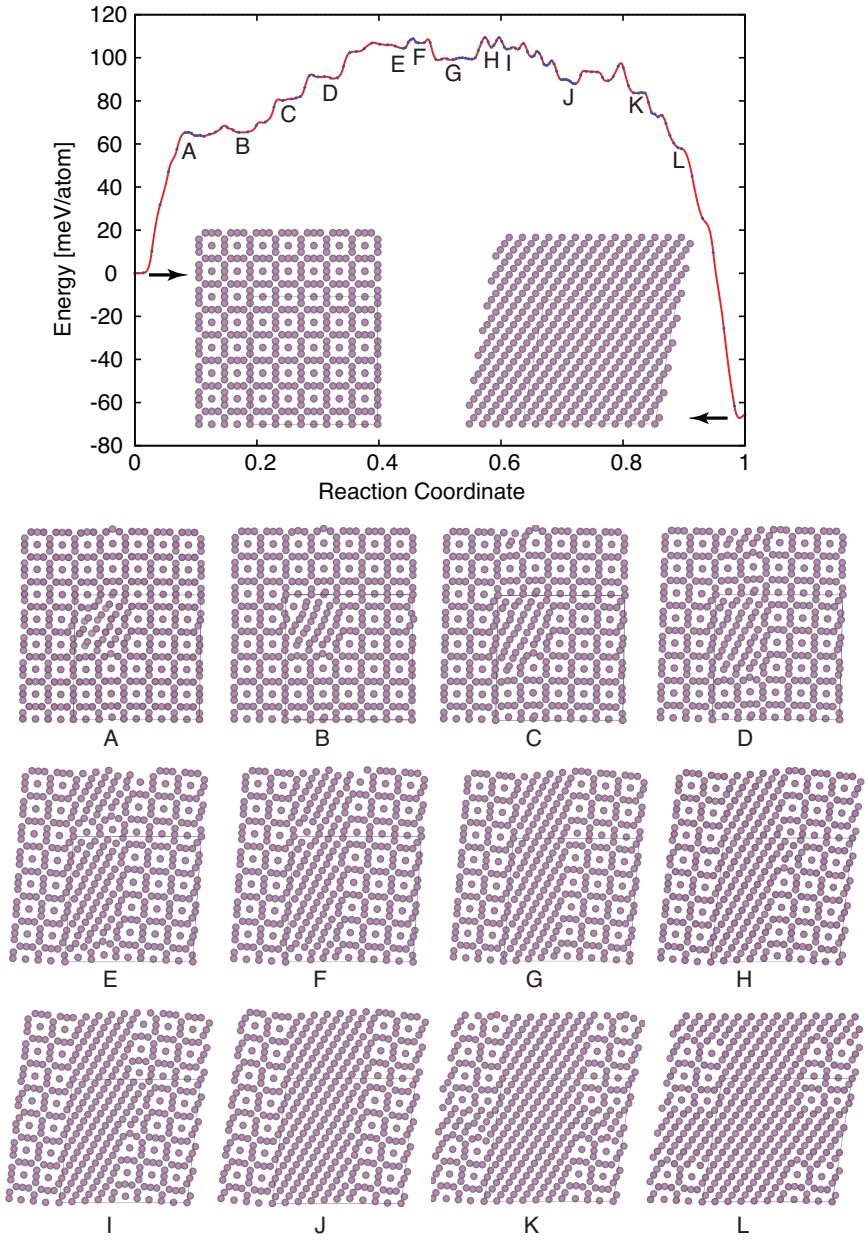

Figure 8.5: A localized nucleation and growth mechanism for the A15 to BCC phase transition in Mo as calculated in a 5×5×1 supercell by the SSNEB method. Several metastable structures along the minimum energy path are shown.

Mo) and significantly influence their mechanical properties, [132]. There is, however, little understanding of the atomistic mechanisms underlying the formation of these phases. The A15 phase is usually only observed in binary or multicomponent alloys, but to a first approximation elemental Mo is a good model system for this work since theoretical studies showed that in Mo the A15 phase is only slightly less stable than and thus competing with the BCC ground state. [**?**, 133]. Furthermore there is an embedded atom method potential for Mo [134] that gives reasonable bulk properties for BCC and A15 as well as an appropriate value for the energy difference between the two phases. To investigate the possible transition paths, we ran several hundreds of SSD searches initiated by making random displacements to all degrees of freedom in the A15 structure. Two concerted mechanisms were found as shown in Fig. 8.4. In both cases, atomic and cell motions are significant.

Based on the first concerted path in Fig. 8.4, we expand the supercell of the initial and final structures and use the SSNEB to refine the minimum energy pathway. This cell is expanded into a $5\times5\times1$ supercell within the plane shown in Fig. 8.4. In this way, we are looking at a quasi-2D system with a periodic unit cell in the perpendicular direction. The converged MEP is shown in Fig. 8.5. In the larger supercell, the initial path, taken to be the concerted mechanism found by the SSD, relaxes to a lower energy local transition in which the BCC phase nucleates locally and propagates throughout the cell. The overall barrier along the path is reduced from 286 meV/atom in the concerted mechanism to 109 meV/atom in the local mechanism. We note,

however, that the barriers for the concerted and local mechanisms can not be compared directly since they scale differently with system size; the former with the volume of the system and the later with the area of the A15-BCC interface. By choosing a large enough supercell, the concerted mechanism can be relaxed with the SSNEB to a lower energy nucleation and growth mechanism. [122]

The nucleus of the new phase forms in the middle of configuration (A) with a sharp increase in energy. In (B) the nucleus takes a clear BCC structure. The BCC phase then grows along the vertical direction unit cell by unit cell following atomic motion similar to that shown in Fig. 8.4. The energy increases as the nucleus grows. In principle, the state with the highest energy corresponds to the critical nucleus, but in this simulation the critical size is not reached before the nucleus spans the periodic boundary, in (F). From (G), the BCC phase grows along the two phase boundary and the energy drops due to the relative stability of BCC over A15 and the fact that the overall length of the boundary barely increases. From (G) to (J) a complete layer of A15 is converted into BCC, one unit cell at a time. After (J), the BCC growth mechanism is again affected by the periodic boundary conditions. Configuration (L) can be viewed as an A15 nucleus, which is relatively unstable with respect to the final pure BCC phase.

8.5 Conclusion

The SSD method is designed to find saddle points in the generalized configuration space of both atomic and cell degrees of freedom. The method

is demonstrated to find phase transitions between different crystal structures represented under periodic boundary conditions. Combined with the AKMC server in EON, the energy landscape of CdSe is calculated in the form of a disconnectivity graph. In this way, the discovery of new phases, as well as a determination of their stability is possible, which is a helpful guide for synthesis. More complex mechanisms involving both local atomic motion and collective shifts in the cell can be found with a combination of the SSD and SSNEB methods. The SSD efficiently finds collective transformation mechanisms in a small supercell and the SSNEB is able to refine the path in terms of local atomic motion along the path. This hybrid approach is used to determine a quasi-2D nucleation and growth pathway for the Mo A15-BCC phase transition.

8.6 Acknowledgments

The method development work was supported by the National Science Foundation under Grant Number CHE-1152342, and the calculations were supported as part of the program "Understanding Charge Separation and Transfer at Interfaces in Energy Materials (EFRC:CST)" an Energy Frontier Research Center funded by the US Department of Energy, Office of Science, Office of Basic Energy Sciences under Award Number DE-SC0001091. Calculations were done with resources from the National Energy Research Scientific Computing Center and the Texas Advanced Computing Center. We would like to thank Rye Terrell, Ari Harjunmaa, and Ralf Drautz for helpful discussions and

related research on the A15 to BCC phase transition.

Bibliography

[1] Michael M Thackeray, Sun-Ho Kang, Christopher S Johnson, John T Vaughey, Roy Benedek, and S A Hackney. Li_2MnO_3-stabilized $LiMO_2$ (M = Mn, Ni, Co) electrodes for lithium-ion batteries. *J. Mater. Chem.*, 17:3112, 2007.

[2] Alastair D. Robertson and Peter G. Bruce. Mechanism of electrochemical activity in Li_2MnO_3. *Chem. Mater.*, 15(13):1984–1992, 2003.

[3] Denis Y. W. Yu, Katsunori Yanagida, Yoshio Kato, and Hiroshi Nakamura. Electrochemical activities in Li_2MnO_3. *J. Electrochem. Soc.*, 156(6):A417, 2009.

[4] D Pasero, V McLaren, S De Souza, and A.R. West. Oxygen nonstoichiometry in Li_2MnO_3: An alternative explanation for its anomalous electrochemical activity. *Chem. Mater.*, 17(7):345–348, 2005.

[5] A. Robert Armstrong, Michael Holzapfel, Petr Novák, Christopher, S. Johnson, Sun-Ho Kang, Michael M. Thackeray, and Peter G. Bruce. Demonstrating oxygen loss and associated structural reorganization in the lithium battery cathode $Li[Ni_{0.2}Li_{0.2}Mn_{0.6}]O_2$. *J. Am. Chem. Soc.*, 128:8694–8698, 2006.

[6] Z. Q. Deng and A. Manthiram. Influence of cationic substitutions on the oxygen loss and reversible capacity of lithium-rich layered oxide cathodes. *J. Phys. Chem. C*, 115:7097–7103, 2011.

[7] V. L. Chevrier, S. P. Ong, R. Armiento, M. K. Y. Chan, and G. Ceder. Hybrid density functional calculations of redox potentials and formation energies of transition metal compounds. *Phys. Rev. B*, 82:075122, 2010.

[8] David O. Scanlon, Aron Walsh, Benjamin J. Morgan, and Graeme W. Watson. An *ab initio* study of reduction of V_2O_5 through the formation

of oxygen vacancies and Li intercalation. *J. Phys. Chem. C*, 112:9903–9911, 2008.

[9] Yoyo Hinuma, Ying S. Meng, Kisuk Kang, and Gerbrand Ceder. Phase transitions in the $LiNi_{0.5}Mn_{0.5}O_2$ system with temperature. *Chem. Mater.*, 19:1790–1800, 2007.

[10] Lei Wang, Thomas Maxisch, and Gerbrand Ceder. Oxidation energies of transition metal oxides within the GGA+U framework. *Phys. Rev. B*, 73:195107, 2006.

[11] Benjamin J. Morgan and Graeme W. Watson. A DFT + U description of oxygen vacancies at the TiO_2 rutile (1 1 0) surface. *Surface Science*, 601:5034–5041, 2007.

[12] G. Kresse and J. Hafner. Ab initio molecular dynamics for liquid metals. *Phys. Rev. B*, 47:R558–R561, 1993.

[13] J. P. Perdew and Y. Wang. Accurate and simple analytic representation of the electron-gas correlation energy. *Phys. Rev. B*, 45:13244–13249, 1992.

[14] P. E. Blöchl. Projector augmented-wave method. *Phys. Rev. B*, 50:17953, 1994.

[15] G. Kresse and D. Joubert. From ultrasoft pseudopotentials to the projector augmented wave method. *Phys. Rev. B*, 59:1758, 1999.

[16] J. Heyd, G. E. Scuseria, and M. Ernzerhof. Influence of the exchange screening parameter on the performance of screened hybrid functionals. *J. Chem. Phys.*, 124:219906, 2006.

[17] M. Marsman, J. Paier, A. Stroppa, and G. Kresse. Hybrid functionals applied to extended systems. *J. Phys.: Condens. Matter*, 2222:064201, 2008.

[18] R. F. W. Bader. *Atoms in Molecules: A Quantum Theory*. Oxford University Press, New York, 1990.

[19] W. Tang, E. Sanville, and G. Henkelman. A grid-based bader analysis algorithm without lattice bias. *J. Phys.: Condens. Matter*, 21:084204, 2009.

[20] A. K. Padhi, K. S. Nanjundaswamy, and J. B. Goodenough. Phospho-olivines as positive-electrode materials for rechargeable lithium batteries. *J. Electrochem. Soc.*, 144:1188–1194, 1997.

[21] Li-Xia Yuan, Zhao-Hui Wang, Wu-Xing Zhang, Xian-Luo Hu, Ji-Tao Chen, Yun-Hui Huang, and John B. Goodenough. Development and challenges of $LiFePO_4$ cathode material for lithium-ion batteries. *Energy Environ. Sci.*, 4(2):269–284, 2011.

[22] Atsuo Yamada, Sai-Cheong Chung, and Koichiro Hinokuma. Optimized $LiFePO_4$ for lithium battery cathodes. *J. Electrochem. Soc.*, 148(3):A224–A229, 2001.

[23] Shyue Ping Ong, Anubhav Jain, Geoffroy Hautier, Byoungwoo Kang, and Gerbrand Ceder. Thermal stabilities of delithiated olivine MPO_4(M = Fe, Mn) cathodes investigated using first principles calculations. *Electrochem. Comm.*, 12(3):427–430, 2010.

[24] N Ravet, J. B. Goodenough, S. Besner, M. Simoneau, P. Hovington, and M. Armand. Abstract no. 127. In *196th Meeting of the Electrochemical Society, HI*, 1999.

[25] N Ravet, Y Chouinard, JF Magnan, S Besner, M Gauthier, and M Armand. Electroactivity of natural and synthetic triphylite. *J. Power Sources*, 97:503–507, 2001.

[26] H Huang, S-C Yin, and LF s Nazar. Approaching theoretical capacity of lifepo4 at room temperature at high rates. *Electrochem. Solid-State Lett.*, 4(10):A170–A172, 2001.

[27] Shin-ichi Nishimura, Genki Kobayashi, Kenji Ohoyama, Ryoji Kanno, Masatomo Yashima, and Atsuo Yamada. Experimental visualization of lithium diffusion in lixfepo4. *Nat. mater.*, 7(9):707–711, 2008.

[28] D Morgan, A Van der Ven, and G Ceder. Li conductivity in $LiMPO_4$ (M= Mn, Fe, Co, Ni) olivine materials. *Electrochem. Solid-State Lett.*, 7(2):A30–A32, 2004.

[29] M Saiful Islam, Daniel J Driscoll, Craig AJ Fisher, and Peter R Slater. Atomic-scale investigation of defects, dopants, and lithium transport in the $LiFePO_4$ olivine-type battery material. *Chem. Mater.*, 17(20):5085–5092, 2005.

[30] W. Kohn and L. J. Sham. Self-consistent equations including exchange and correlation effects. *Phys. Rev.*, 140:A1133–A1138, 1965.

[31] W. Kohn, A. D. Becke, and R. G. Parr. Density functional theory of electronic structure. *J. Phys. Chem.*, 100:12974–12980, 1996.

[32] J. P. Perdew. Unified theory of exchange and correlation beyond the local density approximation. In P. Ziesche and H. Eschrig, editors, *Electronic Structure of Solids*, pages 11–20. Akademie Verlag, Berlin, 1991.

[33] F. Zhou, M. Cococcioni, C. A. Marianetti, D. Morgan, and G. Ceder. First-principles prediction of redox potentials in transition-metal compounds with LDA+U. *Phys. Rev. B*, 70:235121, 2004.

[34] T. Maxisch, F. Zhou, and G. Ceder. *Ab initio* study of the migration of small polarons in olivine Li_xFePO_4 and their association with lithium ions and vacancies. *Phys. Rev. B*, 73:104301, 2006.

[35] G. Kresse and J. Furthmüller. Efficiency of ab-initio total energy calculations for metals and semiconductors using a plane-wave basis set. *Comput. Mater. Sci.*, 6:15–50, 1996.

[36] G. Kresse and J. Furthmüller. Efficient iterative schemes for ab initio total-energy calculations using a plane-wave basis set. *Phys. Rev. B*, 54:11169–11186, 1996.

[37] L. Wang, F. Zhou, Y. S. Meng, and G. Ceder. First-principles study of surface properties of $LiFePO_4$: Surface energy, structure, Wulff shape, and surface redox potential. *Phys. Rev. B*, 76:165435, 2007.

[38] F. Zhou, T. Maxisch, and G. Ceder. Configurational electronic entropy and the phase diagram of mixed-valence oxides: The case of Li_xFePO_4. *Phys. Rev. Lett*, 97:155704, 2006.

[39] G. K. P. Dathar, D. Sheppard, K. J. Stevenson, and G. Henkelman. Calculations of li ion diffusion in olivine phosphates. *Chem. Mater.*, 23:4032–4037, 2011.

[40] Claude Montella. Discussion of the potential step method for the determination of the diffusion coefficients of guest species in host materials: Part i. influence of charge transfer kinetics and ohmic potential drop. *J. Electroanal. Chem.*, 518(2):61–83, 2002.

[41] John B. Goodenough. Rechargeable batteries: Challenges old and new. *J. Solid State Electrochem.*, 16(6):2019–2029, 2012.

[42] Yuhao Lu, Long Wang, Jinguang Cheng, and John B. Goodenough. Prussian blue: A new framework of electrode materials for sodium batteries. *Chem. Commun.*, 48(52):6544–6546, 2012.

[43] J Gaubicher, C Wurm, G Goward, C Masquelier, and L Nazar. Rhombohedral form of $Li_3V_2(PO_4)_3$ as a cathode in Li-ion batteries. *Chem. Mater.*, 12(11):3240–3242, 2000.

[44] Shinichi Komaba, Wataru Murata, Toru Ishikawa, Naoaki Yabuuchi, Tomoaki Ozeki, Tetsuri Nakayama, Atsushi Ogata, Kazuma Gotoh, and Kazuya Fujiwara. Electrochemical Na insertion and solid electrolyte interphase for hard-carbon electrodes and application to Na-ion batteries. *Adv. Funct. Mater.*, 21(20):3859–3867, 2011.

[45] Kyu Tae Lee, TN Ramesh, F Nan, G Botton, and Linda F Nazar. Topochemical synthesis of sodium metal phosphate olivines for sodium-ion batteries. *Chem. Mater.*, 23(16):3593–3600, 2011.

[46] Brian L Ellis, WR Michael Makahnouk, WN Rowan-Weetaluktuk, DH Ryan, and Linda F Nazar. Crystal structure and electrochemical properties of A_2MPO_4F fluorophosphates (A = Na, Li; M= Fe, Mn, Co, Ni). *Chem. Mater.*, 22(3):1059–1070, 2009.

[47] F Sauvage, E Quarez, J-M Tarascon, and E Baudrin. Crystal structure and electrochemical properties vs. Na^+ of the sodium fluorophosphate $Na_{1.5}VOPO_4F_{1.5}$. *Solid State Sci.*, 8(10):1215–1221, 2006.

[48] RKB Gover, A Bryan, P Burns, and J Barker. The electrochemical insertion properties of sodium vanadium fluorophosphate, $Na_3V_2(PO_4)_2F_3$. *Solid State Ionics*, 177(17):1495–1500, 2006.

[49] J Barker, RKB Gover, P Burns, and AJ Bryan. $Li_{4/3}Ti_{5/3}O_4 \parallel Na_3V_2(PO_4)_2F_3$: An example of a hybrid-ion cell using a non-graphitic anode. *J. Electrochem. Soc.*, 154(9):A882–A887, 2007.

[50] Young-Uk Park, Dong-Hwa Seo, Byoungkook Kim, Kun-Pyo Hong, Hyungsub Kim, Seongsu Lee, Rana A Shakoor, Keiichi Miyasaka, Jean-Marie Tarascon, and Kisuk Kang. Tailoring a fluorophosphate as a novel 4 v cathode for lithium-ion batteries. *Sci. Rep.*, 2, 2012.

[51] Paula Serras, Verónica Palomares, Aintzane Goñi, Pierre Kubiak, and Teofilo Rojo. Electrochemical performance of mixed valence $Na_3V_2O_{2x}(PO_4)_2F_{3-2x}$/C as cathode for sodium-ion batteries. *J. Power Sources*, 241:56–60, 2013.

[52] David J Wales and Jonathan PK Doye. Global optimization by basin-hopping and the lowest energy structures of lennard-jones clusters containing up to 110 atoms. *J. Phys. Chem. A*, 101(28):5111–5116, 1997.

[53] SL Dudarev, GA Botton, SY Savrasov, CJ Humphreys, and AP Sutton. Electron-energy-loss spectra and the structural stability of nickel oxide: An lsda+ u study. *Physical Review B*, 57(3):1505–1509, 1998.

[54] David O Scanlon, Aron Walsh, Benjamin J Morgan, and Graeme W Watson. An ab initio study of reduction of V_2O_5 through the formation of oxygen vacancies and Li intercalation. *J. Phys. Chem. C*, 112(26):9903–9911, 2008.

[55] Youhao Liao, Kyu-Sung Park, Penghao Xiao, Graeme Henkelman, Weishan Li, and John B. Goodenough. Sodium intercalation behavior of layered Na_xNbS_2 ($0 \leq x \leq 1$). *Chem. Mater.*, 25(9):1699–1705, 2013.

[56] R.A. Shakoor, Dong-Hwa Seo, Hyungsub Kim, Young-Uk Park, Jongsoon Kim, Sung-Wook Kim, Hyeokjo Gwon, Seongsu Lee, and Kisuk Kang. A combined first principles and experimental study on $Na_3V_2(PO_4)_2F_3$ for rechargeable Na batteries. *J. Mater. Chem.*, 22(38):20535–20541, 2012.

[57] Kuniko Chihara, Ayuko Kitajou, Irina D Gocheva, Shigeto Okada, and Jun-ichi Yamaki. Cathode properties of $Na_3M_2(PO_4)_2F_3$ [M = Ti, Fe, V] for sodium-ion batteries. *J. Power Sources*, pages 80–85, 2012.

[58] G. Henkelman and H. Jónsson. Improved tangent estimate in the nudged elastic band method for finding minimum energy paths and saddle points. *J. Chem. Phys.*, 113:9978–9985, 2000.

[59] G. Henkelman, B. P. Uberuaga, and H. Jónsson. A climbing image nudged elastic band method for finding saddle points and minimum energy paths. *J. Chem. Phys.*, 113:9901–9904, 2000.

[60] H. Jónsson, G. Mills, and K. W. Jacobsen. Nudged elastic band method for finding minimum energy paths of transitions. In B. J. Berne, G. Ciccotti, and D. F. Coker, editors, *Classical and Quantum Dynamics in Condensed Phase Simulations*, pages 385–404. World Scientific, Singapore, 1998.

[61] G. Henkelman, A. Arnaldsson, and H. Jónsson. Theoretical calculations of CH_4 and H_2 associative desorption from Ni(111): Could subsurface hydrogen play an important role? *J. Chem. Phys.*, 124:044706, 2006.

[62] J. C. Polanyi and Wong. Location of energy barriers. I. Effect on the dynamics of reactions A + BC. *J. Chem. Phys.*, 51:1439–1450, 1969.

[63] D. R. Trinkle, R. G. Hennig, S. G. Srinivasan, D. M. Hatch, M. D. Jones, H. T. Stokes, R. C. Albers, and J. W. Wilkins. New mechanism for the α to ω martensitic transformation in pure titanium. *Phys. Rev. Lett.*, 91:025701, 2003.

[64] R. G. Hennig, D. R. Trinkle, J. Bouchet, S. G. Srinivasan, R. C. Albers, and J. W. Wilkins. Impurities block the α to ω martensitic transformation in titanium. *Nat. Mater.*, 4:129, 2005.

[65] K. J. Caspersen and E. A. Carter. Finding transition states for crystalline solid-solid phase transformations. *Proc. Nat. Acad. Sci.*, 102:6738–6743, 2005.

[66] D. F. Johnson and E. A. Carter. Nonadiabaticity in the iron bcc to hcp phase transformation. *J. Chem. Phys.*, 128:104703, 2008.

[67] J. B. Liu and D. D. Johnson. bcc-to-hcp transformation pathways in iron versus hydrostatic pressure: Coupled shuffle and shear modes. *Phys. Rev. B*, 79:134113, 2009.

[68] E. Rabani. An interatomic pair potential for cadmium selenide. *J. Chem. Phys.*, 116:258, 2002.

[69] S. Plimpton. Fast parallel algorithms for short-range molecular dynamics. *J. Comp. Chem.*, 117:1, 1995.

[70] See https://wiki.fysik.dtu.dk/ase/ for information about the ASE project.

[71] See http://theory.cm.utexas.edu/henkelman/code/ to obtain the TSASE code.

[72] See http://theory.cm.utexas.edu/vtsttools/code/ for additional information and to obtain the VASP Transition State Theory code.

[73] H. J. Monkhorst and J. D. Pack. Special points for Brillouin-zone integrations. *Phys. Rev. B*, 13:5188–5192, 1976.

[74] You Xiang Zhao and Ian L. Spain. X-ray diffraction data for graphite to 20 GPa. *Phys. Rev. B*, 40:993–997, Jul 1989.

[75] M. Hanfland, H. Beister, and K. Syassen. Graphite under pressure: Equation of state and first-order Raman modes. *Phys. Rev. B*, 39:12598–12603, Jun 1989.

[76] Wendy L. Mao, Ho-Kwang Mao, Peter J. Eng, Thomas P. Trainor, Matthew Newville, Chi-chang Kao, Dion L. Heinz, Jinfu Shu, Yue Meng, and Russell J. Hemley. Bonding changes in compressed superhard graphite. *Science*, 302:425–427, 2003.

[77] F.P. Bundy, W.A. Bassett, M.S. Weathers, R.J. Hemley, H.K. Mao, and A.F. Gocharov. The pressure-temperature phase and transformation diagram for carbon; updated through 1994. *Carbon*, 34:141–153, 1996.

[78] Viktor F. Britun, Alexander V. Kurdyumov, and Igor A. Petrusha. Diffusionless nucleation of lonsdaleite and diamond in hexagonal graphite under static compression. *Powder Metall. Met. Ceram.*, 43:87–93, 2004.

[79] S. Scandolo, M. Bernasconi, G. L. Chiarotti, P. Focher, and E. Tosatti. Pressure-induced transformation path of graphite to diamond. *Phys. Rev. Lett.*, 74:4015–4018, May 1995.

[80] Y. Tateyama, T. Ogitsu, K. Kusakabe, and S. Tsuneyuki. Constant-pressure first-principles studies on the transition states of the graphite-diamond transformation. *Phys. Rev. B*, 54:14994–15001, Dec 1996.

[81] Jian-Tao Wang, Changfeng Chen, and Yoshiyuki Kawazoe. Low-temperature phase transformation from graphite to sp^3 orthorhombic carbon. *Phys. Rev. Lett.*, 106:075501, Feb 2011.

[82] D J Erskine and W J Nellis. Shock-induced martensitic phase transformation of oriented graphite to diamond. *Nature*, 349(6307):317–319, Jan 1991.

[83] W. H. Gust. Phase transition and shock-compression parameters to 120 GPa for three types of graphite and for amorphous carbon. *Phys. Rev. B*, 22:4744–4756, Nov 1980.

[84] Rustam Z Khaliullin, Hagai Eshet, Thomas D Kühne, Jörg Behler, and Michele Parrinello. Nucleation mechanism for the direct graphite-to-diamond phase transition. *Nat. Mater.*, 10:693–697, 2011.

[85] Daniel Sheppard, Penghao Xiao, William Chemelewski, Duane D. Johnson, and Graeme Henkelman. A generalized solid-state nudged elastic band method. *J. Chem. Phys.*, 136:074103, 2012.

[86] P. Maragakis, Stefan A. Andreev, Yisroel Brumer, David R. Reichman, and Efthimios Kaxiras. Adaptive nudged elastic band approach for transition state calculation. *J. Chem. Phys.*, 117(10):4651–4658, 2002.

[87] Stefan Grimme. Semiempirical GGA-type density functional constructed with a long-range dispersion correction. *J. Comp. Chem.*, 27(15):1787–1799, 2006.

[88] Koichiro Umemoto, Renata M. Wentzcovitch, Susumu Saito, and Takashi Miyake. Body-centered tetragonal C_4: A viable sp^3 carbon allotrope. *Phys. Rev. Lett.*, 104:125504, Mar 2010.

[89] Quan Li, Yanming Ma, Artem R. Oganov, Hongbo Wang, Hui Wang, Ying Xu, Tian Cui, Ho-Kwang Mao, and Guangtian Zou. Superhard monoclinic polymorph of carbon. *Phys. Rev. Lett.*, 102:175506, Apr 2009.

[90] Zhisheng Zhao, Bo Xu, Xiang-Feng Zhou, Li-Min Wang, Bin Wen, Julong He, Zhongyuan Liu, Hui-Tian Wang, and Yongjun Tian. Novel superhard carbon: C-centered orthorhombic C_8. *Phys. Rev. Lett.*, 107:215502, Nov 2011.

[91] Maximilian Amsler, José A. Flores-Livas, Lauri Lehtovaara, Felix Balima, S. Alireza Ghasemi, Denis Machon, Stéphane Pailhès, Alexander Willand, Damien Caliste, Silvana Botti, Alfonso San Miguel, Stefan Goedecker, and Miguel A. L. Marques. Crystal structure of cold compressed graphite. *Phys. Rev. Lett.*, 108:065501, Feb 2012.

[92] Qiang Zhu, Qingfeng Zeng, and Artem R. Oganov. Systematic search for low-enthalpy sp^3 carbon allotropes using evolutionary metadynamics. *Phys. Rev. B*, 85:201407, May 2012.

[93] Xiang-Feng Zhou, Guang-Rui Qian, Xiao Dong, Lixin Zhang, Yongjun Tian, and Hui-Tian Wang. *Ab initio* study of the formation of transparent carbon under pressure. *Phys. Rev. B*, 82:134126, Oct 2010.

[94] Haiyang Niu, Xing-Qiu Chen, Shibing Wang, Dianzhong Li, Wendy L. Mao, and Yiyi Li. Families of superhard crystalline carbon allotropes constructed via cold compression of graphite and nanotubes. *Phys. Rev. Lett.*, 108:135501, Mar 2012.

[95] Motohiko Murakami, Kei Hirose, Katsuyuki Kawamura, Nagayoshi Sata, and Yasuo Ohishi. Post-perovskite phase transition in $MgSiO_3$. *Science*, 304(5672):855–858, May 2004.

[96] Artem R Oganov and Shigeaki Ono. Theoretical and experimental evidence for a post-perovskite phase of $MgSiO_3$ in Earth's D″ layer. *Nature*, 430(6998):445–448, July 2004.

[97] Taku Tsuchiya, Jun Tsuchiya, Koichiro Umemoto, and Renata M. Wentzcovitch. Phase transition in $MgSiO_3$ perovskite in the earth's lower mantle. *Earth. Planet. Sci. Lett.*, 224(3-4):241–248, August 2004.

[98] Hiroshi Kojitani, Yuichi Shirako, and Masaki Akaogi. Post-perovskite phase transition in $CaRuO_3$. *Phys. Earth Planet. Inter.*, 165(3-4):127–134, December 2007.

[99] Ken Niwa, Takehiko Yagi, Kenya Ohgushi, Sébastien Merkel, Nobuyoshi Miyajima, and Takumi Kikegawa. Lattice preferred orientation in $CaIrO_3$ perovskite and post-perovskite formed by plastic deformation under pressure. *Phys. Chem. Miner.*, 34(9):679–686, August 2007.

[100] Shigehiko Tateno, Kei Hirose, Nagayoshi Sata, and Yasuo Ohishi. Structural distortion of $CaSnO_3$ perovskite under pressure and the quenchable post-perovskite phase as a low-pressure analogue to $MgSiO_3$. *Phys. Earth Planet. Inter.*, 181(1-2):54–59, July 2010.

[101] Kazunari Yamaura, Yuichi Shirako, Hiroshi Kojitani, Masao Arai, David P Young, Masaki Akaogi, Mamoru Nakashima, Tetsuhiro Katsumata, Yoshiyuki Inaguma, and Eiji Takayama-Muromachi. Synthesis and magnetic and charge-transport properties of the correlated 4d post-perovskite $CaRhO_3$. *J. Am. Chem. Soc.*, 131(7):2722–2726, February 2009.

[102] Taku Tsuchiya and Jun Tsuchiya. Structure and elasticity of Cmcm $CaIrO_3$ and their pressure dependences: *Ab initio* calculations. *Phys. Rev. B*, 76:144119, Oct 2007.

[103] J.-G. Cheng, J.-S. Zhou, and J. B. Goodenough. Stress-induced perovskite to post-perovskite transition in $CaIrO_3$ at room temperature. *Phys. Rev. B*, 82(13):132103, October 2010.

[104] Ken Niwa, Nobuyoshi Miyajima, Yusuke Seto, Kenya Ohgushi, Hirotada Gotou, and Takehiko Yagi. In situ observation of shear stress-induced perovskite to post-perovskite phase transition in $CaIrO_3$ and the development of its deformation texture in a diamond-anvil cell up to 30GPa. *Phys. Earth Planet. Inter.*, 194-195:10–17, March 2012.

[105] Ken Niwa, Takehiko Yagi, and Kenya Ohgushi. Elasticity of $CaIrO_3$ with perovskite and post-perovskite structure. *Phys. Chem. Miner.*, 38(1):21–31, June 2010.

[106] Artem R Oganov, Roman Martonák, Alessandro Laio, Paolo Raiteri, and Michele Parrinello. Anisotropy of Earth's D″ layer and stacking faults in the $MgSiO_3$ post-perovskite phase. *Nature*, 438(7071):1142–1144, December 2005.

[107] Kyle J Caspersen and Emily A Carter. Finding transition states for crystalline solid-solid phase transformations. *Proc. Natl. Acad. Sci. USA*, 102(19):6738–6743, May 2005.

[108] S. Mayr. Activation energy of shear transformation zones: A key for understanding rheology of glasses and liquids. *Phys. Rev. Lett.*, 97(19):195501, November 2006.

[109] Sai Sriharsha M. Konda, Johnathan N. Brantley, Christopher W. Bielawski, and Dmitrii E. Makarov. Chemical reactions modulated by mechanical stress: extended Bell theory. *J. Chem. Phys.*, 135(16):164103, October 2011.

[110] Alaska Subedi. First-principles study of the electronic structure and magnetism of $CaIrO_3$. *Phys. Rev. B*, 85(2):020408, January 2012.

[111] George I. Bell. Models for the specific adhesion of cells to cells. *Science*, 200(4342):618–627, 1978.

[112] Kyle Caspersen, Adrian Lew, Michael Ortiz, and Emily Carter. Importance of shear in the bcc-to-hcp transformation in iron. *Phys. Rev. Lett.*, 93(11):115501, September 2004.

[113] C. Wert and C. Zener. Interstitial atomic diffusion coefficients. *Phys. Rev.*, 76:1169–1175, 1949.

[114] G. H. Vineyard. Frequency factors and isotope effects in solid state rate processes. *J. Phys. Chem. Solids*, 3:121–127, 1957.

[115] G. Henkelman and H. Jónsson. A dimer method for finding saddle points on high dimensional potential surfaces using only first derivatives. *J. Chem. Phys.*, 111:7010–7022, 1999.

[116] R. A. Olsen, G. J. Kroes, G. Henkelman, A. Arnaldsson, and H. Jónsson. Comparison of methods for finding saddle points without knowledge of the final states. *J. Chem. Phys.*, 121:9776–9792, 2004.

[117] L. Xu and G. Henkelman. Adaptive kinetic Monte Carlo for first-principles accelerated dynamics. *J. Chem. Phys.*, 129:114104, 2008.

[118] A. B. Bortz, M. H. Kalos, and J. L. Lebowitz. A new algorithm for Monte Carlo simulation of Ising spin systems. *J. Comput. Phys.*, 17:10, 1975.

[119] D. T. Gillespie. A general method for numerically simulating the stochastic time evolution of coupled chemical reactions. *J. Comp. Phys.*, 22:403–434, 1976.

[120] A. Heyden, A. T. Bell, and F. J. Keil. Efficient methods for finding transition states in chemical reactions: Comparison of improved dimer method and partitioned rational function optimization method. *J. Chem. Phys.*, 123:224101–1–14, 2005.

[121] J. Kästner and P. Sherwood. Superlinearly converging dimer method for transition state search. *J. Chem. Phys.*, 128:014106–1–6, 2008.

[122] D. Sheppard, P. Xiao, W. Chemelewski, D. D. Johnson, and G. Henkelman. A generalized solid-state nudged elastic band method. *J. Chem. Phys.*, 136:074103, 2012.

[123] R. A. Horn and C. R. Johnson. *Matrix Analysis*. Cambridge University Press, Cambridge, 1985.

[124] L. J. Munro and D. J. Wales. Defect migration in crystalline silicon. *Phys. Rev. B*, 59:3969, 1999.

[125] W. E and X. Zhou. The gentlest ascent dynamics. *Nonlinearity*, 24:1831, 2011.

[126] G. Henkelman and H. Jónsson. Long time scale kinetic Monte Carlo simulations without lattice approximation and predefined event table. *J. Chem. Phys.*, 115:9657–9666, 2001.

[127] S. T. Chill, M. Welborn, R. Terrell, L. Zhang, J.-C. Berthet, A. Pedersen, H. Jónsson, and G. Henkelman. Eon: Software for long time scale simulations of atomic scale systems. *Model. Simul. Mater. Sci. Eng.*, in press, 2014.

[128] O. M. Becker and M. Karplus. The topology of multidimensional potential energy surfaces: Theory and application to peptide structure and kinetics. *J. Chem. Phys.*, 106:1495–1517, 1997.

[129] Martin Jansen. A concept for synthesis planning in solid-state chemistry. *Angew. Chem. Int. Ed.*, 41(20):3746–3766, 2002.

[130] Michael Grünwald, Katie Lutker, A Paul Alivisatos, Eran Rabani, and Phillip L Geissler. Metastability in pressure-induced structural transformations of CdSe/ZnS core/shell nanocrystals. *Nano Lett.*, 13(4):1367–1372, 2012.

[131] Penghao Xiao and Graeme Henkelman. Communication: From graphite to diamond: Reaction pathways of the phase transition. *J. Chem. Phys.*, 137:101101, 2012.

[132] C. M. F. Rae and R. C. Reed. The precipitation of topologically close-packed phases in rhenium-containing superalloys. *Acta Mat.*, 49(19):4113, 2001.

[133] B. Seiser, T. Hammerschmidt, A. N. Kolmogorov, R. Drautz, and D. G. Pettifor. Theory of structural trends within $4d$ and $5d$ transition metal topologically close-packed phases. *Phys. Rev. B*, 83(22):224116, 2011.

[134] X. W. Zhou, H. N. G. Wadley, R. A. Johnson, D. J. Larson, N. Tabat, A. Cerezo, A. K. Petford-Long, G. D. W. Smith, P. H. Clifton, R. L. Martens, and T. F. Kelly. Atomic scale structure of sputtered metal multilayers. *Acta. Mater.*, 49:4005–4015, 2001.